FACULTY OF ENGINEERING
AND ARCHITECTURE

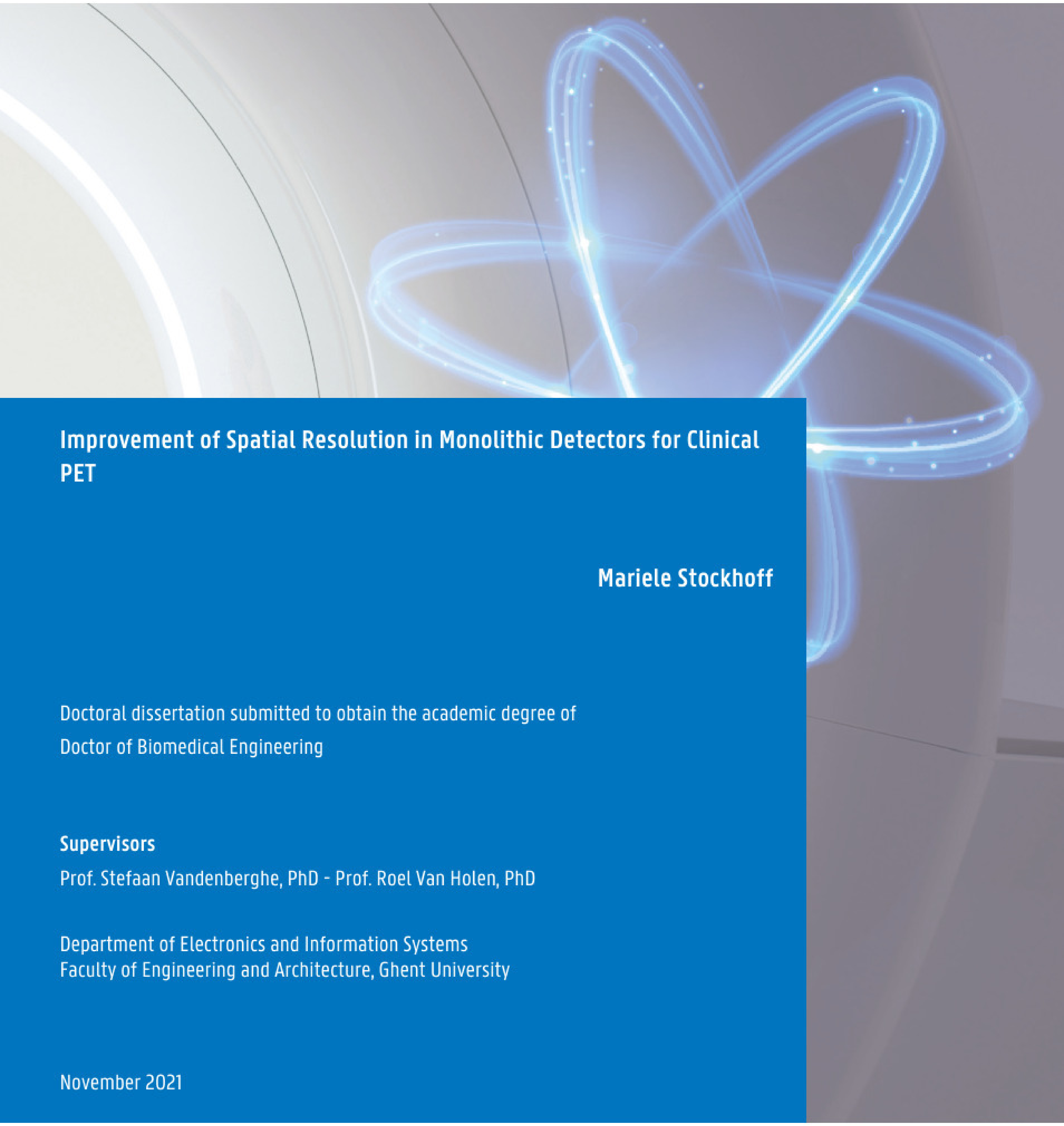

# Improvement of Spatial Resolution in Monolithic Detectors for Clinical PET

**Mariele Stockhoff**

Doctoral dissertation submitted to obtain the academic degree of
Doctor of Biomedical Engineering

**Supervisors**
Prof. Stefaan Vandenberghe, PhD - Prof. Roel Van Holen, PhD

Department of Electronics and Information Systems
Faculty of Engineering and Architecture, Ghent University

November 2021

GHENT
UNIVERSITY

FACULTY OF ENGINEERING
AND ARCHITECTURE

# Improvement of Spatial Resolution in Monolithic Detectors for Clinical PET

**Mariele Stockhoff**

Doctoral dissertation submitted to obtain the academic degree of
Doctor of Biomedical Engineering

**Supervisors**
Prof. Stefaan Vandenberghe, PhD - Prof. Roel Van Holen, PhD

Department of Electronics and Information Systems
Faculty of Engineering and Architecture, Ghent University

November 2021

GHENT
UNIVERSITY

ISBN 978-94-6355-543-2
NUR 954
Wettelijk depot: D/2021/10.500/91

# Members of the Examination Board

## Chair

Prof. Em. Hendrik Van Landeghem, PhD, Ghent University

## Other members entitled to vote

Prof. Matthieu Boone, PhD, Ghent University
Prof. Yves D'Asseler, PhD, Ghent University
Prof. Pawel Moskal, PhD, Jagiellonian University, Poland
Prof. Emilie Roncali, PhD, University of California Davis, USA
Prof. Karl Ziemons, PhD, Fachhochschule Aachen, Germany

## Supervisors

Prof. Stefaan Vandenberghe, PhD, Ghent University
Prof. Roel Van Holen, PhD, Ghent University

# Acknowledgements

In the last 1.5 years it has become more evident than ever before how much we need social connections to function. For a good reason does a PhD thesis usually start with the acknowledgement of the people that support us in our professional environment but also in our life outside of work. In the context of the Corona pandemic I want to start by thanking **Rik Van de Walle** the rector of UGent for sending out uncountable empowering e-mails to all UGent employees and students. Rik asked everyone to show leniency in the assessment of others and more importantly yourself. I am very sure that you helped me stay sane when I was not fulfilling my own expectations.

I would like to express my gratitude to my supervisors **Stefaan Vandenberghe** and **Roel Van Holen**. **Stefaan**, thank you for accepting me as a PhD student at MEDISIP and providing the funding to do my research. You gave me the opportunity and freedom to develop. A highlight working with you was being part of the TB-PET conference organising committee. Bringing together people from all over the world and showing them around in Gent was a true pleasure that I will never forget. I remember our first Skype interview before I accepted the PhD position. Since I was in the US it was already quite late in Belgium and you enjoyed a Belgian beer out of a wine glass. This was the first taste of Belgian culture for me and four years later I think I understand the importance. **Roel**, thank you for listening to my latest findings and concerns week after week after week. My motivation to keep going certainly comes from the support I got from you. Thank you for pushing me when I felt like I cannot improve my results further. It was always a mystery to me how you combine your companies, professorship and family and still being brilliant and in constant good mood. Thank you for taking it with humour when I have been doing measurements with an upside-down detector (or better front side-back) for a while!

Thanks to my great colleague and friend **Milan**. We began our PhD journey together and did our Oktoberfest starters party together. We ran a half marathon together. We published two papers together and submitted our PhD thesis at the exact same day. There are only few people that can bring me laughing to tears but you are one of them. Congratulations again on your phenomenal PhD defense! You have a great future ahead of you!

Thanks to all my colleagues at Medisip. I will miss being around you guys everyday and I will miss my top floor desk with the amazing view on the hospital campus. Please let me know when the building is torn down and I will light a candle. **Emma**, congratulations again on finishing your PhD. I wish you all the best for the future and may you always be the most connected node in your network. **Jens**, I enjoyed a lot sharing the office with you. Your relaxed and positive nature spreads on the people around you! **Ashkan**, you are most of the time not in the office, but when you are there, no one will miss your presence. You make sure that you have greeted everyone in the office personally. Pretty soon you will need a good glove to deal with all the handshakes. **Charlotte**, you were my very first student in Gent and I am happy that you continued your PET research. When something needs to be organised, be it a party or a present you are always in the first row. Thank you! **Jolan**, thanks for not wearing rain pants on rainy days. Why would you, if you can also just dry your pants on the radiators and sit on your desk in a slip? **Gert**, I always enjoy chatting with you when you are around. Good luck with your studies and research! **Lars**, it is always a pleasure to catch up with you when you are around. **Benedicte**, thank you for spreading your positive energy! **Maya**, even though you are far away in Qatar, it feels like I know you very well. Good luck and hope to see you again sometime. And my new colleague **Emma**, enjoy your time at Medisip. I also want to thank my previous colleagues and their partners **Marek & Darja, Stijn & Valerie, Paulo & Thayenny** and **Tim** who became my best friends in Gent. I could write a lot here, but I hope each one of you knows how much I appreciate you! A big thank you also to my previous colleagues **Prakash, Jens, Willeke** and **Kim**. Thanks to **Saskia** and **Jurgen**: In an environment where everyone moves on at some point you are the foundation and constants. Thanks for being approachable and helping us with all the technical and administrative issues. **Inge**, even though you are like 20 years older than me it feels like you are just another friend that I can talk to about everything. Thanks so much for being who you are!

To all the Biommeda colleagues: Without you the lunch breaks wouldn't have been the same. **Carlos, Ghazal, Hooman, Lise, Matthias, Samaneh, Sarah, Tim, Annette, Hicham, Mathias, Daimé, Frederico, Viviana, Daniela, Wouter**. Thanks to **Amith** for always stopping by at our office. You are the most hipster Indian guy I know and always spreading a good vibe. And to the more recent people who joined: **Bhawna, Melissa, Yousof, Simeon, Saar**: You are so much fun and have so much energy. I have a 'fear of missing out' before even having left! Thanks to all the professors: **Charlotte, Chris, Pieter** and **An**. **Patrick**, make sure you stop by for a coffee when going to your DIY store of choice in the future!

Thanks to our visiting researchers. **Nikos**, I spent my first weeks in Gent with you and I ran into you on several conferences which was so much fun. I hope we will keep running into each other somewhere on this small planet. **David**, even though the time was limited, I am so happy to have met you. And damn, this goodbye party was the best of the best. Racing across the work hallway in trash bins or optionally without pants. Hope to visit you soon to help build your new house!
Thanks to the whole Molecubes crew and especially **Karel, Radek** and **Pieter**. I could not have done the experimental part of my PhD without your help. Thanks to all the members of the Gate collaboration and the UTOFPET group. Thanks to **Karl Ziemons** for being part of my complete academic path from Bachelor to PhD. The fact that you travelled to the US and Belgium to be part of my defenses means a lot to me! Thanks to my university friends that helped me to balance study sessions and party sessions: **Flo, Kenan, Isi, Ahmed** and **Lina**. Thanks to the Cherry lab at University of California, Davis where I was able to gain the confidence to start a PhD: **Martin, Shamira, Simon, Peng, Sun Il, Aaron, Katya** and **Carlotta**. Special thanks to **Emilie**, who I learned so much from and is one of the most dedicated researchers I know. **Jill**, we first met on the PhD introduction day and sneaked out to get beers at the Irish pub. Ideal start of a PhD student friendship. Thanks for the many runs, walks and talks at Bourgoyen. You are mastering your research with cows and at the same time you are a master of so many other arts of life. Thank you! Mijn grote uitlaatklep naast mijn onderzoek was de loopgroep in Gent, waar ik niet alleen gepusht wordt om een marathon te lopen, maar ook om constant

mijn Nederlands te oefenen. Dank u **Stefaan, Charles, Ilse** en **Sarah** en alle anderen lopers!

Auch nach 7 Jahren im Ausland könnte mir eins nicht wichtiger sein: Heimat und Familie. Meine Runde in Borken zu drehen und euch alle zu besuchen macht mir unglaublich viel Spaß. Danke, dass ihr immer für mich da seid und dass ihr mich jedes Mal mit offenen Armen empfangt. **Mama & Thomas, Papa & Ulrike**: Wie ihr einfach immer eure eigenen Bedürfnisse hinten anstellt um uns zu unterstützen und zu beschützen wird einem erst klar wenn man selbst erwachsen ist. **Bene & Lea, Gerrit & Maiki**, danke dass wir uns alle so gut verstehen und ich hoffe ihr kommt uns oft besuchen. Das erste was Mama nach meiner bestandenen Verteidigung gesagt hat war: "Oma wäre stolz gewesen." Ich hätte euch alle so gerne an meiner Doktoratsverteidigung dabei gehabt: **Oma & Opa Stockhoff** und **Oma & Opa Buss**. Was wäre ich ohne meine besten Freunde die ich auf den verschiedenen Stationen des Lebens gesammelt habe: **Louisa, Johanna, Christina, Caro, Caro, Laura, Becki, Mona, Steffi, Sascha**! Ihr seid die Besten!

Ten slotte blijft nog een heel belangrijke persoon over: **Thomas**. Ik ben heel blij dat ik jou gevonden heb. De mens met wie je graag alles deelt. Ik heb nooit veel moeten nadenken om te weten dat ik graag met jou wil zijn of met jou wil samen wonen. Ik ben gewoon zo graag bij jou. Love you!

Mariele Stockhoff
November 2021, Gent

# Summary

Positron emission tomography (PET) is a frequently used imaging technique. While most scans provide anatomical information such as computerized tomography (CT) or magnetic resonance imaging (MRI), a PET scan allows the visualization of functional processes. The injection of, for instance, the radiopharmaceutical $^{18}$F-fluorodeoxyglucose ($^{18}$F-FDG) enables the tracking of sugar molecules throughout the body. The radiopharmaceutical, also called tracer, has a radioactive ligand $^{18}$F that emits gamma rays which can be measured by the PET detectors. Very active organs, like the brain or heart have a high sugar consumption and are clearly visible on a $^{18}$F-FDG-PET scan. On the contrary tissues like fat and bones have a low sugar metabolism and will barely be visible. If regions with unexpectedly high sugar consumption, so called hot spots, show up on the PET image, it might indicate the presence of actively growing tumours. The early detection and treatment of tumours is crucial for the patients recovery. Often tumours form metastases which are very small tumours at other body regions. Unfortunately, metastases below a certain size are not visible in PET images. The ability of the scanner to resolve small structures is called the system spatial resolution. It is dependent on several factors. One of them is the detector intrinsic spatial resolution. The goal of this dissertation is the investigation of PET detectors that will be able to provide better spatial resolution for the use in clinical PET systems.

Typical PET detectors consist of a dense scintillation crystal that stops the highly energetic gamma ray. The energy is then converted proportionally to thousands of low-energetic light photons. This process is called scintillation. The scintillation photons are in turn measured by photodetectors that are attached to the crystal. In the state-of-the-art detector design the scintillator is cut into pixels of 2.8-5 mm. The purpose is to confine the scintillation light to a small area. The triggered

pixel then correlates to the location of the gamma ray detection. The width of the pixels however limits the obtainable resolution. A better resolution can be obtained by using smaller pixels. To reach the ultimate system resolution in a clinical PET scanner the intrinsic detector resolution should be around 1.3 mm. Detector spatial resolutions below 1.3 mm are not very useful in clinical PET, since system resolution is dominated by other fundamental resolution limits arising from beta decay and annihilation physics. The downside of decreasing the pixel width to this extent, is the loss of sensitivity, energy and timing resolution. Furthermore, the smaller the pixel width the more expensive it becomes to manufacture these pixelated crystals.

The alternative to pixelated crystals are monolithic crystals. As the name says, the crystal is not segmented but is a block of several centimetres width with a thickness of around 1-2 cm. One side of the block is coupled to a photodetector array. This array measures the light distribution inside the crystal. The light distribution is sampled by the photodetector pixels at a 2-6 mm pitch. The distribution's peak position and peak width allow an accurate 3D position estimation of the gamma ray interaction point. To obtain the best detector spatial resolution in monolithic detectors we have to overcome two major challenges. They are most likely the reasons why monolithic detectors are not yet implemented in commercial clinical PET systems.

The first challenge is the detector calibration. To correlate the measured photodetector signal to the actual gamma interaction position, a detector calibration is needed. In practice, a fine gamma ray beam scans the crystal at known positions and collects reference signals. This process requires a dedicated lab set-up and can be time consuming. Often this procedure is repeated for each individual PET detector. A system can consist of hundreds or even thousands of detectors.

The second challenge is the need for algorithms that are able to correlate the reference light distributions with the unknown gamma interaction location. There are many possible solutions to calculate the best fit between the pre-measured reference signals and the signal with the unknown interaction position. Statistical methods and artificial neural networks are popular candidates to solve this problem.

In conclusion, the design of the calibration set-up, the acquisition of reference data and the development of well-performing positioning algorithms are crucial to obtain a high resolution monolithic detector. To solve these challenges, in-depth knowledge and thorough studies are inevitable.

In this dissertation we investigate and improve monolithic detectors for the use in high resolution clinical PET systems.

In optical simulations we study a 50 x 50 x 16 $mm^3$ lutetium-yttrium oxyorthosilicate (LYSO) crystal. The crystal is read out by silicon photomultiplier (SiPM) photodetector arrays. The detector is calibrated by a gamma ray pencil beam in 1 mm steps. A statistical mean nearest neighbour (MNN) algorithm is implemented to predict the 3D interaction positions. The results indicate a 2D spatial resolution of 0.4-0.66 mm full width at half maximum (FWHM). Depth of interaction (DOI) estimation is implemented with a depth-layer approach. The DOI was estimated with an accuracy of 72% and a mean positioning error of 1.6 mm. This study confirmed the potential high resolution of the proposed detector design, the calibration techniques and positioning methods.

Following the simulation study, we built and evaluated the prototype detector. The obtained mean spatial resolution with the MNN positioning algorithm is 1.13 mm FWHM with small degradations towards the edges. The evaluation was extended to a second positioning algorithm based on artificial neural networks. The network achieves a more uniform resolution and smaller bias. The mean spatial resolution is 1.02 mm. DOI capability was enabled and implemented for both algorithms. The detector energy resolution is around 11% allowing a reliable distinction between scattered and non-scattered events. In conclusion, with our prototype we achieved a better intrinsic detector resolution than the desired 1.3 mm. The simulations and the prototype development allowed us to identify many factors that have an influence on the spatial resolution. We investigated the most important ones in detail, namely, the calibration beam size, the impact of Compton scattered events, the photodetector photon detection efficiency (PDE) and finally the impact of background radiation.

First, the impact of the calibration beam size is investigated. In our calibration set-up we can only collimate the beam to a diameter of 0.6 mm. In simulations and experiments we investigated, how the slightly shifted gamma interaction positions affect the detector performance, and if it would improve using an even smaller beam. Both, simulations and experiments confirmed that a 0.6 mm and a 1 mm beam size allow the calibration and training of a detector with comparable high resolution. The positioning algorithms are not negatively impacted by the slightly spread gamma interaction positions. However, for the detector evaluation the non-perfect calibration beam should be isolated. For this purpose the expected spatial resolution can be approximated by a mathematical deconvolution of the beam diameter width.

The second degrading factor is attributed to the Compton effect. More than half of the detected events have scattered once or multiple times resulting in an altered light distribution. In a simulation study we found that the resolution would improve by 9-12% in terms of FWHM when excluding scattered events. Not only the FWHM metric but also the tails of the point spread functions (PSFs) are broadened. More accurate positioning of scattered events is of great relevance for future high-resolution PET detectors. Towards the end of the book we investigate whether it is possible to improve positioning of Compton scattered events using neural networks.

As a third degrading factor we investigated the SiPM PDE. It is defined as the probability that a single photon is detected when impinging on the SiPM surface. In simulations a PDE reduction of 75% to 35% led to a resolution degradation of 16-30% depending on the size of SiPMs and the number of readout channels. Higher PDEs improve the signal to noise ratio (SNR) and are a major contributor to better spatial resolution in monolithic detectors. Also the introduction of scintillators with higher light yield and hence, more photons per energy unit, would improve the SNR. Current SiPM PDEs range between 35% and 60%, and are expected to improve further in the future.

The fourth degrading factor is the background radiation. A detector calibration in singles mode suffers from a strong background signal. It originates mainly from the radioactive scintillation material LYSO containing $^{176}$Lu, but also insufficient shielding thickness of the collimator housing. We present effective methods to filter relevant calibration events from background and provide high quality reference data.

To conclude, by the individual consideration of each degrading factor one can estimate the magnitude of the degradation and gain insight into the possibilities for improvement.

Throughout this thesis it has been shown that optical simulations are a great tool to support the PET detector development. Be it the prediction of detector performance metrics or the identification and analysis of degrading effects.

In the final part, we determine if we can use the simulated detector data and directly apply it to the training and positioning of the real detector. First, we use the calibration maps generated by simulations, to serve as reference data to position real events of the prototype detector. A calibration based on simulated reference data could potentially allow an elimination of the lengthy calibration procedure. We obtained a spatial resolution of 1.28 mm with a degradation towards the edges. Compared to the experimental calibration this is a degradation of 11.7%. The overall bias increased by 27% mostly attributed to the detector edges. The obtained resolution is slightly degraded but still reaching the 1.3 mm detector resolution goal. This preliminary study provides promising results for the role of optical simulation studies and potentially replacing the cumbersome calibration procedure. Future research to improve these results should be focused on a re-investigation of the reflection model for the detector sides.

Second, we want to use simulations to tackle the degrading effect that Compton scattered events have on the spatial resolution. We trained a scatter distance estimation network from simulated data. This way we were able to identify the events of the real detector that have a far scatter distance. The results demonstrated that removing only 10% of the farthest scattered events leads to a contrast improvement of our phantom of 6-18%. Keeping in mind the 'sensitivity-spatial resolution' trade-off, this is a great achievement which can be further improved by removing a larger fraction of scattered events.

This dissertation demonstrated that monolithic detectors, with sufficient thickness for clinical PET applications, can provide very high spatial resolution approaching the fundamental spatial resolution limits of PET. Using optical simulation models we were able to grasp the factors that are limiting the intrinsic detector resolution and improve the hardware and software design of the prototype detector. Furthermore the potential of directly applying simulated data to improve monolithic detectors was investigated. An important research topic in the future is the implementation of meaningful evaluation standards for the spatial resolution estimation across different research institutes. The variability of the methods makes it very difficult to compare the performance of different detectors, restraining the progress in the field. Furthermore, one should carefully consider whether or not the detector should also be optimized for time of flight (TOF) measurement. From our experience the design indications for high spatial resolution and high coincidence timing resolution (CTR) can be conflicting. A future research topic should be the determination of an equilibrium between spatial resolution and CTR.

Some groups focus on better and faster calibrations in coincidence mode, and by using a slit collimator. Resulting from this thesis, it is the logical next step, to further investigate the use of optical simulations to speed up detector calibration. As a major step towards better calibration with simulated data we see the accurate modelling of the reflective surfaces in the detector. A tool to ease the optical simulation workflow in Gate for monolithic detector calibration could be useful for the community.
The combination of high spatial resolution with efficient calibration methods and timing performance, can lead the way for monolithic detectors to be the detector of choice in future PET systems.

# Samenvatting

Positron emissie tomografie (PET) is een veel gebruikte beeldvormingstechniek. Terwijl de meeste scans anatomische informatie verschaffen zoals computertomografie (CT) of magnetic resonance imaging (MRI), kan met een PET-scan een functioneel proces worden gevisualiseerd. Door inspuiting van bijvoorbeeld het radiofarmacon $^{18}$F-fluorodeoxyglucose ($^{18}$F-FDG) kunnen suikermoleculen in het hele lichaam worden opgespoord. Het radiofarmacon, ook wel tracer genoemd, heeft een radioactief ligand $^{18}$F dat gammastralen uitzendt die door de PET-detectoren kunnen worden gemeten. Zeer actieve organen, zoals de hersenen of het hart, hebben een hoog suikerverbruik en zijn duidelijk zichtbaar op een $^{18}$F-FDG-PET-scan. Weefsels zoals vet en botten daarentegen hebben een laag suikermetabolisme en zullen nauwelijks zichtbaar zijn. Als op het PET-beeld regio's met een onverwacht hoog suikerverbruik te zien zijn, zogenaamde "hot spots", kan dit wijzen op de aanwezigheid van actief groeiende tumoren. Het vroegtijdig opsporen en behandelen van tumoren is van cruciaal belang voor het herstel van de patiënt. Vaak vormen tumoren uitzaaiingen, dat zijn zeer kleine tumoren in andere lichaamsgebieden. Helaas zijn uitzaaiingen beneden een bepaalde grootte niet zichtbaar op PET-beelden. Het vermogen van de scanner om kleine structuren op te sporen, wordt de ruimtelijke resolutie van het systeem genoemd. Deze is afhankelijk van verschillende factoren. Eén daarvan is de intrinsieke ruimtelijke resolutie van de detector. Het doel van dit proefschrift is het onderzoek naar PET detectoren die een betere ruimtelijke resolutie kunnen bieden voor gebruik in klinische PET systemen.

Typische PET-detectoren bestaan uit een dicht scintillatiekristal dat de hoogenergetische gammastraal tegenhoudt. De energie wordt vervolgens proportioneel omgezet in duizenden laag-energetische lichtfotonen. Dit proces wordt scintillatie genoemd. De scintillatiefotonen worden dan weer gemeten door fotodetectoren die aan het kristal zijn aangebracht. In het momenteel gangbare detectorontwerp wordt de scintillator gesneden in pixels van 2.8-5 mm. Het doel hiervan is het scintillatielicht tot een klein gebied te beperken. De geactiveerde pixel correleert dan met de plaats van de gammastraaldetectie. De breedte van de pixels beperkt echter de haalbare resolutie. Een betere resolutie kan worden verkregen door kleinere pixels te gebruiken. Om de best haalbare systeemresolutie in een klinische PET-scanner te bereiken, moet de intrinsieke detectorresolutie ongeveer 1.3 mm bedragen. Spatiële resoluties van de detector van minder dan 1.3 mm zijn niet erg nuttig bij klinische PET, omdat systeemresolutie wordt gedomineerd door andere fundamentele resolutielimieten die het gevolg zijn van de fysische eigenschappen van het beta verval en annihilatie. Het nadeel van een dergelijke verkleining van de pixelbreedte is het verlies van sensitiviteit, energie- en tijdresolutie. Bovendien geldt dat hoe kleiner de pixelbreedte wordt, hoe duurder het wordt om deze gepixelde kristallen te vervaardigen.

Het alternatief voor gepixelde kristallen zijn monolithische kristallen. Zoals de naam al zegt, is het kristal niet gesegmenteerd, maar is het een blok van enkele centimeters breed met een dikte van ongeveer 1-2 cm. Eén zijde van het blok is gekoppeld aan een fotodetector-rooster. Dit rooster meet de lichtverdeling in het kristal. De lichtverdeling wordt door de fotodetectorpixels gesampled op een afstand van 2-6 mm. De piekpositie en piekbreedte van de verdeling maken een nauwkeurige 3D-positiebepaling van de gammastraal mogelijk.

Om bij monolithische detectoren de beste ruimtelijke resolutie van de detector te verkrijgen, moeten we twee grote uitdagingen overwinnen. Deze zijn hoogstwaarschijnlijk de redenen waarom monolithische detectoren nog niet in commerciële klinische PET-systemen worden gebruikt. De eerste uitdaging is de kalibratie van de detector. Om het gemeten signaal van de fotodetector te correleren met de werkelijke gamma interactiepositie, is een kalibratie van de detector vereist. In de praktijk wordt het kristal op gekende posities gescand met een fijne bundel gammastralen en worden referentiesignalen verzameld. Dit proces vereist een specifieke labo opstelling en kan veel tijd in beslag nemen. Vaak wordt deze procedure voor iedere afzonderlijke PET-detector herhaald. Een systeem kan uit honderden of zelfs duizenden detectoren bestaan.

De tweede uitdaging is de nood aan algoritmen die de referentielichtverdelingen kunnen correleren met de onbekende gamma interactiepositie. Er zijn talrijke oplossingen mogelijk om de 'best fit' te berekenen tussen de vooraf gemeten referentiesignalen en het signaal met de onbekende interactieplaats. Statistische methoden en artificiële neurale netwerken zijn populaire kandidaten om dit probleem op te lossen.

Als conclusie kunnen we stellen dat het ontwerp van de kalibratieopstelling, de acquisitie van referentiedata en de ontwikkeling van goed werkende positioneringsalgoritmen van cruciaal belang zijn voor het verkrijgen van een monolithische detector met hoge resolutie. Om deze uitdagingen op te lossen, zijn diepgaande kennis en grondige studies onvermijdelijk.

In dit proefschrift onderzoeken en verbeteren we monolithische detectoren om in klinische PET-systemen met hoge resolutie te gebruiken.

In optische simulaties bestuderen we een 50 x 50 x 16 mm$^3$ lutetium-yttrium oxyorthosilicate (LYSO) kristal. Het kristal wordt uitgelezen door roosters van SiPM fotodetectoren. De detector wordt gekalibreerd met een gammabundel in stappen van 1 mm. Een statistisch mean nearest neighbour (MNN)-algoritme wordt geïmplementeerd om de 3D-interactieposities te berekenen. De resultaten geven een 2D ruimtelijke resolutie aan van 0.4-0.66 mm FWHM. De diepte van de interactie (DOI) schatting is uitgevoerd met een diepte-laag benadering. De DOI werd geschat met een nauwkeurigheid van 72% en een gemiddelde positioneringsfout van 1.6 mm. Deze studie bevestigde de potentiële hoge resolutie van het voorgestelde detectorontwerp, de kalibratietechnieken en de positioneringsmethoden.

Na de simulatiestudie hebben we het prototype van de detector ontworpen en geëvalueerd. De verkregen gemiddelde ruimtelijke resolutie met het MNN positioneringsalgoritme is 1.13 mm FWHM met kleine degradaties naar de randen toe. De evaluatie werd uitgebreid met een tweede positioneringsalgoritme op basis van artificiële neurale netwerken. Het netwerk bereikt een meer uniforme resolutie en een kleinere bias. De gemiddelde ruimtelijke resolutie bedraagt 1.02 mm. De DOI functionaliteit werd voor beide algoritmen geïmplementeerd. De energieresolutie van de detector bedraagt ongeveer 11%, wat een betrouwbaar onderscheid mogelijk maakt tussen verstrooide en niet-verstrooide gebeurtenissen.

We kunnen besluiten dat wij met ons prototype een betere intrinsieke detectorresolutie hebben bereikt dan de gewenste 1.3 mm. De simulaties en de ontwikkeling van het prototype lieten ons toe om vele factoren te identificeren die een invloed hebben op de ruimtelijke resolutie. Wij hebben de belangrijkste in detail onderzocht, namelijk de grootte van de kalibratiebundel, de invloed van Compton verstrooing, de foton detectie efficiëntie (PDE) en tenslotte de invloed van achtergrondstraling.

Eerst wordt de invloed van de grootte van de kalibratiebundel onderzocht. In onze kalibratieopstelling kunnen we de bundel slechts collimeren tot een diameter van 0.6 mm. Via simulaties en experimenten hebben we onderzocht hoe de lichtjes verschoven gamma-interactieposities de detectorprestaties beïnvloeden en of het gebruik van een nog kleinere bundel deze prestaties zouden verbeteren. Zowel simulaties als experimenten bevestigden dat een bundel van 0.6 mm en 1 mm de kalibratie en training van een detector met een vergelijkbaar hoge resolutie mogelijk maken. De positioneringsalgoritmen worden niet negatief beïnvloed door de licht gespreide gamma-interactieposities. Voor de evaluatie van de detector moet de niet-perfecte kalibratiebundel echter worden geïsoleerd. Daartoe kan de verwachte ruimtelijke resolutie worden benaderd door een mathematische deconvolutie van de bundeldiameterbreedte.

De tweede degraderende factor wordt toegeschreven aan het Compton effect. Meer dan de helft van de gedetecteerde gebeurtenissen zijn één of meerdere keren verstrooid, wat een veranderde lichtverdeling teweeg bracht. Uit simulaties bleek dat de resolutie met 9-12% zou verbeteren in termen van FWHM wanneer verstrooide gebeurtenissen worden uitgesloten. Niet alleen de FWHM metriek maar ook de staarten van de puntspreidingsfunctie (PSF) zijn breder geworden. Een nauwkeurigere positionering van verstrooide gebeurtenissen is van groot belang voor toekomstige PET-detectoren met hoge resolutie. Naar het einde van het boek toe onderzoeken we of het mogelijk is om de positionering van Compton verstrooide gebeurtenissen te verbeteren met behulp van neurale netwerken.

Als derde degraderende factor hebben we de SiPM PDE onderzocht. Deze is gedefinieerd als de waarschijnlijkheid dat één enkel foton wordt gedetecteerd wanneer het op het SiPM valt. In simulaties leidde een PDE-reductie van 75% naar 35% tot een resolutieverlies van 16 tot 30%, afhankelijk van de grootte van de SiPMs en het aantal uitleeskanalen. Hogere PDE's verbeteren de signaal-ruisverhouding (SNR) en dragen in belangrijke mate bij tot een betere ruimtelijke resolutie in monolithische detectoren. Ook de invoering van scintillatoren met een hogere lichtopbrengst en dus meer fotonen per energie-eenheid, zou de SNR verbeteren. De huidige PDE's van SiPM liggen tussen de 35% en 60% en zullen naar verwachting in de toekomst nog verder verbeteren.

De vierde degraderende factor is de achtergrondstraling. Een detectorkalibratie in *singles mode* heeft te lijden onder een sterk achtergrondsignaal. Dit wordt voornamelijk veroorzaakt door het radioactieve scintillatiemateriaal LYSO dat $^{176}$Lu bevat, maar ook door een onvoldoende dikke afscherming van de collimatorbehuizing. We stellen methoden voor om relevante kalibratie gebeurtenissen uit de achtergrond te filteren en zo referentiedata van hoge kwaliteit te verkrijgen.

We kunnen besluiten dat, door elke degraderende factor afzonderlijk te bekijken, men de omvang van de degradatie kan inschatten en men beter inzicht krijgt in verbeteringsmogelijkheden.

Doorheen dit proefschrift is aangetoond dat optische simulaties een goed hulpmiddel zijn bij de ontwikkeling van PET detectoren. Of het nu gaat om het voorspellen van de prestaties van de detector of het identificeren en analyseren van degraderende effecten.

In het laatste deel bepalen we of we de gesimuleerde detectorgegevens kunnen gebruiken en rechtstreeks kunnen toepassen op de training en positionering van de echte detector.

Ten eerste gebruiken we de kalibratiegegevens uit de simulaties als referentiedata voor echte gebeurtenissen van de prototype detector. Een kalibratie op basis van gesimuleerde referentiedata zou een lange kalibratieprocedure kunnen vermijden. We verkregen een ruimtelijke resolutie van 1.28 mm met een degradatie naar de randen toe. Vergeleken met de experimentele kalibratie is dit een degradatie van 11.7%. De totale bias is met 27% toegenomen, vooral te wijten aan de uiteinden van de detector. De verkregen resolutie is licht gedaald, maar bereikt nog steeds de 1.3 mm detectorresolutie doelstelling. Deze preliminaire studie levert veelbelovende resultaten op voor de rol van optische simulatiestudies en kan mogelijk de omslachtige kalibratieprocedure vervangen. Toekomstig onderzoek om deze resultaten te verbeteren, moet gefocust zijn op een heronderzoek van het reflectiemodel voor de detectorzijden.

Ten tweede willen we simulaties gebruiken om het degraderende effect van Compton verstrooing op de ruimtelijke resolutie aan te pakken. Op basis van gesimuleerde data bouwden we een netwerk uit dat de verstrooingsafstand kan inschatten. Op deze manier konden we de gebeurtenissen van de echte detector identificeren die een grote verstrooiingsafstand hebben. De resultaten toonden aan dat de eliminatie van slechts 10% van de meest verstrooide gebeurtenissen leidt tot een contrastverbetering van ons fantoom van 6-18%. De 'gevoeligheid-ruimtelijke resolutie' trade-off in gedachte houdende, is dit een uitstekend resultaat dat verder kan worden verbeterd door het uitsluiten van een nog grotere fractie van de verstrooide gebeurtenissen.

Dit proefschrift heeft aangetoond dat monolithische detectoren, die voldoende dik zijn voor klinische PET-toepassingen, een ultra-hoge ruimtelijke resolutie kunnen opleveren die heel dicht in de buurt komt van de fundamentele ruimtelijke resolutielimieten van PET. Met behulp van optische simulatiemodellen konden we factoren die de intrinsieke detectorresolutie beperken, doorgronden en konden we het hardware- en software ontwerp van de prototype detector verbeteren. Verder werd de mogelijkheid onderzocht om gesimuleerde data rechtstreeks te gebruiken om monolithische detectoren te verbeteren. Een belangrijk toekomstig onderzoeksthema is de implementatie van betekenisvolle evaluatienormen voor ruimtelijke resolutieschattingen in verschillende onderzoeksinstellingen. De brede waaier aan methoden maakt het zeer moeilijk om prestaties van verschillende detectoren te vergelijken en belemmert daardoor vooruitgang op dit gebied. Bovendien moet zorgvuldig worden overwogen of de detector al dan niet ook moet worden geoptimaliseerd voor Time of Flight (TOF) metingen. Uit onze ervaringen blijkt dat de indicaties voor een hoge ruimtelijke resolutie en een hoge coïncidentie tijdresolutie (CTR) tegenstrijdig kunnen zijn. In de toekomst zou onderzoek moeten worden gedaan naar een evenwicht tussen ruimtelijke resolutie en CTR. Sommige groepen richten zich op betere en snellere kalibraties in coïncidentiemodus en maken gebruik van een spleetcollimator. Uit dit proefschrift blijkt dat verder onderzoek naar het gebruik van optische simulaties om de kalibratie van detectoren te versnellen een volgende logische stap zou zijn. Het accuraat modelleren van de reflecterende oppervlakken in de detector beschouwen we als een belangrijke stap naar betere kalibratie via gesimuleerde data. Een tool om de optische simulatie-workflow in Gate voor monolithische detectorkalibratie te vergemakkelijken zou nuttig de onderzoeksgemeenschap ten goede komen.

De combinatie van hoge ruimtelijke resolutie met efficiënte kalibratiemethoden en timingprestaties kan ertoe leiden dat monolithische detectoren de voorkeursdetector worden in toekomstige PET-systemen.

# List of Abbreviations

| | |
|---|---|
| $^{18}$F-FDG | $^{18}$F-fluorodeoxyglucose |
| AFM | atomic force microscopy |
| ANN | artificial neural networks |
| APD | avalanche photodiode |
| BGO | bismuth germanium oxide |
| BOLD | blood oxygen level dependent |
| COG | center of gravity |
| CT | computerized tomography |
| CTR | coincidence timing resolution |
| DICOM | digital imaging and communications in medicine |
| DOI | depth of interaction |
| ESR | enhanced specular reflector |
| FDG | fluorodeoxyglucose |
| fMRI | functional magnetic resonance tomography |
| FOV | field of view |
| FWHM | full width at half maximum |
| GTB | gradient tree boosting |

| | |
|---|---|
| LOR | line of response |
| LSO | lutetium oxyorthosilicate |
| LUT | look up table |
| LYSO | lutetium-yttrium oxyorthosilicate |
| | |
| MLE | maximum likelihood estimation |
| MLEM | maximum likelihood expectation maximization |
| MNN | mean nearest neighbour |
| MRI | magnetic resonance imaging |
| MTF | modulation transfer function |
| | |
| PACS | picture archiving and communication system |
| PDE | photon detection efficiency |
| PET | positron emission tomography |
| PMT | photomultiplier tube |
| PSF | point spread function |
| | |
| ROI | region of interest |
| RTP | raised to the power |
| | |
| SiPM | silicon photomultiplier |
| SNR | signal to noise ratio |
| SPAD | single photon avalanche photodiode |
| SPECT | single photon emission tomography |
| | |
| TB | total body |
| TOF | time of flight |

# Contents

# 1

# Introduction

## 1.1 Context

The subject of this dissertation is situated in the field of positron emission tomography (PET), a medical imaging technique. PET scanners are typically found in nuclear medicine departments of major hospitals or in research institutes for clinical or preclinical (animal) studies. While most scans such as x-ray, CT or MRI, provide anatomical information, a PET scan allows the visualization of functional processes in-vivo. The injection of, for instance, the radiopharmaceutical $^{18}$F-fluorodeoxyglucose (FDG) enables the tracking of sugar molecules throughout the body while the radioactive ligand $^{18}$F decays under the emission of positrons. These positrons annihilate with electrons under the emission of two gamma rays that can be measured by the PET detectors. Sugar metabolism is linked to how active different tissues are and at the same time reveals pathologies such as tumour growth indicated by unexpected hot spots appearing in the PET images. Of utmost importance for the patients diagnosis, and the course and final outcome of the treatment is the accurate localisation of even the smallest metastases.

One of the factors that defines the image spatial resolution is the ability of the PET detector to determine exactly where it was hit by the gamma ray. The detector consists of a dense scintillation crystal that stops the highly energetic gamma ray and converts its energy proportionally to thousands of low-energetic light photons. These light photons are then measured by photodetectors. In the state-of-the-art detector design the scintillator is cut into pixels in order to confine the scintillation light to a small area that defines the interaction location of the gamma ray. The pixel size which is currently between 2.8-5 mm is limiting the obtainable resolution. A reduction of the pixel size induces the loss of other important performance metrics, such as lower sensitivity, lower energy and timing resolution and increased cost. Avoiding the use of pixels and instead reading out the scintillation light over a larger area has shown to achieve much better spatial resolution without the degradation of other factors. However, this so called monolithic detector design poses several challenges that are not yet fully understood and optimized. One challenge is the need for a detector calibration that provides reference detector signals at known gamma interaction positions. This is accomplished by moving a gamma ray beam on a narrow calibration grid over the detector and collecting the detector signals accordingly. To this point only pre-calibrated detectors provide the desired resolution. Especially towards the detector edges a strong spatial resolution degradation is otherwise typical. The second challenge is the development of algorithms that are able to correlate the provided light distribution with the gamma interaction location. In conclusion, the efficient collection and processing of calibration data and the development of well-performing algorithms are still not fully optimised and a challenge for the research community. For these reasons monolithic detectors are not yet implemented in commercial clinical PET systems while their performance is superior in almost all respects.

This dissertation investigates a monolithic detector design for the use in clinical PET scanners aiming at high spatial resolution. We use simulation and experimental data to evaluate our hardware and software design choices and identify the key factors that are relevant to reach the ultimate performance.

## 1.2 Outline

In Chapter 2 we start with a broad introduction into the field of medical imaging. Then PET and its sub-domains that are important to understand how the systems work are explained. We cover topics ranging from the clinical examination procedure to radionuclide production, from the physics behind PET to the techniques applied to generate PET images. Finally, the evolution of PET scanners from the first positron imaging to the large total-body PET scanners that have recently entered the market, are outlined.

In Chapter 3 the focus is on the most important component of the system, the gamma ray detector. We are starting with an overview of the milestones in PET detector development followed by a detailed description and analysis of the detectors' individual components. A comparison of pixelated and monolithic detectors and the event positioning algorithms that are required to determine the gamma interaction position in monolithic detectors are covered thereafter. The last section explains the simulation software and applied photon reflection models which are used extensively throughout this thesis.

In Chapter 4 we use optical simulations to investigate the detector performance under idealised and controlled circumstances. Several hardware related parameters that are difficult to study or cannot be studied in depth in experimental set-ups are looked at in this chapter. Some of the factors are the photodetector pixel size, the PDE, and the number of photodetector readout channels.

In Chapter 5 the prototype development and experimental performance evaluation is covered. Two positioning algorithms are tested, a MNN algorithm and a neural network. Next to the PSF evaluation we developed a bar phantom that gives a qualitative and quantitative measure of the detector performance in terms of spatial resolution and linearity. The DOI estimation, energy resolution and uniformity measurements are also part of this chapter.

In Chapter 6 we identify the factors that degrade the spatial resolution of the detector and discuss their origin and how they can be tackled. With the simulated and experimental results we have the data to understand the impact of factors that otherwise are difficult or impossible to investigate. In our set-up the four dominant factors are the calibration beam size, the impact of Compton scattered events, the photodetector PDE, and the influence of the intrinsic lutetium background radiation of the scintillation crystals.

In Chapter 7 we investigate to what extent the simulated calibration data can be applied to improve the performance of real detectors. At first we test whether the simulated calibration maps can be used to avoid the lengthy acquisition of calibration data from an experimental set-up. The resulting spatial resolution degradation is evaluated. In the second section of this chapter we train a neural network to estimate the scatter distance of gamma rays inside the crystal. Since the farthest scattered events are most difficult to position accurately they are removed from the dataset. The resolution improvement is investigated using a bar

phantom measurement.
Finally, in Chapter 8 an overview of our most important findings and a general conclusion is drawn along with future research possibilities.

# 2

# Positron Emission Tomography

## 2.1 Introduction

In this chapter we give an introduction into the world of medical imaging and provide the scientific background to grasp the physics and technological features of PET imaging. Furthermore, we discuss the factors that fundamentally limit the spatial resolution of a PET scan besides the detector spatial resolution. In the last section an overview of the technical evolution in PET over the last decades is given. After this chapter we will go into more detail on PET detectors specifically.

## 2.2 Medical imaging

Medical imaging modalities play a big role in the quick and reliable diagnosis of diseases at an early stage. The methods are various, some are used extensively in the clinical day-to-day life, others are only applied in very specific cases. Next to diagnosis medical imaging techniques are used to plan and monitor therapy. This is for example the radiation therapy plan for patients with cancer. Furthermore there is also interventional imaging to guide the insertion of an instrument, like a catheter or stent, into the patients body. This allows minimally invasive procedures. In the research context medical imaging is often used to get a better understanding of for example the functioning of the brain or the pathway of a certain administered drug. Most common

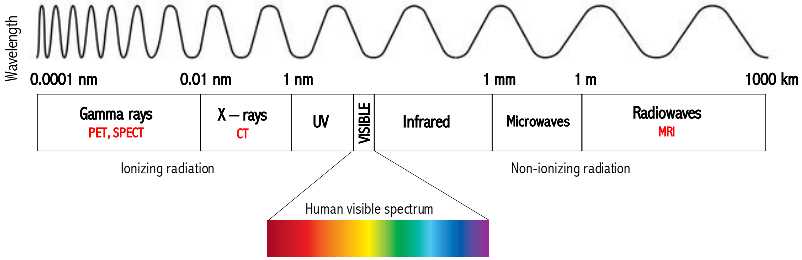

**Figure 2.1:** Overview of the radiation types and their wavelengths in the electromagnetic spectrum. Most medical imaging techniques are based on electromagnetic radiation.

examples of imaging modalities are ultrasound (US), x-ray radiography, x-ray computed tomography (CT), magnetic resonance imaging (MRI), positron emission tomography (PET) and single photon emission computed tomography (SPECT). They can be separated into two main groups, anatomical and functional imaging which are described below.

### 2.2.1 Anatomical imaging

Most commonly used imaging techniques are based on x-rays (Figure 2.1). The first *x-ray image* was conducted by the physicist Wilhelm Conrad Roentgen in December 1895. X-rays are produced by an x-ray tube and penetrate the tissue of the body part of interest. Depending on the density of the tissue the x-rays are attenuated. Bones are absorbing more radiation than for example soft tissue such as muscles or fat. The resulting image, called a radiograph, gives a planar 2D representation mostly used to diagnose fractures or examine bones or teeth, but also a wide range of other organs like lungs and breast can be examined. Angiography and fluoroscopy are two more examples of x-rays being used to visualize anatomic features. The first technique visualizes blood vessels by means of a contrast agent and the latter makes real time moving images of objects like the beating heart or the swallowing process.
When many radiographs of the same region are obtained from different angles a three dimensional image can be computed by image reconstruction algorithms. This technique is known as CT scan. The word tomography has its origins in ancient Greek where *tomos* means slice or section and *graphia* means to write or to describe. The 3D images can be examined by the radiologist in single slices. A CT scan is often used

to image organs in the pelvis, chest and abdomen where many overlapping structures make it difficult to evaluate a 2D radiograph properly. The range of applications is vast and often contrast agents are used to improve the image for angiographies or other tissue examinations.
X-rays are ionizing radiation that damage the human tissue when absorbed and should be avoided as much as possible, especially for pregnant women. Although the required x-ray doses could be reduced drastically in the course of time there are anatomical imaging devices that rely on other physical effects than the attenuation of x-rays in tissue.
MRI is an imaging technique based on strong magnetic fields of several Tesla and pulsed radio waves. All protons, also those present in human tissue, have a spin that produce a small magnetic moment. The protons are mostly hydrogen nuclei of water molecules. As demonstrated in Figure 2.2 a), the protons are initially randomly oriented. The strong magnetic field of the MRI scanner causes the polarization of a fraction of the protons to align parallel with that field while the rest of the protons aligns anti-parallel (Figure 2.2 b)). A radio frequency pulse de-polarizes the protons and forces it into a 90 or 180 degree realignment with the static magnetic field (Figure 2.2 c)). Once the pulse is turned off the proton follows its nature to align again with the magnetic field under the release of electromagnetic energy (Figure 2.2 d)). Gradients in the magnetic field allow the extraction of spatial information to form medical images. The released energy and speed of realignment is measured by a coil. Fourier transformation is applied to interpret the electrical signal and determine the quantity and environment of the protons and therefore tissue type. Functional magnetic resonance tomography (fMRI) is a brain-specific functional imaging technique. While regular MRI measures anatomical structures fMRI can visualize physiological functions of the human body. The clue here is that e.g. neuronal activity needs oxygen as a resource. Oxygen is carried by haemoglobin, a component in the blood. Haemoglobin that carries oxygen has other magnetic properties than de-oxygenated haemoglobin. This difference can be measured using fMRI and can be linked to the brain activity (blood oxygen level dependent (BOLD) contrast).
*Sonography* also known as ultrasound, is another example of anatomical imaging without ionizing radiation. Per definition ultrasound is a sound with frequencies above those that a human can hear. (Sounds below the audible frequencies are called infrasound.) Sonography (lat. sonos: sound, tone) however is the actual name for the medical imaging

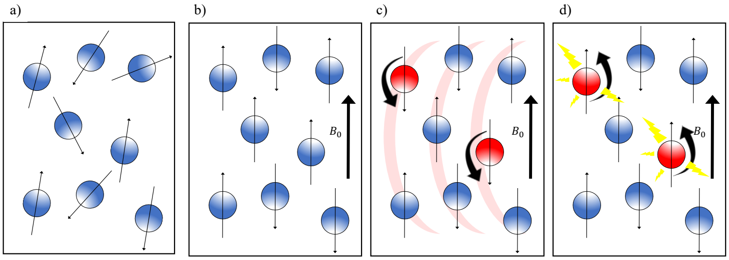

**Figure 2.2:** MRI principles. a) The proton orientation is random, when no magnetic field is applied. b) When the main field $B_0$ is applied, the protons align parallel or anti-parallel to that field. c) The radio-frequency pulse is applied and changes the spin of a fraction of protons. d) After the RF pulse stops these protons return to their previous orientation under the emission of radio waves.

technique where a sound pulse is sent into the tissue using a probe. Thereafter the echoes of the sound are recorded and give insight in the properties of the tissues in which the sound waves were reflected. This method is used in a variety of diagnostic and therapeutic procedures, mostly for soft tissues and structures that are close to the surface. It is very low-cost and not harmful for the patient. Mostly sonograms are known from obstetrical sonography meaning the visualization of the embryo or foetus in the woman's womb. Additional (functional) techniques using ultrasound are for example Doppler ultrasonography which uses the Doppler effect to measure the relative velocity of blood to examine the heart.

### 2.2.2 Functional imaging

An anatomical and morphological change in the body such as a tumour manifests already a relatively long presence of disease. Many diseases can be characterized much earlier by biochemical changes on the cellular level. Medical imaging techniques that allow to investigate biological processes (e.g. blood-flow or metabolism) are called functional imaging. Functional imaging at the cellular and molecular level is called molecular imaging.

Functional imaging can be performed to some extent with most imaging modalities such as CT (CT perfusion), fMRI, sonography (Doppler and contrast enhanced ultrasound) and optical imaging, some of which were already mentioned in the previous section. However, nuclear medicine imaging techniques are the most sensitive and quantitative ones while allowing a visualization of the deep structures. fMRI also allows visualisation of deep structures but is less quantitative because it is only sensitive to relative changes. The variety of radioactive tracers to target different metabolic processes is large and only very small quantities are needed. The two main modalities in this field are PET and SPECT. In both cases radio-pharmaceuticals also known as tracers are injected in the human body that take part in a biological process. A tracer is a molecule of which one stable atom is substituted by one of its radioactive isotopes. Stable and unstable (radioactive) isotopes act in a similar way and allow us to track the molecules by measuring the emitted photons of the radioactive decay. In a single photon emission tomography (SPECT) system the emitted gamma rays are detected by one or multiple gamma cameras that rotate around the patient and detect the radiation from different angles. From the acquisitions from different angles one can obtain three dimensional images by applying inverse Radon transformation or iterative reconstruction (described in Section 2.3.5). These images then give information about the tracer distribution inside the patients body. The gamma cameras use a collimator that allow only photons that come from a certain direction to enter the detector. This drastically lowers the camera sensitivity. In positron emission tomography (PET) imaging a different effect is used to obtain directional information avoiding the use of a collimator, therefore PET has higher sensitivity and also spatial resolution. The PET principles are explained in detail in Section 2.3.

### 2.2.3 Multi-modality imaging

Nuclear imaging techniques such as PET and SPECT are highly sensitive and quantitative for biochemical and molecular studies, but the missing anatomical information makes the interpretation of these scans challenging. In the past, pre-acquired CT (or MRI) scans were co-registered with for example a PET scan to avoid misinterpretation of radio-tracer distributions. While this works well for static, not-moving, organs such as the brain that can be fixed in a certain position, the image co-registration of other organs becomes difficult. Inaccuracies are induced by the patient movement, moving from one bed to another, but also respiratory and cardiac movement. To improve the co-registration

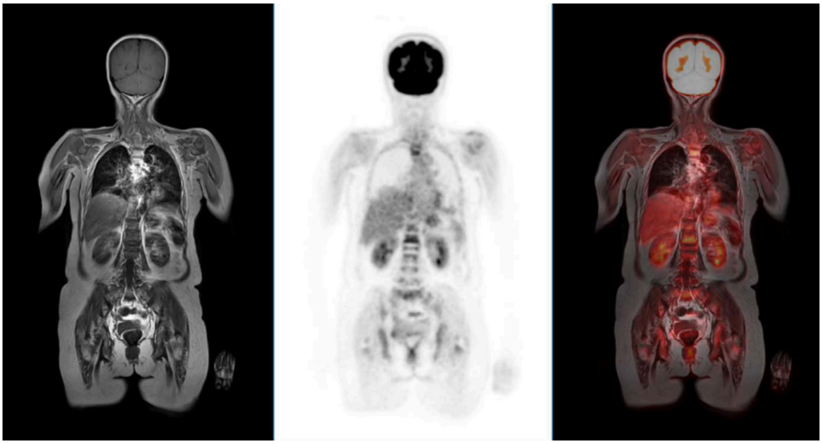

**Figure 2.3:** FDG-PET/MRI scan a) T1-weighted MR, b) PET c) PET/MR. Image courtesy of Dr. Joshua Schaefferkoetter, Clinical Imaging Research Centre, Singapore. [1]

sequential scans can be done without moving the patient to a different bed. Hybrid systems integrate all detectors and electronics inside a single imaging unit and allow controlling the imaging devices with a common software interface. Often combined are SPECT/ CT, PET/ CT, SPECT/ MRI, PET/ MRI. Nowadays PET is always combined with CT in clinics. The typical PET/CT procedure is described in Section 2.3.1.

## 2.3 PET imaging

In PET the patient is injected with a radioactive tracer (see Figure 2.4) that accumulates in tissue depending on the local metabolic activity. The tracers in PET are positron ($\beta^+$) emitting radionuclides. The positron travels a short path in the tissue before it annihilates with an electron into two 511 keV gamma rays travelling in opposite directions. A coincident detection of the two gamma rays in a small enough time window of nanoseconds allows to draw a line of response (LOR). Millions of LORs are then used to reconstruct a PET image. To elaborate more on the background of PET imaging we explain first the clinical routine of a PET scan as well as several different types and applications of PET examinations. Further, the production of the radionuclides used for PET

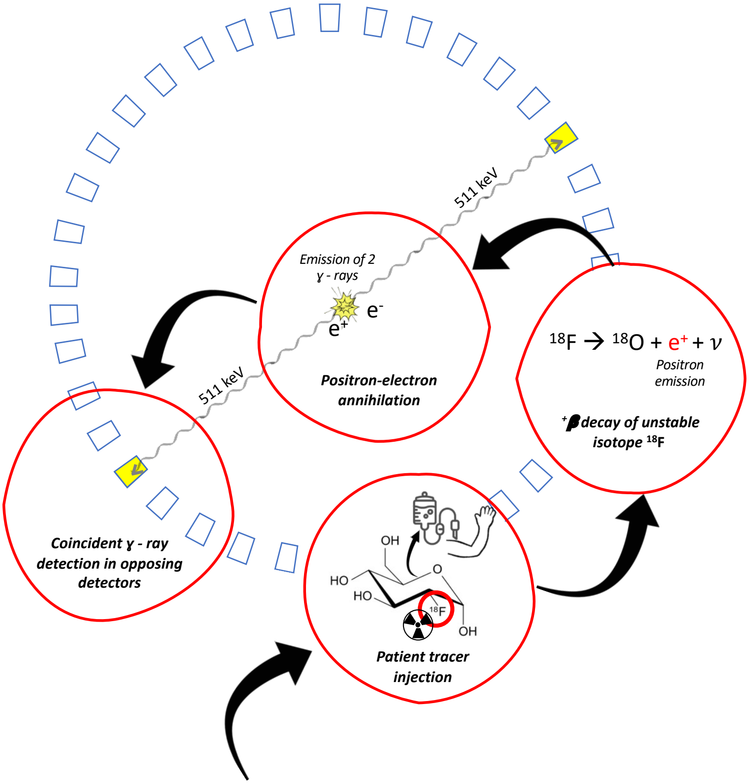

**Figure 2.4:** In PET the patient is injected with a radioactive tracer (here as an example $^{18}F$-FDG). The tracer is taking part in the sugar metabolism in the human or animal and emits positrons through $\beta^+$ decay of $^{18}F$. The positron annihilates with a surrounding electron resulting in two 511 keV gamma rays that travel in opposite directions. Ideally both are detected by the detectors.

is explained. After that the physical principles of PET are explained followed by a discussion on how the physics limit the obtainable spatial resolution. The data acquisition and methods used to reconstruct a PET image are covered as well. Finally, two specific techniques are elaborated that have a direct or indirect influence on the obtainable spatial resolution. First, the role of gamma arrival time measurement known as TOF-PET, and second, the importance of DOI measurement.

### 2.3.1 Clinical PET scan

A PET exam is usually taken in the nuclear medicine department of a major, well-equipped hospital. A radio-tracer injection is performed with an intravenous catheter on the arm. The vast majority of scans is done with the tracer [$^{18}$F]-FDG which is a glucose analogue. In this case the patient should be sober six hours before the exam. The glucose metabolises in the whole body and accumulates in tissues that have a high sugar consumption. These are organs like the brain or the heart but also tumours have a high metabolism and sugar accumulates there. After 30-60 minutes the patient is moved to a sequential PET/CT scanner. The interpretation of the PET images is supported and more accurate when an anatomical image from the CT is taken at the same exam. The two scanners are often combined into one unit and executed sequentially. After the CT scan has been performed, taking around 2 minutes, the PET scan starts, taking 20-30 minutes. After the exam the patient does not have to follow specific restrictions. The radio-tracer will decay and also be flushed out through urine and stool. The medical doctor will examine the three-dimensional PET/CT images stored in the picture archiving and communication system (PACS). With PACS, medical images and reports can be accessed digitally from secured networks and make the distribution and display very efficient. The universal format for PACS is digital imaging and communications in medicine (DICOM). DICOM has been adopted universally between different manufacturers and most hospitals. Most commonly done PET/CT scans are [$^{18}$F]FDG PET/CT, [$^{18}$F]Choline PET/CT, [$^{18}$F]FET PET/CT and PSMA PET/CT. Their application and working principles will be explained in more detail in the following paragraphs.

#### [$^{18}$F]FDG PET/CT

[$^{18}$F]FDG PET/CT is mostly used in the field of neurology and in the field of oncology to detect tumours. [$^{18}$F]FDG or fluorodeoxyglucose is a glucose analogue with a substitution of the normal hydroxyl group with fluorine-18, a positron emitter. Once injected the tracer has a high uptake in cells that have a high glucose consumption. Next to the brain, brown adipose tissue and the kidneys, cancer cells do have high glucose uptake. [$^{18}$F]FDG is therefore an outstanding tracer for tumour detection. Around 90% of all PET scans are of this type.

### [$^{18}$F]FET PET/CT

[$^{18}$F]FET PET/CT stands for [$^{18}$F]-Fluoroethylthyrosine PET/CT. FET is a radioactively labelled amino acid. It has a high specificity for the representation of brain tumours and is used to differentiate them from healthy, inflammatory, irradiated/scarred brain tissue e.g. in the context of radiation therapy or surgical planning and especially for the early diagnosis of recurrences. The FET tracer is also used to differentiate high-grade from low-grade tumours using dynamic PET. Amino acids are the building blocks from which proteins are formed. These building blocks are increasingly taken up by brain tumours, whereas the uptake of amino acids in healthy brain tissue is low.

### PSMA PET/CT

The tracer for PSMA PET/CT imaging is $^{68}$Ga or $^{18}$F labelled PSMA-11. This tracer binds to the prostate-specific membrane antigen, a transmembrane protein that occurs in the prostate. The expression of this protein is increased in multiple malignancies, most pronounced in prostate cancer.

### [$^{18}$F]Choline PET/CT

[$^{18}$F]-Choline PET/CT is used when a clarification of a parathyroid adenoma in hyperparathyroidism (over-active parathyroid gland) is needed. Radioactively labelled choline is administered to make the diseased tissue visible. There is an increased growth and metabolism of the cells, which then take up more choline than healthy cells.

These were some of the most common PET examinations with their different tracers. However, the list of PET tracers being used and researched keeps growing. In 2018, a promising new radio-tracer called FAPI (fibroblast-activation protein inhibitor) was developed targeting a protein that is overly expressed in cancerous tissues. The tumour delineation and image contrast stand out and $^{68}$Ga-FAPI-PET/CT allows to visualise almost 30 different cancers (Figure 2.5) [2, 3]. FAPI-PET/CT does not require specific patient preparation and uptake time reduces to 10 minutes improving work-flow and patient comfort.

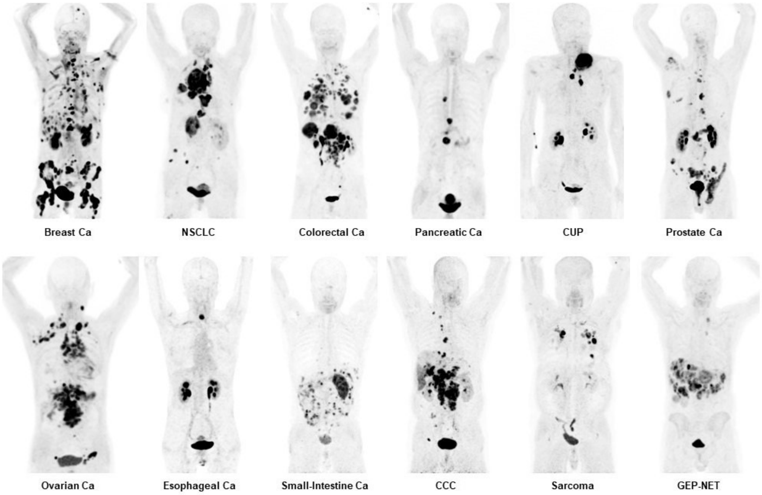

**Figure 2.5:** Radio-tracer distributions of 12 different cancers with FAPI-PET/CT. (Ca = cancer; NSCLC = non-small cell lung cancer; CUP = carcinoma of unknown primary; CCC = cholangiocarcinoma; GEP-NET= Gastroenteropancreatic neuro-endocrine tumour). This research was originally published in JNM. Frederik Giesel et al. Intensity of tracer-uptake in FAPI-PET/CT in different kinds of cancer. J Nucl Med. 2019;60:289. © SNMMI [4].

### 2.3.2 Radionuclide production

The radionuclides occurring in our natural environment are ones with a very long half-life and no important role in human metabolism and physiology. Therefore all radionuclides used in nuclear medicine are produced artificially by bombarding stable atoms with neutrons or protons leading to the formation of unstable, radioactive nuclei. For clinics today radionuclides are produced in a cyclotron or a specific generator. The most commonly used radioisotope $^{18}$F has a half-life of 109.8 minutes which gives PET facilities just enough time to have it delivered from the production site. However, more and more hospitals make use of cyclotrons installed directly on-site producing their own tracers. Radioisotopes having a very short half-life must be produced on-site. Examples are $^{15}$O with a half-life of 2 minutes, $^{13}$N with 11 minutes, and $^{11}$C with 20 minutes.

Typical isotopes that are produced by a generator are $^{82}$Rb produced by a $^{82}$Sr/Rb generator with a half-life of 75 seconds and $^{68}$Ga produced

by a $^{68}$Ge/Ga generator with a half-life of 68 minutes.
The biological function of the radionuclide element itself is interesting only in very limited cases e.g. the iodine uptake in the thyroid using $^{131}$I (or $^{124}$I). In most cases the radionuclide acts as a label of the compound that is of interest, such as the glucose labelled $^{18}$F. A radioisotope or radio-pharmaceutical must furthermore meet many practical requirements in order to be used in clinics [5]:

- type and energy of emission: 50-600 keV (high enough to escape the human body and low enough to meet the detection spectrum of the hardware)
- physical half-life: seconds to days (ideally minutes to hours)
- high specific activity: to not disturb the biological system
- high purity: high fraction of desired radioactivity
- good chemical properties to bind to the molecule of interest
- feasible production cost and complexity
- no cascade (decay product is stable).

### 2.3.3 Physical principles and limitations

In this section the most relevant physical principles in PET are explained in detail. Finally we discuss how these factors limit the spatial resolution that can ultimately be achieved with PET.

#### Positron emission and annihilation

The principle upon which PET is based is positron emission followed by a positron-electron annihilation. First the radionuclide of the PET tracer transforms one of its protons $p$ into a neutron $n$ under the emission of a positron $e^+$ and a neutrino $\nu_e$ (Figure 2.6).

$$p \rightarrow n + e^+ + \nu_e \tag{2.1}$$

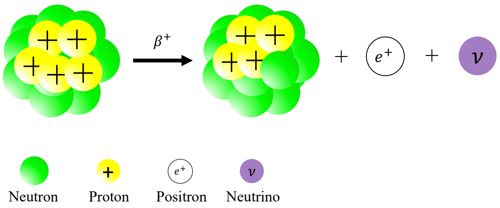

**Figure 2.6:** $\beta^+$ decay. A proton in the nucleus converts into a neutron under the emission of a positron and neutrino.

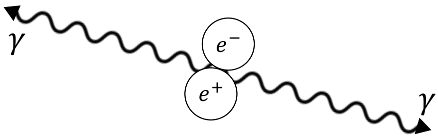

**Figure 2.7:** Annihilation. After the positron travels a certain distance it combines with an electron in the surrounding tissue and both particles convert into two gamma photons of 511 keV travelling anti-parallel.

The positron has a kinetic energy of a few MeV. Before the positron captures an electron and forms a positronium it reduces its energy by travelling a certain distance called the positron range. Depending on the initial kinetic energy of the positron and the number of electrons of the surrounding material the travel path can vary (see 'Mean range in water' in Table 2.1). The annihilating radiation consists of two gamma rays.

$$e^+ e^- \rightarrow \gamma\gamma \tag{2.2}$$

The two gamma rays have a discrete energy of 511 keV each and travel in opposite directions (180°) (Figure 2.7). These two particles arrive at opposing detectors in coincidence, meaning, at (almost) the same time.

### Photon interaction with matter

The PET detector will be explained in detail in the next chapter, however, the rough principle is that the high energetic 511 keV gamma photon is stopped by a dense scintillator which converts the gamma energy

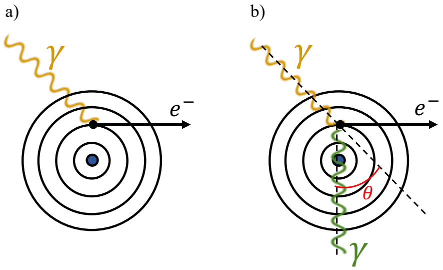

**Figure 2.8:** Interaction of a gamma ray with an atom a) photoelectric interaction and b) Compton scattering.

proportionally into light photons. These photons are then detected by a photodetector. The different types of scintillators and photodetectors and their properties are explained in detail in Section 3.4 and 3.5. The attenuation properties of the scintillator can be calculated with the Beer-Lambert law (Equation 2.3) where N is the number of gamma photons that are not absorbed after travelling through a scintillator of thickness x and $\mu$ is the linear attenuation coefficient. The linear attenuation coefficient is dependent on the scintillator material and the gamma energy. $N_0$ is the initial number of gamma photons.

$$N(x) = N_0 e^{-\mu x} \tag{2.3}$$

Below 1022 keV there are two main interactions of photons with matter in the PET detector: photoelectric and Compton interactions (Figure 2.8). The photoelectric interaction is typically occurring between low-energy gamma rays and a material, such as the scintillator. The full energy of the gamma photon is transferred to an electron in the material. The electron is ejected from its atomic shell with an energy proportional to the initial gamma photon energy. The energy is transferred to the detector and can be used to identify the photon energy. A photon can also scatter by an electron and lose some of its energy depending on the scattering angle. This process is known as Compton scattering. The photon continues its trajectory in a direction with angle $\theta$ relative to the original direction.

$$E' = \frac{E}{1 + \frac{E}{m_0 c^2}(1 - cos\theta)} \tag{2.4}$$

$E'$ is the rest energy of the gamma photon while E is the incident energy of the incident gamma photon. $\theta$ is the scatter angle. $m_0$ is the rest mass of the electron, $c$ is the speed of light in vacuum.

### Fundamental resolution limits of PET

In this section we discuss three factors that cause a fundamental limit in the spatial resolution that a PET system can theoretically reach. These factors are the positron range, the photon accolinearity and the intrinsic detector resolution.
Positron range: Depending on the type of radioisotope the initial kinetic energy of the positron after emission that determines the travel path is different. The positron range induces blurring proportional to the travel distance. For example the commonly used tracer $^{18}F$ induces blurring of about 0.5 mm FWHM in water [6–8]. Most other radionuclides have a larger positron range up to several millimetres. In Table 2.1 the most relevant radionuclides for PET are listed including their mean travel path in water and other important characteristics.

**Table 2.1:** Radionuclides used in PET with their half-life, maximum energy, mean travel path and production site.

| Isotope | $t_{1/2}$ [min] | $E_{max}$ [MeV] | Mean range in water $R_{range}$ [mm] | Production |
|---|---|---|---|---|
| $^{11}$C | 20 | 0.959 | 1.1 | on-site cyclotron |
| $^{18}$F | 110 | 0.633 | 0.5 | cyclotron |
| $^{22}$Na | $1.37 \cdot 10^6$ | 0.55 | 0.5 | cyclotron |
| $^{68}$Ga | 67.8 | 1.89 | 2.9 | generator |

Non-collinearity: Non-collinearity describes the slightly non-collinear annihilation of the two 511 keV gamma rays. The electron and positron are not fully at rest leading to an emission of 180° with a slight deviation that depends on the kinetic energy of the positron. For $^{18}F$ the non-collinearity is $180 \pm 0.2^\circ$. This causes Gaussian blurring that is proportional to the radius of the system r. The larger the distance between the two detectors the larger the impact of non-collinearity. It can be described as $R_{180^\circ} = 0.0044 \cdot r$ mm FWHM.
Intrinsic detector resolution: For preclinical $^{18}F$ scans this leads to a best

possible system spatial resolution of around 0.4 mm while for a human system ($d = 80cm$) around 2 mm should be feasible. This resolution limit is not yet achieved by the scanners that exist. A major limiting factor is the intrinsic detector spatial resolution $R_{int}$ that dominates the system spatial resolution. The general formula to calculate this limit is

$$R_{sys} \approx \sqrt{R_{det}^2 + R_{range}^2 + R_{180^\circ}^2} \tag{2.5}$$

where for monoliths $R_{det} \approx \frac{R_{int}}{\sqrt{2}}$, the positron range $R_{range}$, and the non-collinearity $R_{180^\circ} = 0.0044 \cdot r$. In Figure 2.9 the dependencies are plotted. However, in practice spatial resolution is also limited by the small number of detected events in a PET scanner leading to rather low SNRs. A low SNR leads to degraded image resolution and negatively impacts the lesion detectability [8]. The SNR is proportional to the number of detected events $n$,

$$SNR \propto \sqrt{n}, \tag{2.6}$$

and $n$ is defined as:

$$n \approx kAG\varepsilon^2 T \tag{2.7}$$

where $A$ is the activity in the FOV, $G$ is the geometric coverage of the scanner, $\varepsilon$ is the detector efficiency and is squared because both gamma photons are required to build a LOR, $T$ is the acquisition time and $k$ is specific to the patient (how many events are scattered and absorbed in the body tissue). Improving SNR can also be achieved by including TOF (see Section 2.3.6).

In conclusion, to reach the ultimate spatial resolution one should keep in mind the positron range of the radiotracer, the system diameter and the detector intrinsic resolution. Note that if the detector resolution is improved at the cost of detector efficiency/sensitivity, the SNR is degrading and is also degrading spatial resolution. Detector design is discussed in Section 3.6.

### 2.3.4 Event types in annihilation coincidence detection

PET systems record an event when two gammas are detected in two detectors in a defined coincidence time window. These events are called

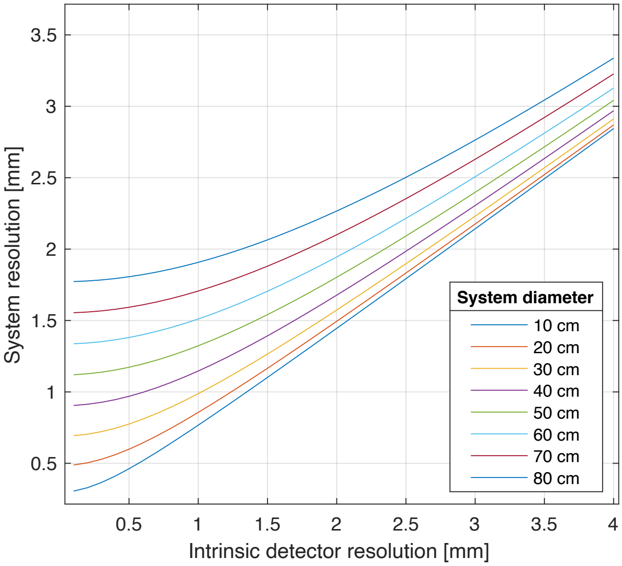

**Figure 2.9:** Fundamental spatial resolution limit in F-18 PET imaging dependent on the system diameter and the intrinsic detector spatial resolution.

*prompt coincidences*. Ideally all events are true coincidences i.e. the detected gammas are originating from the same annihilation event and have not scattered on their path to the detectors (Figure 2.10). If one or both gammas have scattered before detection the drawn LOR is not accurate anymore. This is called a *scattered coincidence*. A coincidence can also be triggered by two gammas from different annihilation events. This is called a *random coincidence*. The true coincidence rate is calculated as:

$$R_{true} = R_{prompt} - R_{scatter} - R_{random} \tag{2.8}$$

A PET specific system quality measure is the noise equivalent count rate (NECR), which is defined as the same statistical noise level as the observed count rate after random and scattered coincidences have been corrected for. The NECR accounts for the additional statistical noise from the correction for random and scattered coincidences [5]. It is usually plotted as a function of the activity since the random coincidence rate and dead time count losses are activity dependent. The measurement allows a comparison between different PET systems and

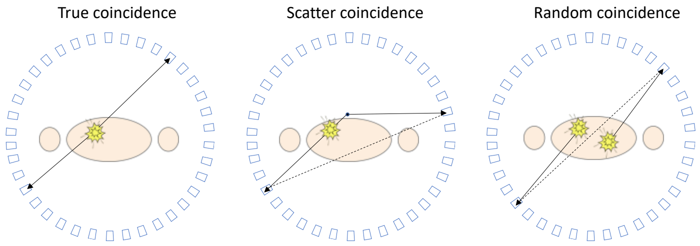

**Figure 2.10:** True, scatter and random coincidences. Scatter and random coincidences contain inaccurate positional information that lead to a uniform background signal which degrades the image contrast.

the optimization of new systems.

$$NECR = \frac{{R_{true}}^2}{R_{true} + R_{scatter} + R_{random}} \tag{2.9}$$

### 2.3.5 Data acquisition and image reconstruction

Two-dimensional radiographic images have the problem that multiple anatomical structures overlap each other which make it difficult to interpret these images. A set of radiographic images from different acquisition angles can give the viewer more insight. However for some structures, for example deep in the chest, there might always be overlaying structures as in this case the rib cage. The solution is tomographic imaging which allows to look at a 3D object in the form of slices including techniques such as x-ray CT, SPECT and PET. To obtain sliced images the object needs to be scanned from multiple angles also known as projection angles. Mathematical reconstruction algorithms are then applied to either reconstruct the emissions of radionuclides as in SPECT and PET or the transmission of x-rays (CT). Two classes of reconstruction techniques are outlined below: iterative and analytical reconstruction.

#### Analytical reconstruction

The simplest form of tomographic image reconstruction is back-projection. Here it is assumed that each voxel in an LOR contributes equally to the integrated line profile between the two detector pairs. Each LOR is thus plotted with constant values along its path. In the final image one

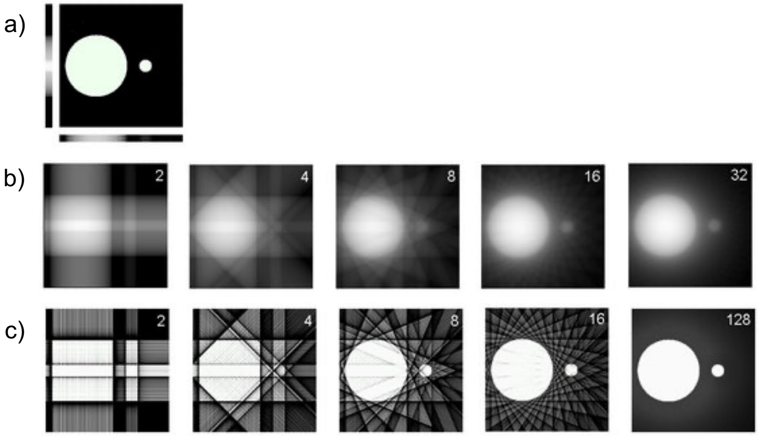

**Figure 2.11:** Analytical reconstruction demonstrated on a phantom seen in a). Simple backprojection with different number of projection angles in b). Filtered backprojection can be seen in c) [9].

single voxel has the intensity of all LORs that intersect with this given voxel. The larger the number of sampled angles and sampling points the better the image resembles the original image. The main drawback of BP is blurring of the image data. The blurring effect is equivalent to a cone shaped filter function $h(x,y) = (x^2 + y^2)^{-1/2}$. Applying the inverse of this filter to the projections can correct for the blurring (see Figure 2.11). This is called filtered back-projection.

### Iterative reconstruction

A more advanced technique to reconstruct image data to a tomographic image is iterative reconstruction. A first estimate of the image (which could be as simple as a uniform image) is made and forward projected. The projections are compared to the original projection data p(r,$\phi$). The error is large in the first iteration, but the differences (or ratios) are used to update the initial image estimate. Once the difference between the projection data of the reconstructed image and the original projection data is sufficiently small the iteration is stopped. Although iterative reconstruction is computationally much more expensive than analytical reconstruction it has become the standard technique in PET through improved computational capacities. The most common iterative reconstruction algorithm is the maximum likelihood expectation maximization (MLEM) algorithm.

### 2.3.6 TOF-PET

A PET system that measures the difference of the arrival times of the two annihilation gamma photons at coincident detectors is called TOF-PET. The more accurate this time can be measured the more precisely the position of the positron annihilation along the LOR can be determined. Theoretically, a pair of detectors that detect exactly the same arrival time of two photons lead to the conclusion that the annihilation point must be in the center of the LOR. However, there is a so called coincidence timing resolution (CTR) which is the uncertainty in the measured arrival time that leads to a position uncertainty $\Delta x$ along the LOR. The best CTR reached in an experimental set-up is about 58 ps translating to 8.7 mm uncertainty on the LOR [10]. The corresponding formula is:

$$\Delta x = \frac{CTR}{2} \cdot 10^{-10} \cdot c \tag{2.10}$$

with the speed of light c being about $300 \cdot 10^{-6}$ m/s. The uncertainty for different CTRs is plotted in Figure 2.12.

First clinical TOF-PET reached only 500-600 ps [11, 12], but improved gradually over time with the introduction of faster scintillators, improved electronics and the replacement of photomultiplier tubes (PMTs) with SiPMs [13, 14]. The latest TOF-PET on the market (Siemens Biograph Vision) reaches 210 ps corresponding to about 3 cm positioning uncertainty [15]. In preclinical PET the positioning uncertainty is too large compared to the field of view (FOV) and therefore TOF is typically not used. The 10 ps TOF challenge (https://the10ps-challenge.org/) is the current effort of the PET community to reach the challenging goal of reducing the CTR down to a point where the discrete location on the LOR could be distinguished. At 10 ps this is about 2 mm. At this level reconstruction-less PET could open doors for novel applications and general improvement of resolution effective sensitivity and SNR [16]. An example of how the inclusion of TOF improves image quality can be seen in Figure 2.13.

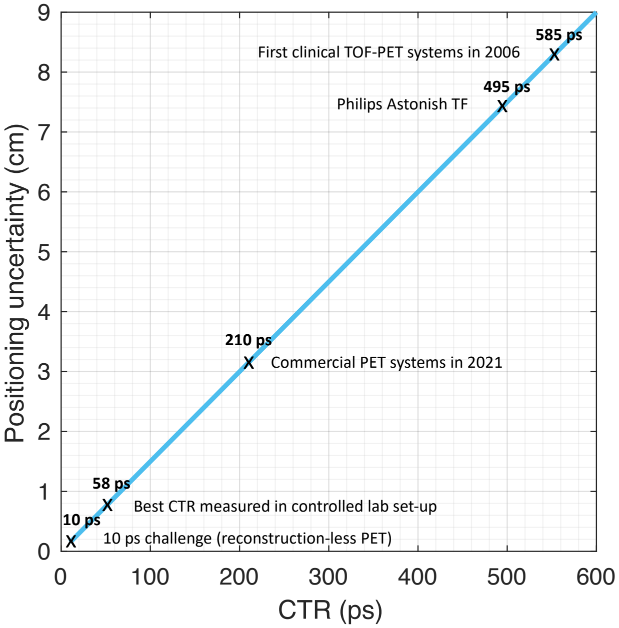

**Figure 2.12:** The TOF positioning uncertainty dependent on the system CTR according to Formula 2.10.

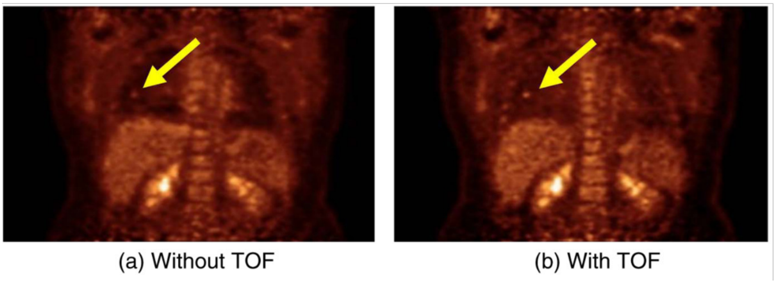
(a) Without TOF

(b) With TOF

**Figure 2.13:** a) Image including no TOF information b) TOF information is included in the reconstruction. Images are acquired on a Philips TOF PET scanner. Images are courtesy of Dr Joel Karp, Philadelphia [1].

### 2.3.7 Depth of interaction (DOI) in PET

At the edge of the FOV and at oblique imaging planes the so called parallax error is induced leading to a degradation of spatial resolution. The gamma photon is entering the crystal at an oblique angle which can lead to the energy deposition in an adjacent detector pixel, instead of the one that it initially entered (Figure 2.14). Consequently the LOR cannot be formed accurately. The width of the LOR increases with angle $\theta$, the length x and width d of the scintillator according to the following formula:

$$d^{'} = d\ cos\ \theta + x\ sin\ \theta \tag{2.11}$$

Wider or shorter pixels (increasing d or decreasing x), reduce parallax effects, however this is only at the cost of either spatial resolution or sensitivity. The estimation of the DOI to reduce parallax error has been studied extensively. In pixelated detectors several designs have been developed that allow some sort of extraction of DOI (phoswhich, dual-ended readout) [17, 18]. Especially in dedicated organ scanners where the small bore induces oblique incidence angles DOI improves spatial resolution for larger radial distances and provides a more uniform resolution across the bore [19].

In monolithic detectors an oblique incidence angle induces a similar effect. If the gamma deposits its energy deeper inside the crystal, the estimated 2D interaction position is not equal to the entrance position anymore. Monolithic detectors, however, can easily extract DOI information without additional hardware or design alterations. This is possible because the width of the measured light distribution correlates to the DOI. It also needs to be said that, the better the intrinsic detector resolution the more important the DOI performance gets [19]. DOI is furthermore of interest for TOF-PET to correct for time walk inside the detector [16].

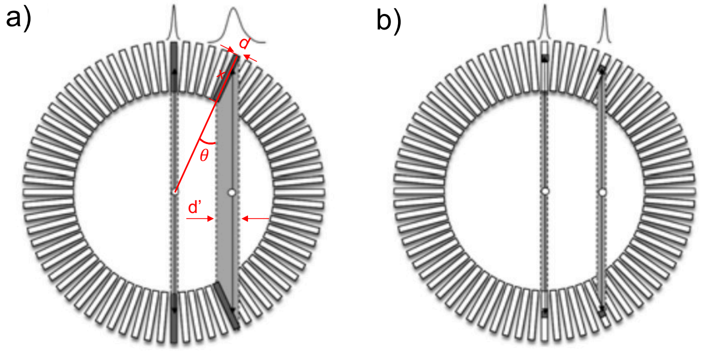

**Figure 2.14:** Importance of DOI in PET scanner a) parallax error without DOI determination b) reduction of parallax error by DOI encoding [20]

## 2.4 Technical evolution in PET

The following sections will give a brief overview of the milestones in the development of PET with a focus on the developments relevant to this thesis.

### 2.4.1 Positron imaging

Coincidence detection to capture positron annihilation in medicine was independently reported in 1951 by Wrenn et al. [21] as well as Sweet [1, 22]. In 1953, Brownell and Sweet published a more detailed report on the coincidence detection for localizing brain tumours [23]. The step from two coincident detectors to a full ring of 32 NaI detectors was made in 1961 [24]. In the 1970s the so called positron camera was developed by Burnham and Brownell which enabled the use of smaller scintillation crystals by a shared photodetector scheme reducing the number of needed photodetectors and improving spatial resolution [25]. To this point the acquired images were still 2-dimensional and not tomographic. Only after the development of CT in 1973 [26, 27] and SPECT, first PET reconstructions were realized.

### 2.4.2 First clinical PET

The first full PET systems named Positome [28] and PETT [29] appeared and the latter entered the clinical market in a EG&G ORTEC - collaboration for the first time in 1979 [30, 31]. Later PET systems employed bismuth germanium oxide (BGO) as a scintillator rather than NaI. It is more dense than NaI and not hygroscopic and therefore allows much easier assembly. In 1986 Casey and Nutt published their work on a matrix assembly of smaller scintillation crystals put into a block with a shared photodetector coupling. This so called block detector design marks a milestone in PET detector development [32]. The first block detector was an 8 x 8 array of BGO crystals coupled to four PMTs. It improved the spatial resolution while reducing the number of photodetectors (further discussed in Section 3). The next step was the extension from one ring to several rings of block detectors. First versions were using septa (tungsten shielding) in between each ring. This allowed to detect only coincidences within the plane of that detector ring improving the rate of true coincidences and reducing dead time. However the system sensitivity suffered significantly from the tungsten septa. The next milestone for PET was removing the septa and acquiring all possible coincidences across several detector rings [33]. First scanners made the septa optional by making them retractable, however techniques were developed to work PET from now on in fully 3D-mode. In 1998 FDG-PET scans were first reimbursed in the US.

To further improve spatial resolution by using finer segmented pixels the light output of BGO was not high enough. The smallest feasible pixel size at that time was about 6 mm x 3 mm. A brighter crystal was needed to guarantee that the crystal encoding would still be reliable. The engineering of lutetium oxyorthosilicate (LSO) [34] in 1992 provided a scintillator that is not only five times brighter than BGO but also its decay time with 40 ns is reduced by a factor of 7.5 compared to BGO. In 1999 the first system using LSO was commercialized, the ECAT ACCEL. A variant of LSO including yttrium called LYSO (frequently used today) was developed shortly after and offers similar characteristics. The new scintillators allowed smaller crystal pixels leading to improved spatial and energy resolution. The fast decay time decreased the detector deadtime and for the first time the TOF of the two gamma rays could be measured. This technique allows to decrease the range of possible annihilation positions along the LOR to a few centimetres which improves the

SNR ratio. The very first TOF-PET scanner were built by the Swedish company Scanditronix, nowadays GE, late in 1980s and based on BaF2 material which delivers around 500 ps timing resolution. TOF-PET systems came back in 2008 with the Philips Gemini [35] and Siemens Biograph mCT(2010) [36]. A detailed overview of TOF-PET in given in Section 2.3.6.

### 2.4.3 Preclinical PET

Preclinical PET scanners which are scanners mostly used for studies with animals (small rodents) started evolving in the beginning of the 90s with the same detectors used in human scanners. This led to limited spatial resolution for rodents and the need for dedicated small animal PET detectors appeared. In 1997 Cherry et al. [37] developed the first preclinical PET device called the microPET with dedicated detectors which was also commercialized. The LSO version of this scanner achieved spatial resolutions smaller than 1 mm. The first scanner to use semiconductors instead of PMTs is also a preclinical PET system [38] making PET detectors MR-compatible. Only 10 years later semiconductors appeared in clinical imaging. Although the preclinical imaging market is much smaller than the clinical it has significant impact on scientific research translating to the clinical world. The huge improvement of preclinical PET systems over the last two decades can be seen in Figure 2.15.

### 2.4.4 PET/CT

The hardware fusion of PET and CT combines the low resolution functional image with the high-resolution anatomical images. Not only does it help the radiologist to interpret the tracer distribution in the patients body but also the CT system is used to acquire attenuation correction factors to be applied to the PET data. Technically the two systems are simply put in sequence making almost simultaneous scans possible without moving the patient. In 2001 two PET/CT systems entered the imaging market (GE Discovery PET/CT and Siemens Biograph PET/CT). A major economical advantage that led to the extinction of PET as a standalone in clinics within 4 years [1] was the scanning time reduction. It resulted from the attenuation correction done with the CT in 1-2 minutes instead of several minutes with the PET system. Furthermore, Philips, Canon and more recently United Imaging

1997

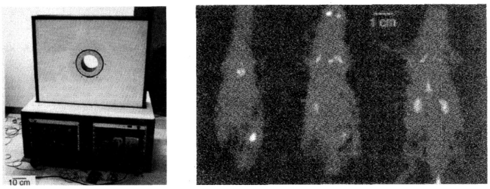

microPET

Coronal sections through a mouse. Brain, heart, kidneys and bladder are clearly seen.

2004

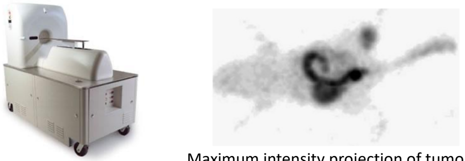

Philips MOSAIC

Maximum intensity projection of tumour-bearing mouse.

2011

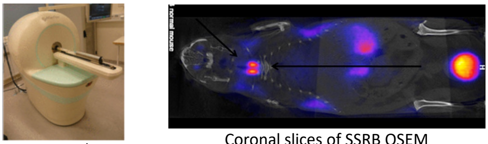

nanoPET/CT

Coronal slices of SSRB OSEM reconstructed image of mouse.

2016

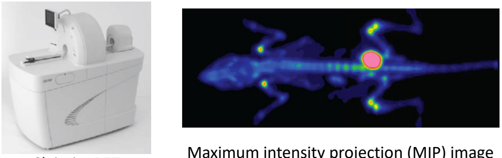

ClairvivoPET

Maximum intensity projection (MIP) image of mouse scanned using the ClairvivoPET.

2017

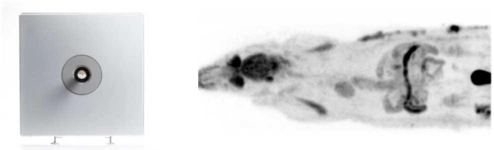

Beta cube

Rat – PET – 10.85 MBq F-FDP MIP

**Figure 2.15:** Preclinical imaging improvement. The first dedicated PET scanner in 1997 is called microPET [37]. Since then many preclinical scanners have entered the market [39–43]. Over time the image quality has improved while the scanner dimensions have decreased to bench-top systems. The latest technology PET scanner is the beta-cube from MOLECUBES with a system size of 54 x 56 x 54 $cm^3$ and sub-mm spatial resolution [44].

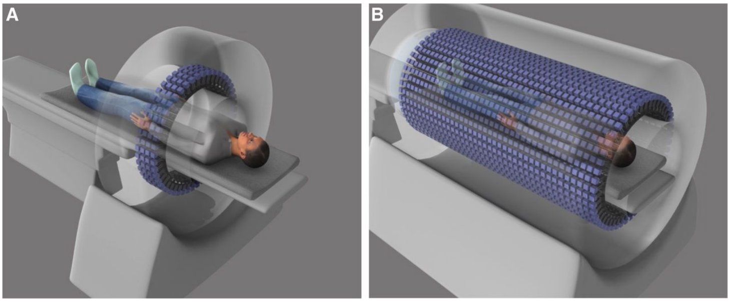

**Figure 2.16:** A) Conventional PET scanner with an axial FOV of 15-30 cm and B) a total-body PET scanner with total-body coverage of almost 2 m [45].

Healthcare offer PET/CTs. Worldwide around 5000 PET/CT scanners are installed [1].

The combination of PET and MRI has been limited by the photodetectors' need to be reliable in magnetic fields. The rise of avalanche photodiodes (APDs) and SiPMs made this possible. The first APD-based PET ring appeared in 2006 (Siemens Healthcare Molecular Imaging) for brain imaging and 2010 for the whole body (Biograph mMR). PET/MRI is, next to superior soft image contrast, also powerful in other domains like low-radiation, motion correction (and more). However, it is very expensive, has a low patient throughput and at this point is still mainly used in research environments.

Semiconductor photodetectors which were initially designed for MR-compatibility also became the preferred photodetector in PET/CT due to its timing capability, compactness and general superior performance. In 2016 GE launched the Discovery MI PET/CTs based on SiPMs.

### 2.4.5 Clinical total-body PET

The existing PET scanners have an axial FOV of about 15-30 cm. The fraction of coincidences that is detected by this scanner geometry is around 1%. A major improvement of current PET scans can be achieved by increasing the axial length of the scanner (Figure 2.16) and therefore improving sensitivity and SNR [46]. While the concept of so called total body (TB)-PET is known for a long time it had not been realised due to the large amounts of hardware needed and the related cost that was expected to hinder the commercialisation. Recently the first funding allowed to construct such a system. The EXPLORER scanner [45, 47] extends to 195 cm resulting in an increased sensitivity factor of 40. Not only does the image quality improve significantly (6 times better SNR) but also the tracer distribution throughout the human body can be captured dynamically (Figure 2.17). In return for the improved image quality the scanning time can be reduced by a factor of 40 or the injected activity can be reduced by the same factor. This opens up a wide range of interesting potential applications and opportunities that are currently being explored. Similar approaches have been realised at UPenn with a slightly shorter length and more focus on TOF implementation. The reported timing resolution is 256 ps [48, 49]. The two systems employ pixelated detectors of 2.76 mm and 3.76 mm crystal width leading to system resolutions of 3.0 mm [50] and 4.0 mm respectively. The missing DOI capabilities result in off-centre resolution degradation to 4.7 mm and 5.6 mm FWHM.

Seen as the largest downside of TB-PET scanners is the cost factor. Efforts are made to find the best benefit-cost trade-off. At UGent a TB-PET is investigated that is reduced in length to around 1 m, covering head to hip of most adults. The use of monolithic detectors will allow uniform high resolution even at off-center positions due to their DOI capability [51, 52].

An alternative design, called J-PET, was developed at the Jagiellonian university in Krakow. The group constructed the first PET based on plastic scintillators. The scintillators are long strips that are axially arranged in layers. The interaction position of the gamma in the plastic strip can be determined by the time difference that is measured at both end of the strips. The strips are very cost-effective compared to organic scintillators and have a small light attenuation. Due to the strip readout at both ends the axial FOV can easily be extended to a TB-PET scanner without a significant increase of cost. In other words, the strip readout is independent of the aFOV [53–55]. The first version of the J-PET has an axial length of 50 cm [56]. However, to obtain similar stopping power in a PET system much thicker scintillators are needed. Furthermore, almost all interactions are Compton interaction making it more difficult to filter true coincidences.

The first commercial total-body PET scanner has been launched by United Imaging Healthcare the uExplorer [50] (Figure 2.18 a)) and is based on the design of the previously mentioned EXPLORER. Shortly after, the Biograph Vision Quadra was launched by Siemens [57] (Figure

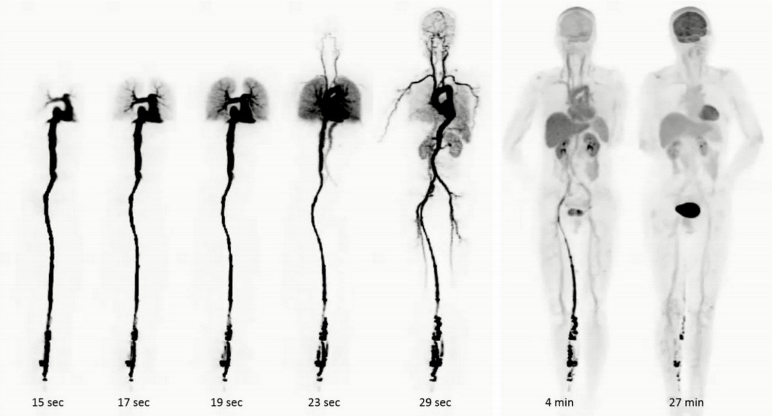

**Figure 2.17:** Dynamic scan of images acquired with the first total-body PET scanner EXPLORER. This is the first time (2019) the entire human body is imaged at the same time. This research was originally published in JNM. Badawi et al. First Human Imaging Studies With the Explorer Total-Body Pet Scanner. J Nucl Med. 2019;60:303. © SNMMI. [58].

2.18 c)). The Quadra has an axial FOV of 106 cm and was first installed in October 2020. The system length is achieved by placing four detector-block assemblies in series. The pixel width is 3.2 mm. The system also has TOF capability of <250 ps.

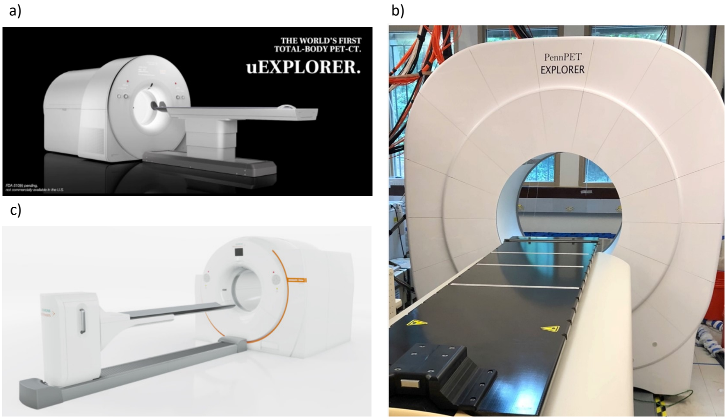

**Figure 2.18:** The first total-body PET scanners a) the United Imaging uEXPLORER b) the PennPET EXPLORER and c) the Siemens Biograph Vision Quadra.

## 2.5 Conclusion

In this chapter we focussed on PET as a functional imaging modality in the broader context of medical imaging. We provided an overview of PET imaging principles, its limits, the scientific background and the technological features. Finally we summarized the most important technical milestones in PET, from the initial positron imaging successes to the latest preclinical and clinical developments. In the next chapter we leave the system level and focus on one of the most important components of the system: the gamma ray detector.

# 3

# Gamma ray detectors for PET

## 3.1 Introduction

In this chapter the PET gamma ray detector will be introduced, starting with a brief overview of the most important milestones in PET detector development. This is followed by a section about the performance metrics used to evaluate a PET detector. The next section introduces the scintillator mechanism, the ideal scintillator properties for PET detectors and explains the importance of the crystal surface treatment. Next, the available photodetectors used to read out the scintillators are described. Then the principles, advantages and disadvantages of pixelated versus monolithic detectors are described and discussed. Since monolithic detectors require a calibration step to achieve high event positioning performance the calibration techniques as well as the event positioning algorithms are explained. The chapter closes with a section on Monte Carlo methods used to model monolithic scintillators to understand their behaviour, and predict and optimize their design.

## 3.2 Milestones in PET detector development

Scintillation gamma ray detectors consist of three main components: the scintillator, the photosensor and the electronics. The most important detector requirements are (i) having a high efficiency to detect 511 keV gamma rays and (ii) providing precise information on the interaction position of the gamma interaction(s) inside the crystal. Furthermore

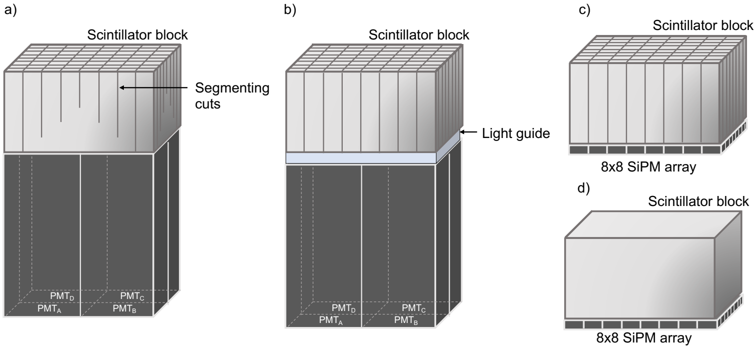

**Figure 3.1:** Different detector designs. a) One of the first block detector designs b) fully pixelated design with light guide c) fully pixelated design with one-to-one solid-state detector coupling (here SiPMs) d) monolithic detector design.

good timing and energy resolution as well as good countrate performance are desirable.

The classical PET detector, also known as block detector, first came up in the 1970s. At the time it was a 20-30 mm thick BGO scintillator coupled to photomultiplier tubes. To obtain better spatial resolution the crystal was segmented in sub-elements. A photodetector coupling for each of those elements would have increased the cost dramatically, instead, the large crystal was segmented by partial cuts in the material (Figure 3.1a)). The cuts were filled with a reflector to reduce crosstalk between the elements and modify the light spread in the crystal depending on the gamma interaction position. Only four PMTs were then needed to get a response that can be used to determine the crystal element where the interaction occurred. The output X,Y is the estimated position of the annihilation in the block detector with the four signals being $\text{PMT}_A$, $\text{PMT}_B$ and so on.

$$X = \frac{(PMT_A + PMT_B) - (PMT_C + PMT_D)}{PMT_A + PMT_B + PMT_C + PMT_D}$$

$$Y = \frac{(PMT_A + PMT_C) - (PMT_B + PMT_D)}{PMT_A + PMT_B + PMT_C + PMT_D} \tag{3.1}$$

Lutetium-based scintillators replaced the BGO scintillators in the late 1990s having a higher stopping power, higher light output and fast decay time. Especially the higher light output enabled the use of smaller and fully segmented scintillation pixels and thus improving spatial resolution. This array of pixels was coupled to a lightguide serving to distribute the light over multiple PMTs (Figure 3.1b)). Between the 2000s and 2010s solid state photodetectors became available (Avalanche photodiodes (APDs) and later silicon photomultipliers (SiPMs)). With these devices being about the size of the segmented crystal a one-to-one coupling was made possible improving the decoding error (Figure 3.1c)). To this day detectors with sub-elements down to 0.5 mm have been developed [59]. The presence of small pixelated photodetectors also brought rise to non-segmented monolithic detectors which can provide high spatial resolution and provide DOI information (Figure 3.1d)). In the next section we will define and discuss the performance metrics which are relevant for a PET detector.

## 3.3 Performance metrics

### 3.3.1 Detector sensitivity

Sensitivity or detector efficiency defines the ratio of how many of the emitted gamma rays are finally detected. According to Beer-Lambert Law this value depends in first instance on the thickness of the crystal, the effective atomic number Z and the density. Furthermore the packing fraction of the crystal and the applied energy window has an influence on the number of detected events.

$$S = \frac{\#photons_{detected}}{\#photons_{emitted}} \tag{3.2}$$

### 3.3.2 Spatial resolution

Detector intrinsic spatial resolution is the ability of the detector to resolve adjacent points from each other. The better the spatial resolution the sharper and more detailed the imaged object appears. Spatial resolution is expressed as the full width at half maximum (FWHM) of the detector response when irradiated with a infinitely small source (Figure 3.2). The intrinsic spatial resolution of a PET detector is only

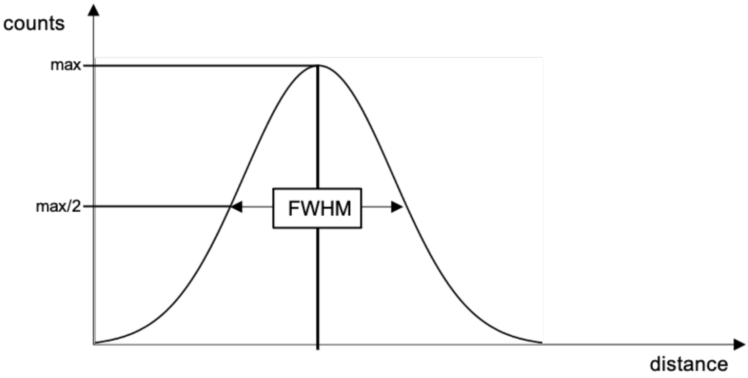

**Figure 3.2:** The FWHM metric.

one factor that influences the resolution obtained on system level. Next to the detector spatial resolution the positron range and system diameter (non-collinearity) define the system resolution (cfr. Section 2.3.3). The spatial resolution of a PET detector is dependent on many factors such as the scintillator light output, the SiPM pixel size and photon detection efficiency (PDE), and the scintillator thickness. In monolithic detectors the spatial resolution is also dependent on the algorithm used to estimate the gamma interaction positions from the measured light distribution. For pixelated scintillation detectors the spatial resolution is dependent on the width of the scintillator pixel elements (cfr. Section 3.6).

### 3.3.3 Energy resolution

Ideally the photopeak in the energy spectrum of a 511 keV emitter appears as a sharp peak or line. The peak becomes broadened in an actual spectrum by a whole range of effects. Even if the same energy was deposited in a scintillation detector there is a statistical variation of the number of generated scintillation photons per keV. The scintillation position inside the crystal also changes the number of scintillation photons that is detected. A scintillation close to a crystal boundary can cause a large number of photons to exit the crystal. The amount of light that exits the crystal depends mostly on the surface treatment and reflective coating. Furthermore statistical variations are introduced by the photodetector and by fluctuations in the power supply of the photodetectors. Due to these statistical effects the photopeak

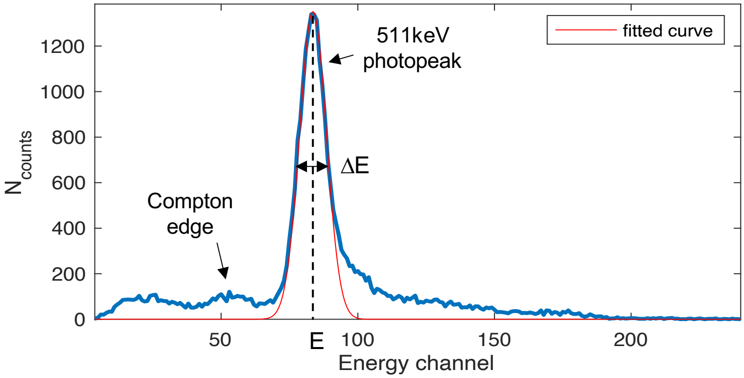

**Figure 3.3:** The energy spectrum (blue) of a gamma ray detector is acquired and fitted with a Gaussian (red). The peak position and width of the distribution define the energy resolution.

appears as a more Gaussian shaped curve instead of a line. The energy resolution is measured by calculating the FWHM of this energy peak. The energy resolution $E_{res}$ is given in percent as the FWHM of the peak ΔE divided by the energy peak position E.

$$E_{res} = \frac{\Delta E}{E} \times 100\% \tag{3.3}$$

A good energy resolution is desired to distinguish gamma rays with similar energies and exclude, for example, gammas that have interacted with e.g. the patient tissue and scattered. A gamma ray that scattered in the patients body changes its travel direction. Subsequently the detected gamma does not contain the needed information to construct a valid line-of-response. These events are then removed from the dataset.

### 3.3.4 Timing resolution

Timing resolution is the capability of the detector to accurately measure the time when the gamma photon arrived at the detector. In first instance the time window for accepting coincidences can be decreased with better timing resolution and they reduce the number of random coincidences. Approaching a much better timing resolution, the detector can measure the time-of-flight difference of the gammas. This allows to reduce the range of possible interaction positions along the LOR and therefore improve SNR. Ultimately the timing resolution could be good enough to predict the exact interaction position along the LOR and no reconstruction will be needed anymore.

## 3.4 Scintillators

### 3.4.1 The scintillation mechanism

The two main types of scintillators used for scintillation detectors are organic materials dissolved in a liquid and inorganic solid scintillation crystals. In PET mostly inorganic scintillators are used due to their higher effective atomic number $Z_{eff}$ which enables the material to stop the high-energy gamma photons. The light yield of inorganic scintillators is also more proportional to the deposited energy compared to inorganic scintillators [60].

The crystal structure is the reason why the scintillation occurs and determines the energy states in the scintillator. While some crystals exist in their pure state, most of them are doped with impurities of other atoms to modify the energy states and enable the scintillation effect. Two examples of impurity-activated scintillators are thallium doped - sodium iodide NaI(Tl) or caesium iodide CsI(Tl).

The existing energy states are the valence and conduction band (Figure 3.4). The energy difference between the two bands is called band gap. Through the photoelectric or Compton interaction in the scintillator an electron is moving from the valence band to the conduction band. The number of created electron-hole-pairs is proportional to the energy absorbed. The electron then de-excites and moves back to the valence band under the emission of its energy in the form of light photons. The spectrum of the emitted light is determined by the energy states of the bands and may be modified by impurities.

### 3.4.2 Properties of a scintillator

The properties of a small selection of typically used scintillator materials are displayed in Table 3.1. The relevance of each property for PET detectors is briefly discussed in this section.

Ideally a scintillator used for PET detectors should have a high stopping

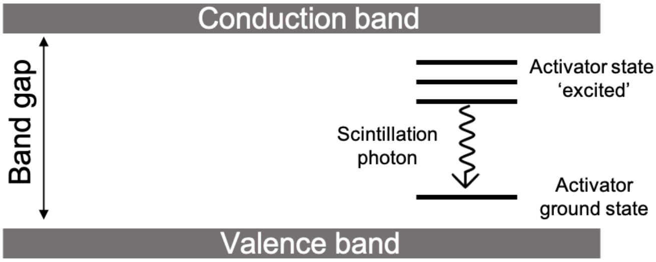

**Figure 3.4:** The scintillation mechanism is based on the crystal structure with its energy bands.

power which means that a large fraction of incident gamma photons are absorbed by the material. As previously mentioned, this is dependent on the density $\rho$ and effective atomic number $Z_{eff}$ and the thickness of the material x. Additionally, a large $Z_{eff}$ will increase the fraction of photoelectric interactions versus Compton scatter. This is desired because the gamma energy will be deposited at one single location and improve the positioning accuracy which in turn improves the determination of the line of response drawn between two opposing detectors.

**Table 3.1:** Scintillator materials used in PET and their properties [5]. LYSO(Ce) data from [61].

| Property | LYSO(Ce) | BGO | NaI(Tl) | $LaBr_3$(Ce) |
|---|---|---|---|---|
| Density (g/cm$^3$) $\rho$ | 7.20 | 7.13 | 3.67 | 5.3 |
| Effective atomic number $Z_{eff}$ | 66 | 73 | 50 | 46 |
| Decay time (ns) | 42 | 300 | 230 | 35 |
| Photon yield (per keV) | 29 | 8 | 38 | 61 |
| Index of refraction | 1.82 | 2.15 | 1.85 | 1.9 |
| Hygroscopic | no | no | yes | yes |
| Peak emission (nm) | 420 | 480 | 415 | 358 |
| Attenuation length for 511 keV (mm) | 11.5 | 10.4 | 29.1 | 21.3 |

Furthermore, a short decay time is desired, which is the time in which most of the scintillation photons are generated. It reduces pile-up effects, minimizes dead time and improves timing resolution.

The number of photons emitted per keV is called the light output or photon yield. A higher light yield results in more accurate estimation of the gamma interaction position and a better energy resolution. For TOF performance the number of photons emitted (ideally with a short scintillator rise time) and finally detected per photodetector pixel is important.

To optimize the extraction of the photons from the scintillator it should have an index of refraction close to that of the photodetector. Additionally the emission spectrum of the scintillator and the wavelength dependent quantum efficiency of the detector should match as good as possible. The peak emission wavelength of different scintillators is given in Table 3.1. Some crystals are hygroscopic meaning that they cannot be exposed to air but must be encapsulated in a air-free (rather moisture-free) environment. This makes the handling of those scintillators more complicated and not desirable.

The attenuation length (mm) describes how easy a 511 keV gamma ray can penetrate the material. The linear attenuation coefficient $\mu$ can be calculated as 1/attenuation length ($\mathrm{mm}^{-1}$).

### 3.4.3 Crystal surface treatment

The measured light distribution depends strongly on the surface treatment of the crystal. The crystal itself can be left ground as cut or mechanically polished or chemically etched. Then a coating can be applied such as black paint, Teflon wrap (or white paint), specular mirror-like reflectors or retro-reflectors.

Black paint is mostly used for monolithic crystals because it absorbs optical photons at the scintillator edges where many photons reflect before being detected. The reflections lead to a distortion of the detected light distribution potentially leading to an inaccurate position estimation. However, it may also have a negative effect on energy and timing resolution due to the smaller total number of collected optical photons. Teflon is a white material that can be wrapped around the crystal. It reflects photons with high probability and in a diffuse manner. The more layers of Teflon tape are used, the higher the reflectivity. Alternatively a white paint can be used leading to a similar reflection pattern. Enhanced specular reflector (ESR) is a reflecting material that has also a high reflectivity, but reflects optical photons in a specular pattern. Retro-reflectors are known from traffic signalling like street signs and reflect the photons in the same direction they came from leading to a preservation of the light distribution. The micro-structure of a retro-reflector is designed in a way that each photon reflects three times inside a cube shaped structure before the photons travel path is reversed.

## 3.5 Photodetectors

To sample the light distribution generated by a scintillation pulse inside a monolithic crystal, photodetectors are attached to typically the backside of the crystal. Different approaches have been investigated such as front-side readout, front- plus back-side readout and only edge-readout but not investigated in this work.
Photon sensors should have a response proportional to the number of incident photons and the gain should be sufficiently large so that the signals can be easily interpreted. The response times of the detectors should be smaller than nanoseconds and they should be sensitive for a broad range of electromagnetic wavelengths. The internal dark count rate and noise should be as small as possible.

### 3.5.1 Photomultiplier tubes

PMTs were the main photodetectors in PET until a few years ago being reliable and low noise photosensors. However, there are some drawbacks. The quantum efficiency is limited by the photocathode to around 25% at 420 nm. A high gain is reached only by applying a bias voltage of 1-2 kV which makes the power supply costly. Furthermore PMTs are very large in size and are not suitable for the use in an MRI since they are not working reliably in a magnetic field.

### 3.5.2 Semiconductor detectors: APDs and SiPMs

Semiconductor detectors are solid-state detectors that are compatible with MR while providing high gain, improved timing and are much more compact than PMTs. They work with low operating voltages and the available pixel sizes are 2-6 mm, which is ideal for the use in PET detectors. Initially APDs were used specifically for PET/MRI systems [62, 63]. They have an outstanding high quantum efficiency of more than 65%, but excess noise (or gain noise) is next to temperature sensitivity one major drawback and negatively affects timing resolution [64]. APDs

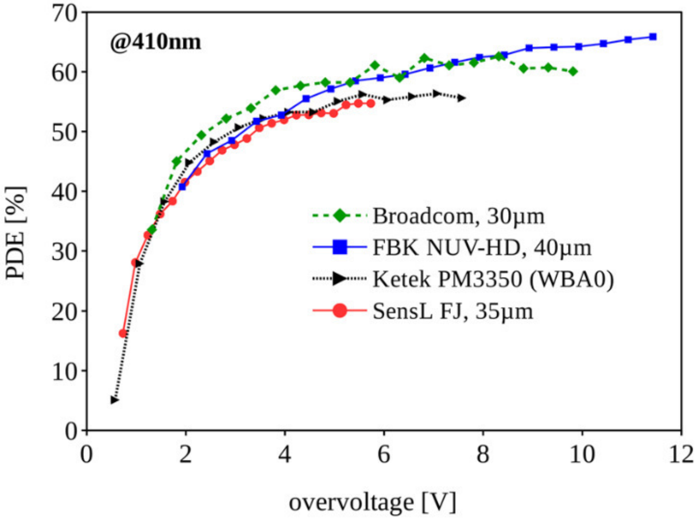

**Figure 3.5:** PDE in function of the applied overvoltage at 410 nm. Compared are SiPMs from different vendors: Broadcom, FBK, Ketek and SensL (now: ON-semiconductor) [10].

are therefore not suitable for TOF-PET.

Later SiPMs replaced APDs [65] and are now the most commonly used photodetectors in newer PET systems. SiPMs consist of hundreds to thousands of microcells or single photon avalanche photodiodes (SPADs) per mm$^2$ which are Geiger-APDs combined with individual quenching circuits. The SiPM gain is around 1x10$^6$ and can be achieved with only ~30 V bias voltage [66].

As seen in Figure 3.5, SiPMs can have PDEs up to 60%. The PDE wavelength dependency can be seen in Figure 3.6. Note that the peak emission of LYSO is at this wavelength (Table 3.1) and therefore a perfect match to be combined with SiPMs. The noise is very low and the uniformity between SPADs is high. This enables the SiPMs to detect photo-electron spectra with high precision. This is not possible with PMTs due to high variances in gain and noise.

PDE is the probability of a photon being detected by the SiPM and is dependent on the photon wavelength $\lambda$, the over-voltage $V$ and the fill factor $F$. $\eta(\lambda)$ is the quantum efficiency of silicon and $\varepsilon(V)$ the

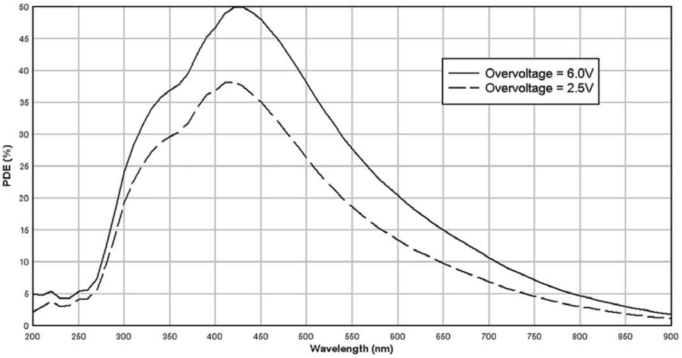

**Figure 3.6:** The SiPM PDE in relation to the photon wavelengths [67]. These SiPMs are most sensitive for light with a wavelength of ~430 nm.

probability of an avalanche to be initiated (Equation 3.4).

$$PDE(\lambda, V) = \eta(\lambda) \cdot \varepsilon(V) \cdot F \tag{3.4}$$

The fill factor $F$ is the active area of an SiPM that is sensitive to light. Higher fill factors, meaning larger SPADs, lead to higher PDE and gain but also increase recovery times. For better recovery times smaller SPADs can be useful. Dark counts are the major source of noise in SiPMs and originate from thermal electrons [64, 67].

## 3.6 Detector designs

### 3.6.1 Pixelated scintillators

All clinical and most preclinical PET scanners consist of detectors with pixelated scintillator arrays. These arrays consist of many individual thin crystal elements with a length of 15-25 mm for clinical PET (shorter for preclinical). The more the width of the crystals is reduced the better the resolution that can be achieved. For clinical settings this is a width of 2.6-5 mm while in preclinical scanners the width can go down to 0.5 mm. The scintillation material is grown as an ingot, a large block, and is then mechanically cut into crystal pixels (Figure 3.7). The crystal pixel surface is further treated to influence the reflection properties and light output (cfr. Section 3.4.3).

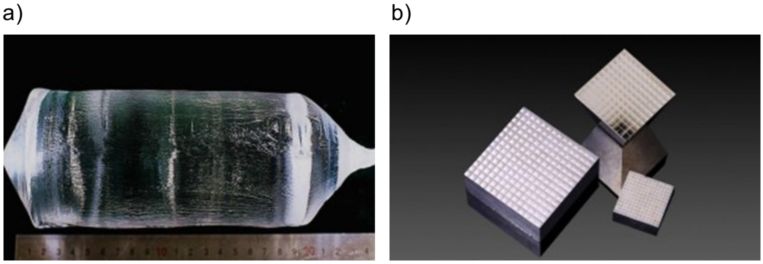

**Figure 3.7:** a) A LYSO ingot with maximum dimensions of ø 95 mm × 200 mm and b) manufactured pixelated LYSO arrays with different pixel sizes [61].

### Pixel decoding

In a one-to-one pixel-photodetector coupling the 2D gamma interaction position can simply be assigned to one of the discrete crystal pixels. In case that *number of scintillator pixels* < *number of photodetector pixels* a light guide can be used to spread the light over multiple photodetectors. This reduces the number of photodetectors but negatively affects the spatial resolution since mathematical algorithms are necessary that introduce a pixel decoding error.

### Sensitivity

In between the pixels a reflector is placed that is needed to minimize crosstalk and improve light output. The reflector material reduces the detector packing fraction and thus deadspace is created. The smaller the pixels the more deadspace is created. The sensitivity drops significantly as displayed in Table 3.2. For example, in an array of 1 mm pixels the sensitivity loss is at 14% compared to a monolithic crystal that has no deadspaces. Since PET detectors work in coincidence the impact is quadratic which results in a total loss of 26%. The sensitivity loss can be compensated by using longer crystals. The stopping power would be better but in consequence the collection efficiency of scintillation photons in very long crystals is compromised.

### Light collection efficiency

In crystals with a large aspect ratio the photons reflect many times before they reach the photodetector. According to a simulation of a 3 x

**Table 3.2:** Sensitivity loss for pixelated arrays of different pixel sizes with 3M Vikuit ESR reflectors compared to a monolithic detector design.

| Pixel array | Pixel size [mm] | Sensitive area $A_S$ [$mm^2$] | Detector size A [$mm^2$] | $A_S/A$ | Sensitivity Loss |
|---|---|---|---|---|---|
| 86 x 86 | 0.5 | 1849 | 2452.7 | 0.75 | 25% |
| 46 x 46 | 1 | 2116 | 2452.7 | 0.86 | 14% |
| 24 x 24 | 2 | 2304 | 2482.5 | 0.93 | 7% |
| 16 x 16 | 3 | 2304 | 2428.0 | 0.95 | 5% |
| monolithic | - | 2500 | 2500 | 1 | 0% |

3 x 20 $mm^3$ crystal a photon reflects on average 50 times in a polished crystal [68]. An increasing number of reflections increases on the one hand the chance that the photon is lost and on the other hand the time until it is detected. This effect is amplified with increasing crystal aspect ratio. The light collection efficiency drops.

### DOI

The number of scintillation photons that reach the photodetector is strongly dependent on the DOI of the gamma interaction and on the surface finish. In a polished crystal the DOI effect is much less pronounced than in a crystal with a rough surface structure. The light output variance per depth and in between crystal pixels makes it challenging to extract DOI information and usually requires additional hardware and electronics.

### Timing

Pixelated detectors have shown to provide excellent timing resolution [69]. Current state-of-the-art CTR is 214 ps FWHM based on pixelated arrays of 3.2 x 3.2 x 20 $mm^3$ [15]. However, the need for longer and thinner crystals leads inevitably to a larger variance on the photon transit times resulting in a deterioration of timing performance [8].

### Cost

The trend towards smaller scintillation crystals to obtain better spatial resolution increases the cost of the detectors [70]. In a small market study including two vendors in 2019 [71] we found that pixelated arrays are more economical for larger pixel sizes with a price cross-over at 2 mm pixel size (unit prices for arrays with dimensions 50 x 50 x 16 $\text{mm}^3$). The smallest available pixel size was stated to be 0.5 mm, which makes the prices more than triple compared to the monolithic block. In this case, the pixelated detector design trades one performance parameter at the cost of another. An improved spatial resolution is only achieved by a loss of potentially all other performance metrics: sensitivity, energy resolution, timing resolution and manufacturing feasibility.

## 3.6.2 Monolithic scintillators

### Light distribution

Monolithic PET detectors consist of one slab of scintillation material without any segmentation or gaps. The scintillation light spreads throughout the crystal and is typically measured at one crystal side by a matrix of photodetectors. The measured signal therefore represents the light distribution inside the crystal. This light distribution can be used to determine the 2D position of the gamma interaction by the peak position of that distribution. Not only the 2D position but also the DOI can be estimated from that distribution. Looking at the spread of the light over the photodetector array one can estimate how *deep* in the crystal the photon interaction occurred. If it occurred closer to the photodetectors a concentration of most of the photons on a few photodetector pixels can be observed. If it occurred further away from that array the light will spread over many pixels (Figure 3.8).

### Challenges

There are several factors that make the monolithic detector concept a bit more complicated. First of all, there are many scintillation photons that are reflected by the detector sides and top which influences the measured distribution significantly. Especially towards the edges, the peak of the measured distribution might not correlate to the interaction position.

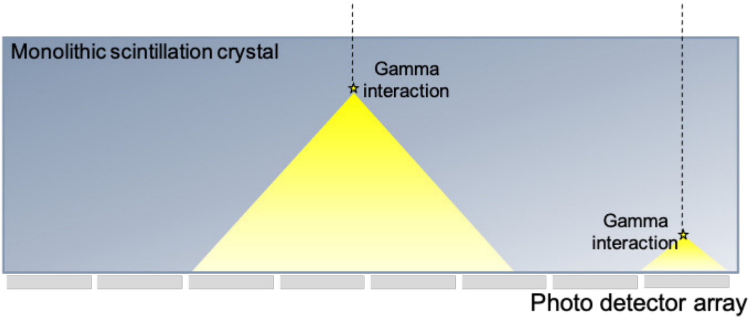

**Figure 3.8:** Simplified concept of light spread inside a monolithic crystal. A gamma interaction towards the top spreads light on multiple photodetector pixels. An interaction close to the array only triggers very few pixels.

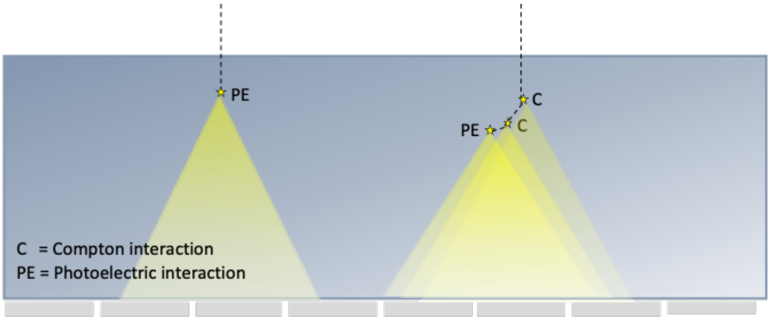

**Figure 3.9:** The gamma energy deposition and resulting light distribution for a pure photoelectric event and an event with two preceding Compton interactions.

Furthermore, there is often more than one interaction position inside the crystal, mostly due to Compton scatter, which makes it more complex to determine the position(s) of interaction since the light distributions will overlap (Figure 3.9) (cfr. Section 6.3). Additionally, statistical noise, variations in scintillator light yield and amplifier gains of the photodetectors contribute to the signal. It is also possible that multiple events are triggered at once either two gamma events or one gamma event and a $^{176}$Lu event. The higher the count rates the higher the probability that this will occur. However, in a non-saturated system the chances are rather small.

### Timing resolution

For monoliths the light spread and collection over multiple photodetector pixels results in low SNR and thus limits the achievable timing performance [72, 73]. However, the unrestricted movement of scintillation photons with a direct travel path to the photodetector makes monolithic crystals fundamentally superior to be used for timing measurements. The monolith is therefore a promising alternative to reach timing performances comparable or better than those of pixelated detectors using precise calibration techniques.

### Readout channels

One should also keep in mind that if all photodetector channels are read out, the count rate performance of the electronics needs to be much higher for monolithic detectors compared to pixelated ones. Various techniques to reduce the number of readout channels have been evaluated e.g., Anger logic, row and column summing or a sparse readout [74–77]. However, these techniques should be implemented cautiously since performance parameters like spatial resolution can degrade but especially timing resolution is sensitive to multiplexing [72, 78].

### Spatial resolution

Multiple monolithic detector designs have been evaluated with respect to spatial resolution. The performance depends highly on the crystal thickness. For the use in clinical systems a thickness of more than 12 mm is typically required to have sufficient detector sensitivity. A spatial resolution of 1.7 and 1.5 mm FWHM could be achieved with a 22 and 20 mm thick crystal, respectively [73, 79]. A 15 mm thick crystal was used in [74] achieving 1.8 mm FWHM. In [80] a spatial resolution of 1.4 mm (with correction of source size) could be obtained with a crystal thickness of 12 mm. Even better spatial resolution of 1.1 mm [79] and 0.78 mm [81] could be achieved with a 10 and 8 mm thick crystal. In [82] a remarkable detector spatial resolution of 0.9 mm FWHM is reported with a crystal of 15 mm thickness. A great effort is done to isolate the source size from the measured FWHM values leading to a better estimate of the intrinsic spatial resolution.

Not only the crystal thickness but also the evaluated region on the detector (centre, edge, corner, centre line on one axis) and the correction methods applied to isolate the calibration beam diameter [82] have a large impact on the stated spatial resolution. There is no standardized procedure to evaluate the performance of monolithic detectors and therefore it is not trivial to compare results from different groups.

## 3.7 Event positioning algorithms

The gamma interaction position inside the monolithic crystal induces a shower of scintillation photons that is detected by the photodetectors coupled usually to one side of the crystal. The measured light spread is then used to estimate the interaction position in 2D (x,y) or 3D (x,y,z (DOI)). Simple position estimation of the gamma interaction with Anger logic or functions that model the light distribution work well in the center of the detector. However, the reflections of the scintillation light at the edges of the crystal are distorting the light distribution causing positioning artefacts. The events at the crystal edges are compressed and positioned more towards the center than they should be. Efforts have been made to reduce this effect by using black absorbing paint to retain the light distribution at the cost of potentially losing a large fraction of photons. Further, more complex statistical approaches have been used such as nearest neighbour, maximum likelihood estimation (MLE) and more recently also neural networks to obtain the best spatial resolution in monoliths. Most statistical methods do require a calibration upfront, collecting reference light distributions at known irradiation positions.

A collimated source, for example by a tungsten collimator to a 1 mm diameter beam or even narrower is produced by a radioisotope e.g. $^{68}$Ge or $^{22}$Na (Figure 3.10). This beam is then irradiating the detector step-by-step along a fine 2D grid (e.g. 1 mm steps). At each position 100 to 1000 events are acquired and stored as reference data. The events energy which is the sum of all detected photons across the photodetector array is calculated. Events above and below certain energy thresholds are eliminated from the data set. This step filters out events that are not photoelectric or have not deposited their full energy inside the crystal e.g. scattered events.

Alternatively the physical collimation of the calibration source is achieved by a slit collimator (tungsten or lead) or a coincident detector forming a narrow calibration beam. Calibration leads to very good spatial resolu-

tion at the cost of work-intensive procedures. Often each individual detector block is calibrated separately. This is possibly the largest factor holding back the adoption of monolithic crystals in clinical PET systems. However, techniques to speed up the calibration are addressed by multiple research groups [73, 79, 80, 83–86] and are not seen as a key limitation of using the monolithic detector design in future PET systems [8]. Only recently the more complex positioning has become possible in real time due to more advanced hardware like GPUs.
Here we discuss in detail Anger logic, MLE, MNN positioning, artificial neural networkss (ANNs) and gradient tree boosting (GTB).

### 3.7.1 Anger logic

Anger logic, also known as center of gravity (COG), was developed by Hal Anger in 1958 [87]. It can be used without any sort of calibration and serves detectors that do not need to achieve high spatial resolution. Examples are certain clinical SPECT applications. In SPECT sensitivity is a trade-off for spatial resolution due to the use of its collimators. When sufficient sensitivity is required only low spatial resolution can be obtained and Anger logic performance may be sufficient [88]. Anger logic is also used for pre-processing calibration data of monolithic detectors e.g. when a spatial filter is applied to remove non-relevant events outside the region of interest (ROI) i.e. the calibration beam position.
The interaction position $\mathrm{X}_i$,$\mathrm{Y}_i$ is calculated with the weights $wX$ and $wY$ that correspond to the position of the photodetectors with respect to the detector center. The energy $E$ is the sum of the charge $C$ in all photodetector channels $E = \sum_{k=1}^{K} C_k$. The number of photodetectors is $K$.

$$X_i = \frac{\sum_{k=1}^{K}(wX_k \cdot C_k)}{\sum_{k=1}^{K} C_k} \tag{3.5}$$

$$Y_i = \frac{\sum_{k=1}^{K}(wY_k \cdot C_k)}{\sum_{k=1}^{K} C_k} \tag{3.6}$$

A variation of Anger logic is the raised to the power (RTP)-algorithm [89] to improve positioning at the edges. The energy $E$ is then exponentiated, with $p$ being the power. The interaction position X$_i$,Y$_i$ are:

$$X_i = \frac{\sum_{k=1}^{K}(wX_k \cdot {C_k}^p)}{\sum_{k=1}^{K} {C_k}^p} \tag{3.7}$$

$$Y_i = \frac{\sum_{k=1}^{K}(wY_k \cdot {C_k}^p))}{\sum_{k=1}^{K} {C_k}^p} \tag{3.8}$$

### 3.7.2 Maximum likelihood estimation

MLE [70, 90–93] is a statistical method requiring an extensive reference dataset as mentioned above. Furthermore the events are normalised by their energy values:

$$C_{norm_k} = \frac{C_k}{\sum_{k=1}^{K} C_k} \tag{3.9}$$

For each photodetector pixel i and each calibration position j the mean of the signal $\mu_{i,j}$ and the signal standard deviation $\sigma_{i,j}$ are calculated and stored in a look up table (LUT). Interpolation of the data allows a positioning on a grid finer than what was recorded initially.

For each position $j$ in the LUT the likelihood $P_{i,j,k}$ is calculated of an event $i$ with photodetector channel values $k$ occurring at this calibration position.

$$P_{i,j,k} = \prod_k \left(\frac{1}{\sigma_{j,k}\sqrt{2\pi}} exp(-\frac{C_{norm_{i,k}} - \mu_{j,k}}{2\sigma_{j,k}^2})\right) \tag{3.10}$$

The event i is assigned to the calibration position j where the value $\prod_k(P_{i,j,k})$ maximizes. The general approach is to calculate the likelihood exhaustively for every position. A reduction of calculation steps can be achieved by so called contracting-grid search [94], finding the likelihood on a coarser calibration grid and then a finer search around the coarse estimation position.

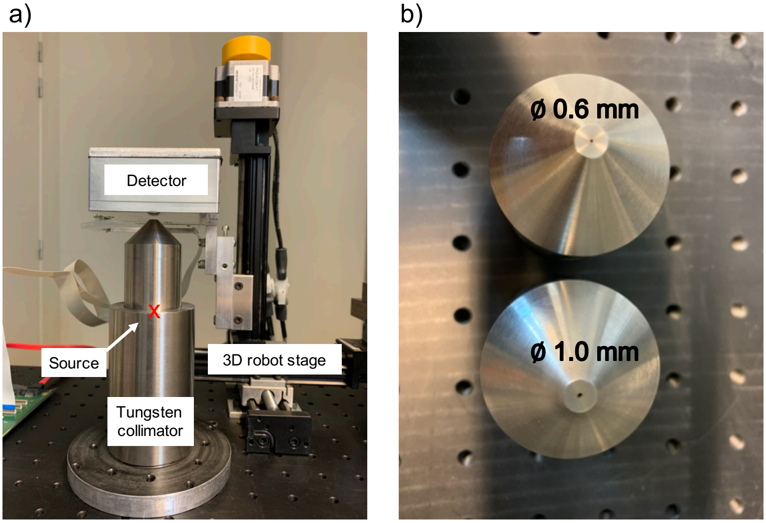

**Figure 3.10:** a) Calibration set-up with tungsten collimator and the detector mounted on a 3D-robot stage. b) Collimator with two collimation beam diameters.

### 3.7.3 (Mean) nearest neighbour

To determine the 2D interaction position of a scintillation event, with a nearest neighbour algorithm a large calibration data set is acquired with a pencil beam source at a small pitched grid on the crystal surface. For each position in the calibration data set the normalised signal is calculated and stored in a calibration map. A test signal is then classified to the nearest neighbour within the calibration map with the signal that has the least square difference. In other words, the nearest neighbour algorithm [95, 96] calculates the Euclidean distance between the light spread of the unclassified event to the light spread of each event in a reference data set. The reference data set includes the normalised charge $C_{ref_{j,k}}$ of each event in every calibration position $j$ and photodetector channel $k$. The event i that needs to be classified is normalised and called $C_{norm_{i,k}}$. The reference event with the least Euclidean distance to the unclassified event is considered the true interaction position.

$$Dist_{i,j} = \sqrt{\sum_{k=1}^{K} (C_{norm_{i,k}} - C_{ref_{j,k}})^2} \tag{3.11}$$

This method requires a relatively high number of calculations while only the discrete calculation positions can be classified achieving only limited spatial resolution. A variation of the nearest neighbour algorithm is the MNN - algorithm. Here the mean normalised charge per calibration position and photodetector channel is calculated. This reduces the number of calculation steps drastically. Instead of calculating the Euclidean distance of hundreds of events per calibration position there is only one event and one Euclidean distance per calibration position. Furthermore, MNN allows interpolation of the data to position events on a grid finer than what was recorded initially. While being efficient in the number of calculation steps the spatial resolution suffers under the 'mean'-signal approach.
A major improvement is achieved by first sorting the calibration data set into several groups of signals that have a similar light distribution and then calculating the mean of each of these groups [97]. The sorting can be done by calculating the variance of each event per calibration position and then building a number of groups per standard deviation range. The calculation steps increase with the number of standard deviation groups selected and degree of interpolation. DOI capability is also introduced by these standard deviation groups. This method is applied in the scope of this thesis and a more detailed description can be found in Section 4.2.2.

### 3.7.4 Artificial neural networks

ANNs [98–102] are very applicable to solve the inverse problem of linking light distributions to the gamma interaction position in the crystal especially with respect to the non-linear behaviour at the crystal edges. The photodetector signal is the input for the ANN training with the calibration beam position being the classification or regression output. The network architecture is a feed-forward multilayer network with the input nodes equal to the photodetector channels and followed by layers of fully connected hidden layers. This method is also applied in the scope of this thesis and a more detailed description can be found in Section 5.2.4.

### 3.7.5 Gradient tree boosting

GTB is a supervised machine learning technique [80, 103] based on sequential binary decisions called decision trees. The first tree is based on the input calibration position while the following trees are trained on the positioning error of the previous tree. Every new tree corrects therefore the result of the tree before. The final output is the sum of all previous predictions. The algorithm is very scalable to the memory restrictions and easily implementable on an FPGA.

## 3.8 Modeling of gamma ray detectors

Monte Carlo simulations are used in the field of nuclear medicine to help with scanner design decisions, the optimization of acquisition parameters and the design of reconstruction algorithms [104]. System simulations typically do not include the full detector modelling but rather use analytical models that calculate the detector response based on user defined input parameters such as detector energy resolution, dead time, quantum efficiency and so on. Detector simulations, also called optical simulations, focus solely on modeling single detector modules. Here each high energy photon generates optical photons in the scintillator and each scintillation photon is tracked until it is detected by the sensitive volume. The sensitive volume or photodetector can also be modeled with a certain packing fraction, PDE, noise etc. The photon trajectory can be stored and each photon interaction can be tracked individually. This is computing and memory expensive and therefore not (yet) feasible to simulate for whole systems with 10s, 100s or 1000s of individual detectors.

Here we will shortly introduce the simulation software Gate, one of its simulation frameworks: the optical system, and finally the available implementations to model surface reflectance.

### 3.8.1 Gate collaboration

GATE is an open-source Monte Carlo simulation toolkit which is developed and maintained by users in the medical physics community [104–107]. The underlying physics like tracking particles and processing interactions are relying on the Geant4 toolkit. In 15 years of development the applications of the simulation software is broad, ranging from nuclear imaging to radiotherapy, dosimetry and hadron therapy. GATE basically facilitates the simulation of imaging systems like PET and SPECT and provides tools for numerous simulation conditions (actors, kinetics, phantoms, readout etc.).

### 3.8.2 Optical system

To record interactions inside a simulated detector one needs to define an *optical system.* All interactions occurring inside the system and in a declared *sensitive detector* are recorded as *hits* to the simulation output. The optical system has two levels which are the *crystal* and *pixel* (crystal read out). The crystal geometry and material (density) are defined directly in the macro file. The material properties related to the scintillation material are defined separately in the *Materials.xml* file. The user can define the scintillation yield, index of refraction, rise time, absorption length etc. The generated optical photons are collected at the sensitive detector which is simply a geometric body attached to the crystal geometry. The photodetector array fill factor can be realized by modeling a single pixel and using the *repeaters* command with respective repeat vectors that leave a small gap in between each pixel. The PDE is defined as *EFFICIENCY* in *Surface.xml* corresponding to the surface definitions. The surface definitions are further described in the next section.

The source type definition provides many options. Simple particles, specific isotopes or a back-to-back source for coincidence measurements can be defined. The source settings define for a big part the computational power and time necessary to complete the simulation. On the one hand the user wants the simulations to be as realistic as possible, on the other hand the simulations should only be as complex as necessary. For example, in our detector calibration set-up the source is encapsulated in a tungsten collimator (Figure 3.11). The collimator geometry STL-file can be loaded into the software and the source can be placed inside. However, if one only desires a collimated source, then the more efficient implementation is a gamma point source definition with a small opening angle, mono-energetic and with a certain activity. This saves unnecessary computational steps of a huge fraction of gamma photons that would be absorbed inside the shielding material of the collimator.

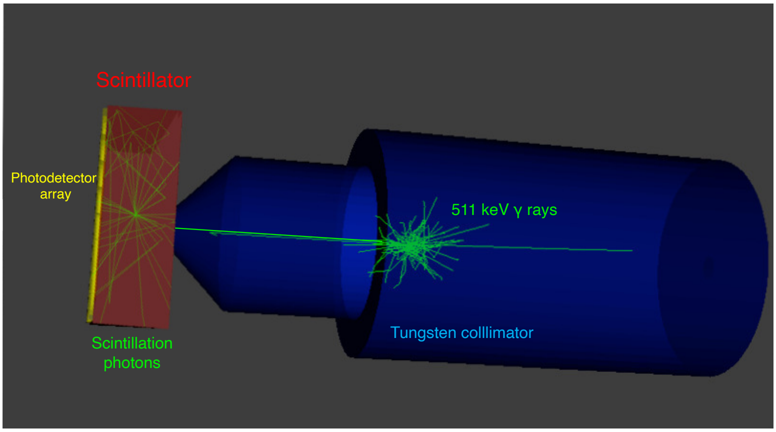

**Figure 3.11:** Optical simulation set-up in Gate. A calibration beam is formed by a tungsten collimator with a monoenergetic 511 keV gamma source. The collimator is simulated by importing the 3D STL file into Gate. The detector is a monolithic LYSO crystal with a pixelated photodetector readout. The crystal surfaces are defined with the LUT Davis surface reflectance model.

### 3.8.3 Surface reflectance model

In optical simulation that track each single photon, often including multiple reflections at geometry boundaries, it is crucial to precisely define the optical surfaces to generate a realistic light distribution [104]. Often used models for surface reflectance, e.g. the UNIFIED model in GATE [109, 110], suffer from inaccuracies, especially for rough surface data [108, 111, 112]. The reflection surfaces are often modelled as a set of micro-facets with orientations of a standard deviation $\sigma$ defined

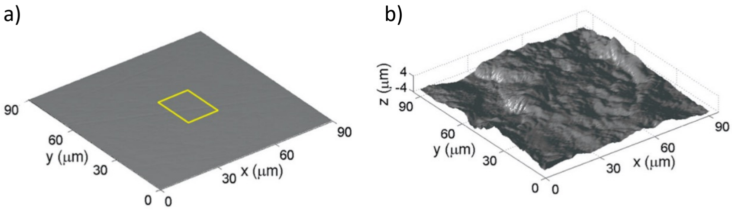

**Figure 3.12:** a) Surface topology of polished scintillator surface measured with atomic force microscopy (AFM). b) Rough surface topology. This figure was originally published in [108] © Institute of Physics and Engineering in Medicine. Reproduced by permission of IOP Publishing. All rights reserved.

**Table 3.3:** Simulation conditions overview.
Ra= average roughness, Rms $\sigma$ = root mean squared roughness, Rpv = peak-to-valley roughness. Data from [68].

| | Rough surface | Polished surface |
|---|---|---|
| Ra | 0.48 µm | 20.8 nm |
| Rms $\sigma$ | 0.57 µm | 26.2 nm |
| Rpv | 3.12 µm | 34.7 nm |

by the user. A more realistic model, the LUT Davis model, is based on measured surface data obtained from AFM measurements. The user simply defines the desired surface and reflector material and the simulation will extract the needed information from the LUT provided by the simulation software. In the following paragraph we will briefly explain the methods used to calculate the LUTs.

The topographic measurements of polished and rough surfaces (Figure 3.12) are then loaded in a custom simulation [108]. The roughness metrics can be seen in Table 3.3. The surfaces are irradiated with photons from all angular directions. The resulting angular distribution of the reflected rays (Figure 3.13) is stored in LUTs as well as the surface reflectivity. This work was extended to an integrated model of the scintillator and the reflector [68]. The available reflector options are Teflon and ESR (either air or grease coupled). Compared to other existing models the LUT Davis model considers the reflection probabilities and directions with respect to the incidence photons. To allow for more flexibility and user-specific surface modelling a tool was developed to generate custom LUTs [113]. This allows the user to define the surface roughness, scintillator properties, coupling medium and reflector type. The LUT Davis model is officially implemented in Gate since version 8.0 [114].

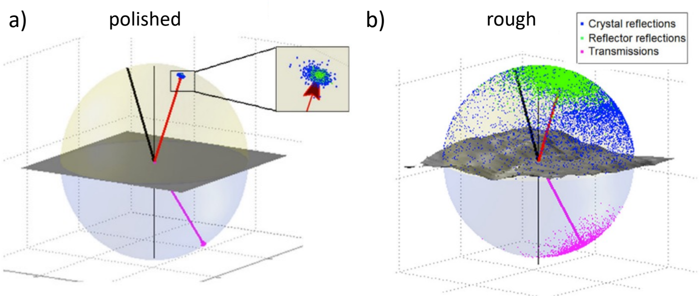

**Figure 3.13:** Photons at 20° incidence angle (black line) on a a) polished and b) rough surface. The blue dots represent the reflection distribution of the crystal surface, the green dots are reflected by the attached reflector (here, ESR, air coupled), the pink dots are photons transmitted through the reflector. This figure was originally published in [68] © Institute of Physics and Engineering in Medicine. Reproduced by permission of IOP Publishing. All rights reserved.

## 3.9 Conclusion

In this chapter we gave a detailed overview on gamma ray detectors for PET. The reader is provided with the necessary background to understand the research motivation and applied methodologies. We explained the most important developments in the field since the upcoming of the first block detectors and how monolithic detectors became more interesting in the recent past. Furthermore we elaborate on each individual detector component. The advantages and disadvantages of monolithic detectors versus the standard pixelated design play a central role for the research motivation of this thesis. To get familiar with the methods that we will use throughout the thesis we covered the calibration procedure and the range of existing event positioning algorithms. We finalize this chapter with the simulation software tools used to model the detector. In the next chapter our monolithic detector design is evaluated in an optical simulation study.

# 4

# Optical simulation study on the detector spatial resolution

## 4.1 Introduction

In the previous chapters we introduced PET and more specifically PET detectors. We discussed the potential of monolithic PET detectors for the use in clinical applications and their advantages compared to the commonly used pixelated design. In summary, we found that the trend towards smaller scintillation crystal pixels to obtain better spatial resolution negatively affects other desirable parameters like sensitivity, energy and timing resolution, and also cost. For this reason it is likely that future generation PET detectors could be based on continuous monolithic scintillation detectors. Other key features of continuous crystals are the intrinsically available DOI information that can be directly obtained from the measured light distribution. It also needs to be said that, the better the intrinsic detector resolution the more important the DOI performance gets. DOI improves the positioning accuracy at oblique incidence angles and improves resolution at off-center positions.

In this chapter optical simulations are used to investigate the detector performance of our monolithic detector design under idealised and controlled circumstances. We study several hardware-related parameters that are difficult to study or cannot be studied in depth in experimental set-ups due to cost, feasibility or because they cannot be controlled. These parameters are the photodetector pixel size, the PDE and the number of channels used to read out the sensor array. Pixel size and PDE are mainly limited to what is currently on the market: 2, 3, 4 or 6 mm pixels and 35-60% PDE. The number of electronic readout channels can be equal to the number of pixels (here referred to as individual channel readout) or a combined readout where signals from multiple channels are summed to reduce the cost in electronics (referred to as combined readout).

Optical simulations including an advanced surface reflection model allow us to investigate the effect of the mentioned parameters individually and understand their influence on the spatial resolution of the detector. Additionally, simulations allow us to access the ground truth interaction positions of Compton scattered events and generate perfect calibration sources and high statistics. Simulations can be very powerful albeit at the cost of ignoring effects that cannot be modelled accurately (noise, electronics).

The influence of the SiPMs PDE is partially covered in this chapter. The detailed analysis and discussion can be found in Section 6.4 of the Chapter 'Main degrading factors on spatial resolution'.

The simulation work resulted in two peer reviewed A1 journal publication [71, 100] and four conference contributions [115–118].

## 4.2 Materials and methods

To obtain a better overview of this section a brief summary is provided upfront. A monolithic 50 x 50 x 16 mm$^3$ LYSO scintillation crystal with back-side SiPM readout (Figure 4.1) is simulated. The thickness of 16 mm is typical to reach the needed sensitivity for clinical PET. The width and length are chosen with respect to the attached SiPM array. Arrays of 3.035 x 3.035 mm$^2$ and 6.07 x 6.07 mm$^2$ SiPM pixels are tested with three different PDEs. Further, individual channel versus combined channel readout, with summed rows and columns, are investigated. The detector is calibrated with a 511 keV source in 1 mm steps. Per position the calibration data is organized in six depth-layers. Events are then positioned with a MNN algorithm. The 2D spatial resolution is determined in terms of FWHM in the central region of the detector and dependent on the depth-layer. The resolution degradation at the edges and corners of the crystal are evaluated. The DOI positioning performance is evaluated. Finally, the resolution is determined in a

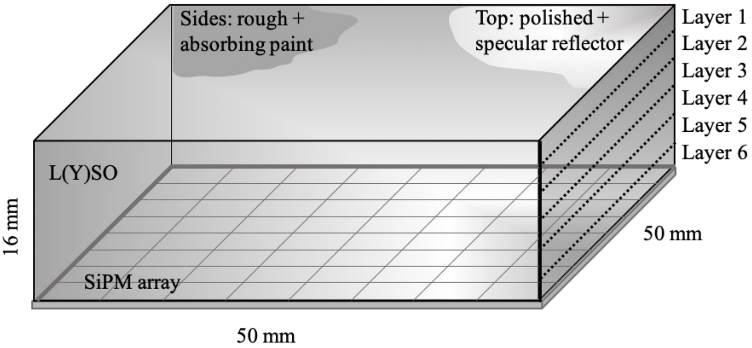

**Figure 4.1:** Optical simulation model of the monolithic PET detector with back-side SiPM readout in GATE. Indicated are the surface finish at the top and the sides of the crystal, and the virtual DOI layers.

Derenzo-like simulation set-up. Detector uniformity is assessed with a flood source.

### 4.2.1 Optical simulation set-up

#### Monte Carlo simulation with Gate

Optical simulations are performed with GATE v8.0. The monolithic crystal is defined as LYSO with dimensions 50 x 50 x 16 mm$^3$. No intrinsic radioactivity of lutetium is modelled. The scintillation yield is 29,000 photons/MeV. The index of refraction is 1.82 [61]. The absorption length for optical photons is set to 1 m. Compton scatter and the photoelectric effect are enabled in the GATE physics list. For simulation studies that aim at improving spatial resolution it is elementary to include an accurate surface reflection model. In our study we use the LUT Davis model (cfr. Section 3.8.3), the lateral sides are modelled as rough surfaces painted with black paint. Depending on the incidence angle of the photons on this surface they are either reflected or transmitted according to a measured reflectance. The black paint is modelled as 100% absorbing, which means all transmitted photons are absorbed. The top of the crystal is polished and covered with a specular reflector (3M ESR Vikuiti™) coupled with optical grease. Typical parameters to characterize the surface roughness are extracted from AFM data measured in [68] and were previously presented in

**Table 4.1:** Simulation conditions overview.

| | 3 mm SiPMs | 6 mm SiPMs |
|---|---|---|
| Actual pixel size | 3.035 mm x 3.035 mm | 6.07 mm x 6.07 mm |
| Pixel array | 16 x 16 | 8 x 8 |
| Channel readout | 256 | 64 |
| Combined readout | 32 | 16 |
| Scintillation material | LYSO | |
| Crystal size | 50 x 50 x 16 $mm^3$ | |
| PDE | 35%, 50%, 75% | |

Section 3.8.3. The bottom surface of the crystal is defined as polished. Photons that are transmitted through this surface reach the sensor pixel array. The refractive index between crystal and sensor array is that of optical grease (n=1.5). Other optical material characteristics of the scintillator and reflectors (wavelength dependencies, refractive indices, reflectance properties) are intrinsic to the LUT Davis model.

#### Photon detection efficiency, pixel size and combining channels

The SiPM pixel size is 6.07 x 6.07 $mm^2$ in an 8 x 8 array with a pixel pitch of 6.13 mm (values based on SensL SiPMs J-Series, now: onsemi). The signal for 3.035 x 3.035 $mm^2$ pixels in a corresponding 16 x 16 array is selected from the distribution of photons on the 6.07 x 6.07 $mm^2$ in the 8 x 8 array. For simplicity, we refer to 3 mm and 6 mm pixel sizes throughout this work. Combined channels refers to summing the signal from rows and columns. For 6 mm pixels this means reducing 64 (8 x 8) channel readout to 16 (8 + 8) channels. For 3 mm the reduction is from 256 (16 x 16) channel readout to 32 (16 + 16) channels. This is a channel reduction factor of 4 and 8, respectively. PDEs of 35%, 50% and 75% are modelled. An overview is provided in Table 4.1. The details on PDE modelling including a detailed analysis and discussion can be found in Section 6.4.

### 4.2.2 Detector calibration and positioning algorithm

In the first paragraph we describe the general concept and then move on to a detailed description of the methods.

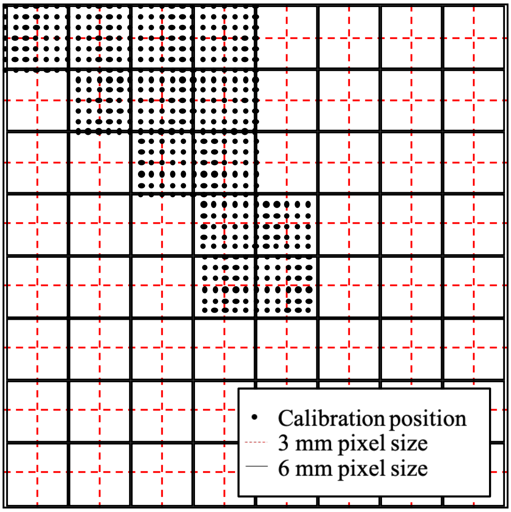

**Figure 4.2:** The simulated photodetector array of 3.035 x 3.035 $mm^2$ and 6.07 x 6.07 $mm^2$ pixels with respect to the calibration positions. The symmetry of the detector allows to characterize the whole area by only acquiring data at the indicated calibration positions.

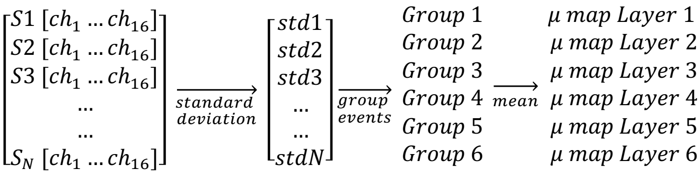

**Figure 4.3:** The flowchart depicts how the calibration data for the given set-up is organised for MNN positioning. S1 to $S_N$ are the event signals each consisting of 16 channels $ch_1$ to $ch_{16}$. For each event the standard deviation std1 to stdN over the 16 channels is calculated. The events are sorted according to this standard deviation and separated in six groups. From each group the mean signal per channel is calculated and saved. This is repeated for each calibration position.

To determine the 2D interaction position of a scintillation event, a MNN algorithm is used (cfr. Section 3.7.3). In principle, a large calibration data set is acquired with a pencil beam source at a small pitched grid on the crystal surface. For each position in the calibration data set the mean of all signals is calculated and stored in a calibration map. A test signal is then classified to the nearest neighbour within the calibration map with the signal that has the least square difference. A strong signal variation can be seen at a single position due to different gamma absorption depths in the crystal. As described in Section 3.7.3, an improved 2D positioning performance is obtained when the calibration data per position is first sorted according to the standard deviation of all individual SiPM pixel responses and then separated in multiple groups before calculating a mean signal for each of these groups. For the choice of the number of groups one must consider: 1. the amount of available calibration data to keep sufficient statistics when splitting the data into groups, 2. the computation time, 3. the increasing memory that is needed to store more calibration maps. Sorting and grouping the data according to the standard deviation does not only improve 2D positioning in the crystal, it can also give information about the 3D position of the interaction. A large standard deviation (with respect to other events at that calibration position) correlates to deep interactions, close to the SiPM array, and a small standard deviation to the ones closer to the crystal top. In Figure 4.4 the calibration maps are visualised for two depth layers. In the first column the top layer is presented for four different pixels, in the second column for layer 5 which is closer to the SiPM array. For each pixel its mean signal amplitude is shown at each calibration position. The SiPM pixels responds for a much larger range of calibration positions for layer 1 events than for layer 5. This correlates directly to the solid angle and scintillation light spread of the events from different interaction depths. For the sake of 3D positioning the size of each group is chosen equal to the expected number of events per depth layer indicated in Figure 4.1. Therefore, due to attenuation of the dense crystal material the group at the crystal top contains the most events.

A virtual, perpendicular source is stepped in 1 mm steps across selected areas of the detector. The source is perfectly collimated, pencil-shaped, and monoenergetic (511 keV). The symmetry of the detector allows us to characterize the whole area by scanning over the positions depicted in Figure 4.2. At each calibration position a minimum of 25,000 events was acquired. In each data set the sum of photons per event is recorded.

The photopeak position is determined and a lower threshold is set at the minimum between photopeak and Compton edge. This threshold strongly varies per detector calibration position and is lower at the edges due to more photon absorption. For a central calibration position, with PDE 50%, the threshold is at ~2,400 photons with photopeak at ~3,100 photons. Events outside the photopeak energy window are rejected. The remaining number of events is ~20,000. For a single event each signal channel is normalized by the sum of the charge in all channels. For this set-up, six layers were chosen to maintain sufficient events in the bottom layer (~1,000 events), and keep the number of the classification signals feasible. The number of classification signals is 223,494. For each layer the mean channel signal is calculated and stored in a look-up-table. The calibration data organization is shown in a flow chart in Figure 4.3. The calibration maps are interpolated to a calibration grid step size of 0.25 mm by linear 2D interpolation. Test events are positioned with a MNN algorithm. The data is first energy filtered and normalized as described above. In an exhaustive neighbour search, each test event is compared to calibration signals from all positions and all six layers. The calibration signal with the calculated least distance to the test signal is the selected nearest neighbour.

### 4.2.3 Spatial resolution

#### 2D resolution

The spatial resolution is obtained by positioning 2,000 events per calibration position in the central 10 x 10 $mm^2$ of the detector (Figure 4.5). The PSFs are measured by fitting a Gaussian function and measuring its FWHM in horizontal and vertical direction and presented as an average of all profiles. The positioning bias is defined as the distance between the real X, Y - position and the calculated position. The FWHM, the mean positioning bias and the median bias for all events are calculated for pixel sizes 3 mm and 6 mm, with individual and combined channel readout, and with PDEs of 35%, 50% and 75%. A statistical paired difference t-test with a p-value of $<0.05$ is calculated for all values discussed in this section.

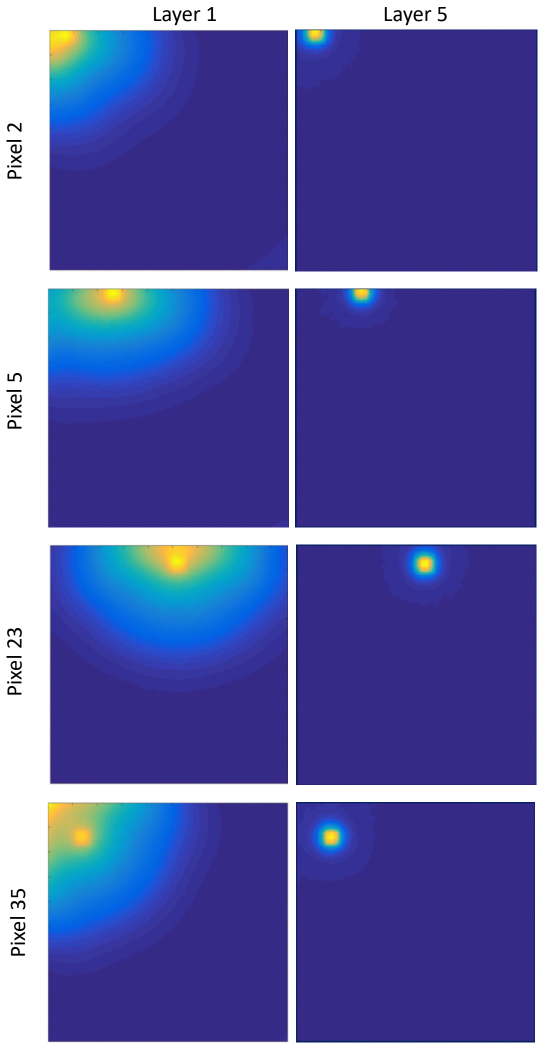

**Figure 4.4:** Calibration maps. The plots show the mean signal amplitude of an individual pixel at each calibration position. Here a subset of four pixels is presented: 2, 5, 23 and 35. The left column displays first layer pixel responses (close to entrance face), the right column displays layer 5 (deeper in the crystal, towards readout).

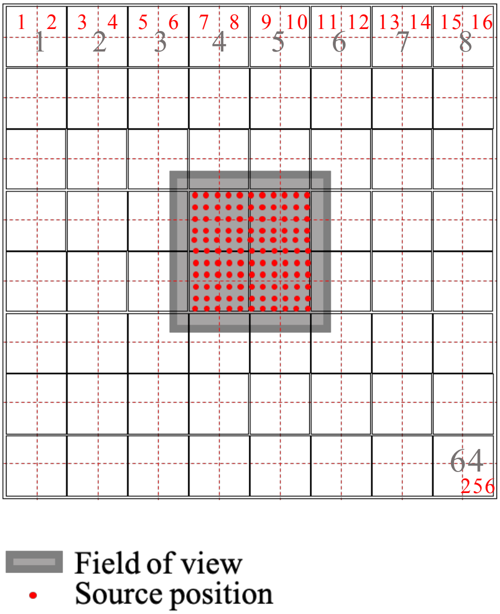

**Figure 4.5:** Simulation set-up for the spatial resolution estimation. The detector is evaluated at the indicated source positions. The numbers indicate the number of pixels in the first row for a 3 mm pixel readout (red) and a 6 mm pixel readout (black).

### Layer-dependent 2D resolution

The positioning algorithm uses 2D calibration data that was separated in six depth-dependent groups as described in Section 4.2.2. This allows to obtain depth information for each positioned event. The positioned events from Section 4.2.3 are histogrammed by the depth-layer. The spatial resolution is determined individually dependent on the depth-layer.

### Full detector resolution

The spatial resolution for the complete 50 x 50 $mm^2$ detector area is obtained by positioning 2,000 events at 49 x 49 positions with 1 mm distances. FWHM and positioning bias are obtained as described in

**Table 4.2:** Correlation between layer and gamma interaction depth.

| Layer | Discrete DOI [mm] | DOI range [mm] | Location |
|---|---|---|---|
| 1 | 14.25 | 12.01-16.00 | Crystal top |
| 2 | 10.87 | 9.25-12.00 | |
| 3 | 8.12 | 6.51-9.24 | |
| 4 | 5.60 | 4.21-6.50 | |
| 5 | 3.60 | 2.51-4.20 | |
| 6 | 1.50 | 0.00-2.50 | Close to SiPM |

4.2.3. Here, a data set with a 32 channel readout and a PDE of 75% is used.

### DOI - resolution

To determine the DOI resolution, 10,000 test events from the center of the detector with known 3D interaction information are positioned. For Compton scattered events the depth coordinate of the events' first interaction in the crystal is used as the depth metric. The MNN search is done, as previously, by comparing the test signals to calibration signals from all positions and all six depth layers. The determined nearest neighbour belongs therefore compulsively to one of the six depth-layers which allows to assign a specific depth to each positioned event. The discrete depth per layer is presented in Table 4.2. The determined depth-layers of the test events are presented in a histogram dependent on the real DOI coordinate. A layer determination is considered accurate if the DOI falls in between the defined DOI ranges (Table 4.2). The accuracy is given in percent per layer. For example, an event with a real DOI of 10 mm is accurately positioned in layer 2, the positioning error would be 0.87 mm. The calculation of the positioning error is done by comparing the real DOI to the discrete layer depth. The mean absolute error per layer is calculated as well as the standard deviation. Here, a data set with a 256 channel readout and a PDE of 75% is used.

## 4.2.4 Derenzo-like collimator

Perfect 511 keV pencil beam sources with diameters 0.45 mm, 0.6 mm, 0.9 mm, 1.2 mm, 1.5 mm and 1.8 mm are positioned in the center of the detector as depicted in Figure 4.6. The center-to-center distance

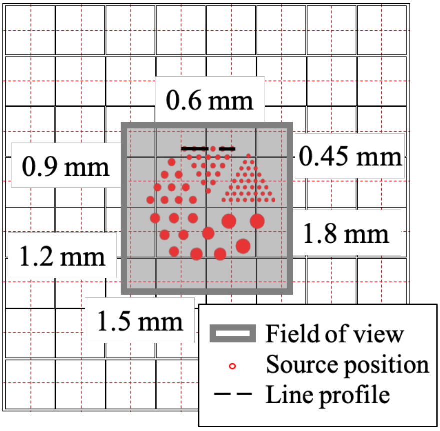

**Figure 4.6:** Spatial resolution determination with a Derenzo-like simulation set-up a) Perfect pencil beam sources of diameters between 0.45 mm - 1.8 mm are irradiating the detector.

between each source is twice its diameter. For this set-up a PDE of 50%, 3 mm pixel sizes and individual channel readout are used. 594,000 events are positioned and 2D histogrammed in an image. In a further step the histogram is normalized by the flood map of the uniformity measurement from Section 4.2.5. A line profile is drawn through the image at the center of 0.6 mm diameter sources to evaluate the distinguishability of individual point spread functions.

### 4.2.5 Uniformity

A flood source is placed in one corner of the detector covering 1/4th of the total area. 652,750 events are positioned. In a second step the events are discriminated depending on the positioned layer.

## 4.3 Results

### 4.3.1 Spatial resolution

#### 2D resolution

In Table 4.3 the spatial resolution is presented for two SiPM pixel sizes as a function of the number of readout channels and PDE. For 3 mm pixels and a 256 channel readout the FWHM values are 0.48 mm, 0.44 mm and 0.40 mm for a PDE of 35%, 50% and 75%, respectively. In a combined channel readout scenario (row and column summed) with 32 channels the same pixel size results in FWHM values of 0.52 mm, 0.47 mm and 0.42 mm, respectively. For 6 mm pixels and a 64 channel readout the FWHM values are 0.64 mm, 0.55 mm and 0.48 mm, respectively. In a combined channel readout scenario with 16 channels the same pixel size results in FWHM values of 0.66 mm, 0.56 mm and 0.48 mm, respectively. A graphical presentation of these values can be found in Figure 4.7 (‘All layers’).

For an individual channel readout an improvement of 0.12 ± 0.04 mm in resolution could be obtained by reducing the pixel size from 6 mm to 3 mm. For a combined readout the smaller 3 mm pixel size improved the resolution by 0.10 ± 0.04 mm. The PDE increase from 35% to 50% improved the resolution by 0.07 ± 0.03 mm, while a theoretical PDE increase to 75% could result in another improvement of 0.06 ± 0.02 mm. For 3 mm pixel size the reduction of readout channels from 256 to 32 channels (factor 8) has an impact of 0.03 mm. For 6 mm pixel size the reduction from 64 to 16 channels (factor 4) does not reduce the resolution significantly. While the mean positioning bias is higher than 1.7 mm for all set-ups, the median bias stays below 0.56 mm for 3 mm pixels and below 0.71 mm for 6 mm pixels.

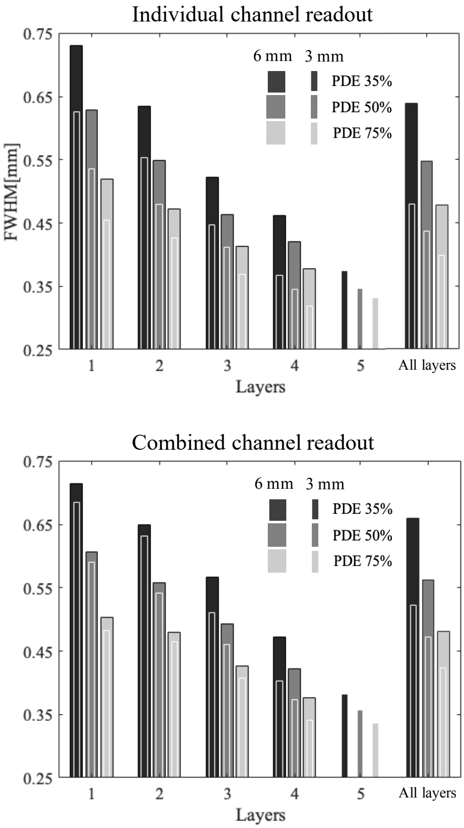

**Figure 4.7:** Layer-dependent spatial resolution. The spatial resolution is presented individually for depth layers 1-5 and for all layers combined for individual channel readout and combined channel readout. FWHM values from layer 6 (and layer 5 for 6 mm pixels) are not presented due to large positioning artefacts that do not allow to determine reasonable FWHM values. The column 'all layers' contains the resolution over all layers.

**Table 4.3:** Spatial resolution as FWHM[mm] is calculated separately for each layer and for all six layers combined at central 10 x 10 $mm^2$ of the detector. For each FWHM value the mean of FWHMs at 121 positions in horizontal and vertical direction is shown. Values in cursive are presented for the sake of completeness but are to be interpreted carefully because artifacts are dominating the histograms.

| **SiPM size** | 3 mm | | | | | | 6 mm | | | | | |
|---|---|---|---|---|---|---|---|---|---|---|---|---|
| **Readout channels** | 256 | | | 32 | | | 64 | | | 16 | | |
| **PDE[%]** | 35 | 50 | 75 | 35 | 50 | 75 | 35 | 50 | 75 | 35 | 50 | 75 |
| **Spatial resolution FWHM [mm]** | | | | | | | | | | | | |
| L1 | 0.63 | 0.54 | 0.45 | 0.69 | 0.59 | 0.48 | 0.73 | 0.63 | 0.52 | 0.71 | 0.61 | 0.50 |
| L2 | 0.55 | 0.48 | 0.43 | 0.63 | 0.54 | 0.46 | 0.63 | 0.55 | 0.47 | 0.65 | 0.56 | 0.48 |
| L3 | 0.45 | 0.41 | 0.37 | 0.51 | 0.46 | 0.41 | 0.52 | 0.46 | 0.41 | 0.57 | 0.49 | 0.43 |
| L4 | 0.37 | 0.34 | 0.32 | 0.40 | 0.37 | 0.34 | 0.46 | 0.42 | 0.38 | 0.47 | 0.42 | 0.38 |
| L5 | 0.38 | 0.35 | 0.33 | 0.38 | 0.36 | 0.34 | *0.45* | *0.43* | *0.39* | *0.46* | *0.42* | *0.39* |
| L6 | *0.35* | *0.31* | *0.30* | *0.32* | *0.33* | *0.31* | *0.38* | *0.36* | *0.34* | *0.36* | *0.38* | *0.35* |
| **All layers** | **0.48** | **0.44** | **0.40** | **0.52** | **0.47** | **0.42** | **0.64** | **0.55** | **0.48** | **0.66** | **0.56** | **0.48** |

Table 4.4: Bias mean is the mean of all calculated x,y - biases per layer and all positioned events, respectively. Values in cursive are presented for the sake of completeness but are to be interpreted carefully because artifacts are dominating the histograms.

| **SiPM size** | 3 mm | | | | | | 6 mm | | | | | |
|---|---|---|---|---|---|---|---|---|---|---|---|---|
| **Readout channels** | 256 | | | 32 | | | 64 | | | 16 | | |
| **PDE[%]** | 35 | 50 | 75 | 35 | 50 | 75 | 35 | 50 | 75 | 35 | 50 | 75 |
| **Mean bias** | | | | | | | | | | | | |
| L1 | 1.31 | 1.26 | 1.18 | 1.34 | 1.33 | 1.37 | 1.33 | 1.26 | 1.26 | 1.43 | 1.43 | 1.37 |
| L2 | 1.50 | 1.46 | 1.42 | 1.45 | 1.45 | 1.41 | 1.46 | 1.47 | 1.42 | 1.41 | 1.41 | 1.39 |
| L3 | 1.91 | 1.89 | 1.79 | 1.63 | 1.64 | 1.66 | 1.84 | 1.83 | 1.81 | 1.63 | 1.73 | 1.75 |
| L4 | 2.27 | 2.20 | 2.20 | 1.87 | 2.02 | 1.92 | 2.44 | 2.42 | 2.53 | 2.23 | 2.12 | 2.12 |
| L5 | 2.97 | 2.81 | 2.63 | 2.82 | 2.84 | 2.82 | 2.82 | 2.80 | 2.80 | 2.90 | 2.74 | 2.76 |
| L6 | 2.52 | 2.63 | 2.64 | 2.18 | 2.12 | 2.18 | 2.30 | 2.18 | 2.19 | 1.91 | 1.85 | 1.88 |
| All events | 1.89 | 1.83 | 1.78 | 1.72 | 1.73 | 1.73 | 1.85 | 1.80 | 1.79 | 1.77 | 1.74 | 1.73 |

**Table 4.5:** Bias median is the median of all calculated x,y - biases per layer and all positioned events, respectively.

| **SiPM size** | 3 mm | | | | | | 6 mm | | | | | |
|---|---|---|---|---|---|---|---|---|---|---|---|---|
| **Readout channels** | 256 | | | 32 | | | 64 | | | 16 | | |
| **PDE[%]** | 35 | 50 | 75 | 35 | 50 | 75 | 35 | 50 | 75 | 35 | 50 | 75 |
| **Median bias** | | | | | | | | | | | | |
| L1 | 0.50 | 0.50 | 0.35 | 0.56 | 0.50 | 0.35 | 0.56 | 0.50 | 0.35 | 0.56 | 0.50 | 0.35 |
| L2 | 0.56 | 0.56 | 0.50 | 0.56 | 0.56 | 0.50 | 0.56 | 0.56 | 0.50 | 0.56 | 0.56 | 0.50 |
| L3 | 0.79 | 0.71 | 0.56 | 0.56 | 0.56 | 0.50 | 0.56 | 0.56 | 0.56 | 0.56 | 0.56 | 0.56 |
| L4 | 0.71 | 0.56 | 0.56 | 0.56 | 0.56 | 0.50 | 0.75 | 0.75 | 0.79 | 0.79 | 0.71 | 0.56 |
| L5 | 0.75 | 0.56 | 0.56 | 0.71 | 0.71 | 0.71 | 1.06 | 1.00 | 1.03 | 1.03 | 1.12 | 1.06 |
| L6 | 1.00 | 1.00 | 1.00 | 1.00 | 0.90 | 0.95 | 1.41 | 1.41 | 1.41 | 1.25 | 1.25 | 1.25 |
| All events | 0.56 | 0.56 | 0.56 | 0.56 | 0.56 | 0.50 | 0.71 | 0.71 | 0.71 | 0.71 | 0.71 | 0.56 |

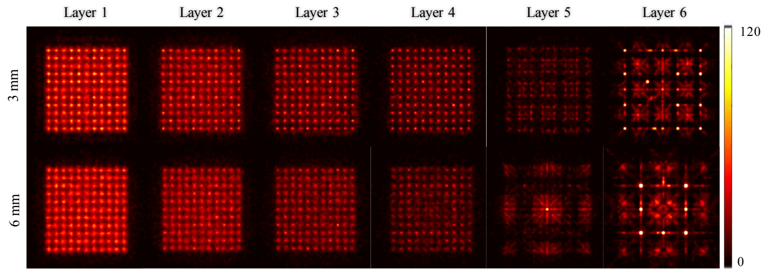

**Figure 4.8:** Layer-dependent positioning performance for two different pixel sizes. The impact of the pixel size on the positioning performance is most prominent in layers 5 and 6. The central 10 x 10 $mm^2$ are evaluated.

### Layer-dependent 2D resolution

In Table 4.3 and Figure 4.7 the spatial resolution dependent on the depth layer is presented. Values in Table 4.3 printed in cursive should be interpreted carefully (not presented graphically in Figure 4.7), because artefacts are dominating (see Figure 4.8, layer 5 and 6), and it is thus not meaningful to determine FWHM values. For almost all configurations, the resolution improves towards layer 5 (close to the SiPM array). The layer dependency is smaller for 6 mm pixels and for higher PDEs. In the combined channel scenario the resolution difference between 3 and 6 mm pixel size is generally less pronounced than in the individual channel readout scenario. The spatial resolution dependent on the depth-layer is presented in Figure 4.8. For 3 mm pixels the artefacts concentrate in layer 6 and a directional bias can be seen in layer 5. For 6 mm pixel size strong artefacts are visible in layer 5 and 6.

### Full detector resolution

In Figure 4.9 a) the detector spatial resolution in FWHM and positioning bias for the whole detector is shown. The corresponding histogram of the estimated event positions is presented in Figure 4.9 b). Table 4.6 shows mean FWHM and mean and median bias values. The spatial resolution in FWHM for the whole detector is 0.56 mm FWHM. The mean and median positioning bias is 1.41 mm and 0.56 mm, respectively. For the edge region illustrated in Figure 4.9 a) the resolution degrades to 0.72 mm FWHM and mean and median bias of 1.46 mm and 0.75 mm,

**Table 4.6:** Spatial resolution as FWHM [mm]

| | Whole detector | Edge | Corner |
|---|---|---|---|
| **Mean FWHM** | 0.56 | 0.72 | 0.80 |
| **Mean bias** | 1.41 | 1.46 | 1.45 |
| **Median bias** | 0.56 | 0.75 | 0.9 |

respectively. For the corner region illustrated in 4.9 a) the resolution degrades to 0.8 mm FWHM and mean and median bias of 1.45 mm and 0.9 mm, respectively.

### DOI - resolution

Figure 4.10 shows the correlation between the estimated depth-layers and the real DOI. The depth distributions per layer are asymmetrical and feature large tails towards the crystal top. The dotted lines indicate the fraction of events that is not scattered. The layer classification accuracy is high towards the crystal top with 97% and decreases towards the lower layers (Table 4.7). The amount of events positioned in layer 1 is highest and decreases towards layer 5. Layer 6 contains slightly more events than layer 5. The relative amount of positioned and expected events per layer are listed in Table 5. The mean absolute DOI positioning error and its standard deviation are also presented in Table 4.7 . The mean error is ~1 mm at the crystal top and increases towards the deeper layers to ~3 mm. The standard deviation increases in a similar manner. In contrast, the values in parenthesis are from the non-scatter scenario. The layer positioning accuracy is between 83 - 99%. The mean error range from about 0.9 mm in layer 1 to 0.39 mm in layer 5. Considering the relative amount of events per layer the overall accuracy and positioning error is calculated. The overall layer accuracy is 72.2% and the mean positioning error is 1.6 mm.

## 4.3.2 Derenzo-like collimator

The expected resolution from the given set-up (PDE 50%, 3 mm pixels, 256 channels) is 0.44 mm. Figure 4.11 shows that sources up to 0.6 mm can be distinguished from one another. The next smaller sources 0.45 mm cannot be distinguished.

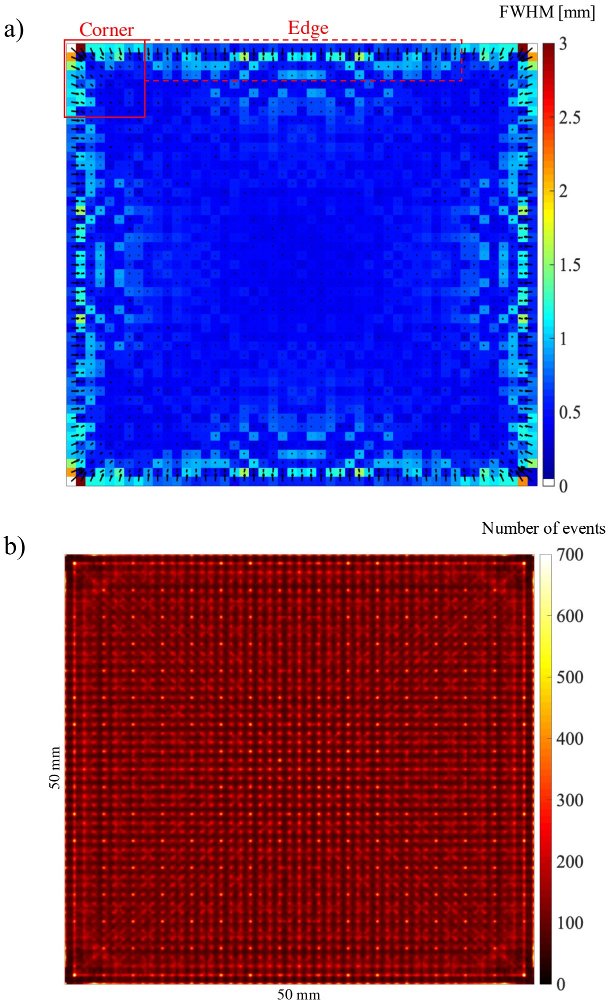

**Figure 4.9:** Full detector positioning performance. a) Spatial resolution in FWHM of each position of b). Positioning bias is given as vectors. b) 2D histogram of 2000 positioned events per calibration position in a 49 x 49 grid.

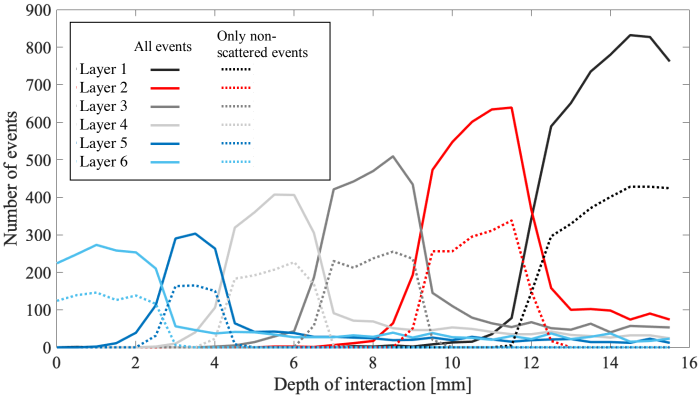

**Figure 4.10:** Detector depth resolution measurement. 10,000 events with known interaction coordinates are positioned. On the x-axis, '0' represents the depth of the SiPM pixels and '16' the entrance face of the detector. The DOI is presented dependent on the determined depth layer. The histograms feature long tails towards the right (crystal top). Non-scattered events are presented in dotted line style. The tails are caused by the Compton scattered events.

**Table 4.7:** Detector depth resolution measurement. Values in parenthesis present the non-scatter case. The last row gives the mean of all layers considering the relative number of events in each layer. The overall layer positioning accuracy is 72.2%, the absolute depth positioning error is 1.6 mm. The scattered events degrade the positioning accuracy majorly.

| Layer | Layer Accuracy [%] | Positioned events /expected [%] | Mean absolute error [mm] | Standard deviation [mm] |
|---|---|---|---|---|
| 1 | 96.57 (99.75) | 28.27 / 29.5 | 0.99 (0.92) | 0.72 |
| 2 | 70.69 (90.20) | 21.73 / 22.95 | 1.18 (0.72) | 1.11 |
| 3 | 66.45 (91.19) | 17.14 / 17.87 | 1.58 (0.67) | 1.78 |
| 4 | 58.38 (83.05) | 13.60 / 13.91 | 1.91 (0.62) | 2.46 |
| 5 | 50.69 (83.56) | 8.01 / 10.83 | 2.3 (0.39) | 3.17 |
| 6 | 54.58 (85.03) | 11.25 / 4.94 | 3.03 (0.73) | 3.87 |
| All | 72.2 | 100 / 100 | 1.6 | |

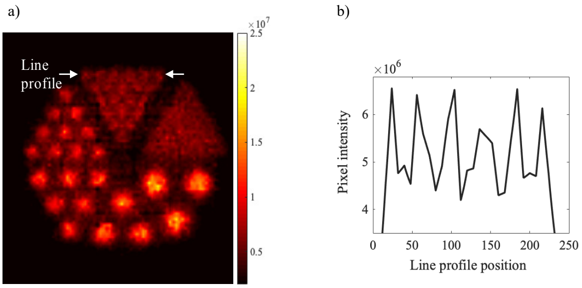

**Figure 4.11:** Spatial resolution determination with a Derenzo-like simulation set-up a) Histogram of estimated source positions normalized by uniformity measurement of 50% PDE 3 mm 256 channels. b) The indicated line profile is drawn through 0.6 mm sources. The sources can be distinguished from each other.

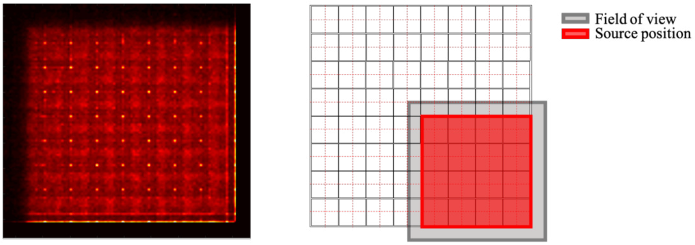

**Figure 4.12:** Evaluation of detector uniformity with a flood source. A flood source is placed over 1/4th of the detector with 3 x 3 mm$^2$ SiPM pixels and 50% PDE. Histogram of the estimated (reconstructed) event positions showing hot spots and edge non-uniformities.

### 4.3.3 Uniformity

In Figure 4.12 the uniformity can be evaluated qualitatively. In Figure 4.13 the layer-dependent uniformity plots show that the artefacts are characteristic to the DOI of the event.

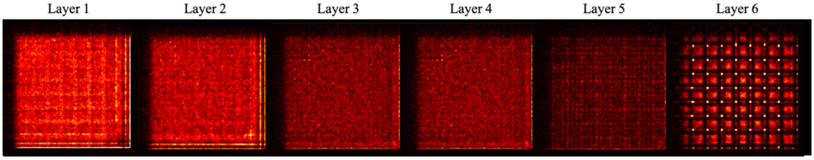

**Figure 4.13:** The histogram data from Figure 4.12 is presented with (reconstructed) depth-layer discrimination. Hot spots originate mainly from layer 6 (SiPM-close). Edge artefacts occur in all layers.

## 4.4 Discussion

### 4.4.1 Spatial resolution

#### 2D resolution

As results indicate, the pixel size has a significant impact on the resolution, for all tested PDEs. Especially for individual channel readout scenarios, the smaller pixel size improves the outcome, but also for a combined readout smaller pixel sizes can improve resolution. Smaller pixels allow to obtain a more detailed representation of the light distribution projected onto the photodetector. The light distribution again characterizes the position of the gamma interaction and therefore allows for more precise positioning. The downside of smaller pixels is the smaller SNR introduced by the smaller solid angle of the scintillation light on an SiPM pixel and therefore a lower number of detected photons. In terms of cost, smaller SiPM pixel sizes are similar in price per area, but the much higher number of channels that need to be read out with appropriate electronics are increasing the cost proportionally. Here a combined readout can be applied to reduce the overall cost of a detector by summing channels. In the presented set-ups, the number of channels is drastically reduced by 87.5% and 75% for 3 mm and 6 mm pixel sizes, respectively. The resulting loss of resolution is only <8% for 3 mm pixels and insignificant for 6 mm pixels. If one is interested in lowering detector costs the results strongly imply to use a reduced channel readout while maintaining high resolution. However, recent research motivations also aim at high timing resolution which might degrade when combining the signals from multiple channels. Also note that superior resolution can be obtained with less channels when using 3 mm pixels and combined-channel readout (32 channels) instead of an individual channel readout

(64 channels) and 6 mm pixel size. The artefacts are depth dependent and discussed in the next section.
In our simulations we demonstrate the ultimate spatial resolution that can be obtained with an idealized set-up. In a real set-up it is very difficult to ensure the same accuracies. Factors that deteriorate the spatial resolution or make optical simulations less reliable are: 1. the scintillation crystal itself which can have internal defects 2. inhomogeneous crystal surface treatment 3. bad coupling of the crystal to the SiPM array (non-uniform light extraction, air bubbles or misalignments) 4. light entering the detector 5. the calibration source diameter size 6. alignment of calibration beam 7. sufficient calibration data statistics 8. SiPM PDE inhomogeneity 9. multiple sources of additional noise in the signal processing chain 10. intrinsic radioactivity of LYSO. Some of these factors will be be covered in Chapter 6.

### Layer-dependent 2D resolution

A strong depth-dependent spatial resolution is presented that also depends on pixel size, PDE and number of readout channels. The results show us that on the one side resolution improves when gamma interactions occur rather close to the SiPM array than to the crystal top, but on the other side an interaction too close to the SiPM array leads to artefacts. These artefacts can be explained by insufficient light spread which means that most scintillation light is captured by a single SiPM pixel. The interaction position is then simply estimated as the pixel center. For those SiPM-close events the positioning bias will be determined mainly by the pixel size that means even without any light spread a smaller pixel leads to smaller positioning bias. One should also consider that the relative number of events occurring close to the array is dependent on the scintillator thickness. The thicker the crystal the smaller is the ratio of gamma interactions close to the array.
Another source of artefacts originates from Compton scattered events. As seen in Figure 4.10 the lower layers capture events that first interacted in the upper layers but then scattered. Scatter is the reason for the decreasing DOI positioning accuracy and also the artefacts that are not related to light spread issues. The depth-dependent resolution differences can be linked to the noise that is present in the respective set-up and has multiple sources. First, noise is introduced with lower PDEs. Second, a 3 x 3 mm$^2$ pixel detects only about 1/4th of the

number of photons compared to a 6 x 6 mm$^2$ pixel. Third, due to the solid angle, with increasing distance of the scintillation position to the array, the number of photons per area decreases. Therefore, the more noise the set-up includes the stronger is the depth dependency of spatial resolution.

#### Full detector resolution

Compared to the detector center the resolution degrades towards the edge of the detector from 0.42 to 0.72 mm FWHM. The resolution at the corner of the crystal degrades further to 0.8 mm FWHM. This leads to a whole detector resolution of 0.56 mm FWHM. The resolution degradation is limited to a relatively small area of a few millimetres on the detector edges and corner. The signal is more complex and influenced by the edge reflections. An improvement could potentially be obtained by calibrating in a finer grid at the edges.

#### DOI - resolution

The higher amount of events in the top layers occurs due to the attenuation of the crystal material. The figure shows that each layer also includes events from all shallower depths of the crystal. Considering that a high percentage of events are Compton scattered and can be distinguished in a simulation set-up, these long tails are identified as scattered events. The applied positioning technique is based on average detector responses which leads to a loss of information on scattered events and makes positioning of those difficult. Nevertheless, 80% of events are positioned with high accuracy, a mean error of 1.6 mm which is very useful for the improvement of image quality and potentially timing measurements in TOF PET systems. Much lower errors and higher accuracies are obtained when scattered events are eliminated from the data set.

### 4.4.2 Derenzo-like collimator

This simulation shows that high resolution cannot only be obtained at the detectors calibration positions but also at random other center positions. A small resolution degradation with this set-up is observed and expected. First of all, because the statistics per pixel are lower than in Section 4.3.1 and second, because the tails of the adjacent Derenzo spheres are overlapping each other which lowers their distinguishability from each other.

### 4.4.3 Uniformity

The uniformity measurement shows how much the positioning performance is diverging at the detector and crystal edges. The overall uniformity shows hot spots that follow a pattern that can be linked to the underlying SiPM pixel grid of 3 mm steps and edge artefacts in a region of ~1.5 - 1.75 mm from the crystal edges. With a total area of 50 x 50 $\mathrm{mm}^2$ the degradation area at the edges is 12 - 14%.

## 4.5 Conclusion

Optical simulations were performed to predict the performance of a thick monolithic scintillation detector and investigate how several factors influence the spatial resolution. Here we focussed on testing the influence of the SiPM pixel size, the PDE and combining readout channels. The determined 2D spatial resolution in the detector center is 0.40-0.66 mm FWHM. Towards the edges and corner of the detector the resolution slightly degrades. Smaller pixel sizes and higher PDE significantly improved the spatial resolution. Reducing the number of readout channels by a factor of 4 did not significantly change the resolution. Therefore, a single channel readout is not always necessary to maintain high spatial resolution. The DOI is estimated with a depth layer approach and reaches 72% accuracy and a mean absolute positioning error of 1.6 mm. The simulation results give strong design indications and demonstrate the ultimate spatial resolution that is obtainable under optimal conditions like a perfect calibration source, perfect coupling and alignment of crystal and SiPMs, no intrinsic activity, etc. The data processing framework developed for the simulated data will be the basis for the data processing of the prototype detector in the next chapter. The software to generate calibration maps from the event data and the positioning algorithm can be used with only small adaptations. Furthermore the simulation model will be used in Chapter 6 to further analyse the degrading factors and in Chapter 7 to improve the real detector using simulated data.

# 5

# Experimental detector performance evaluation

## 5.1 Introduction

The previous chapter demonstrated the ultimate spatial resolution that can be obtained with a thick monolithic PET detector under idealized conditions. The simulation study provides insight into many parameters and creates the basis to understand the physical processes in the detector. Hence, optical simulations are the ideal preparation for the development of the detector prototype described in this chapter. Furthermore, the generated calibration data serve as the basis for the development of the data processing framework such as filtering, positioning, and evaluation algorithms. However, one must carefully evaluate the obstacles faced in experimental set-ups. These obstacles are identified and discussed throughout this chapter and the next Chapter 'Main degrading factors on spatial resolution'. The crystal properties of our prototype are as previously simulated while the readout scheme is narrowed to one of the multiple simulated ones, i.e. 6 x 6 $\mathrm{mm}^2$ pixels, 16 channels, rows and columns summed. Summing rows and columns reduces the number of readout channels by a factor of 4. The readout electronics of our detector are designed for cost-efficiency. The 2D spatial resolution and DOI are evaluated as well as the energy resolution and detector uniformity. The event positioning is extended from the previously applied MNN algorithm to a neural network. Both algorithms are presented side-by-side and compared for most evaluations. Neural networks are very applicable to solve the inverse problem of linking light distributions to the gamma interaction position especially with respect to the non-linear

behaviour at the crystal edges. In the recent paper by Decuyper et al. [100] we found that neural networks achieve superior positioning performance when applied to the same simulated data as presented in the previous chapter. Therefore we train and evaluate the neural network design also on the experimental data.
In Section 2.3.3 'Fundamental resolution limits of PET' we discussed the influence of non-collinearity, positron range, and intrinsic detector resolution on the obtainable system resolution. Typical clinical systems have a diameter of 60-80 cm and are utilized with a $^{18}$F tracer, hence, the ideal detector resolution should be better than 1.3 mm to not become the dominating factor. The resulting system resolution is then around 2 mm which is the limit imposed by positron physics under the conditions mentioned above. Applications in systems with smaller diameter such as brain PET systems can also profit from better spatial resolutions. In conclusion, in this chapter we present our prototype detector aiming at 1.3 mm spatial resolution or better, using the MNN positioning algorithm and neural networks.
The work presented in this chapter resulted in one peer reviewed A1 journal publication [119] and two conference contributions [120, 121].

## 5.2 Materials and methods

### 5.2.1 Experimental set-up

The investigated detector is a monolithic 50 x 50 x 16 mm$^3$ LYSO (Epic Crystal) crystal, readout by SiPMs at the back (Figure 5.1). The surfaces have a rough black painted finishing on the crystal sides (16 x 50 mm$^2$) and a black painted specular reflector attached to a polished crystal top (50 x 50 mm$^2$). The crystal is coupled with optical grease (St. Gobain BC630) to an 8 x 8 array of 6 x 6 mm$^2$ SiPMs (onsemi MicroFJ-60035-TSV). The crystal and SiPMs are placed in a light-tight aluminium housing (Figure 5.2). Similar to what has been previously published [44, 81, 122] the signals of 64 SiPM pixels are combined to 16 (8+8) channels by summing rows and columns (Figure 5.3). This is done by using a resistor network that splits the current of each pixel in two. One half of the current ends up in the column signal and the other half ends up in the row signal. The 16 rows and columns currents are then amplified using a current-to-voltage amplifier (based on an operational amplifier). In a next step the amplified signal is converted to a differential signal, using a differential amplifier. The differential signal is digitized by a free-running ADC with a sampling frequency of 64 MHz.

### 5.2.2 Calibration data acquisition

The detector is calibrated with a collimated $^{68}$Ge source (69 MBq) placed in a tungsten collimator forming a beam with a diameter of 0.6 mm. The collimated beam is orthogonal to the optical table irradiating the detector which is mounted on a three-dimensional robot stage (Owis LTM 80, positioning error 25 $\mu$m/100 mm) (Figure 5.1). Calibration data is acquired in a 49 x 49 grid for 70s per position. A calibration and an evaluation dataset are extracted from the acquired data. For the calibration dataset the events are pre-positioned with an Anger logic algorithm for each calibration position. A ROI is then drawn around the calibration beam position to extract only data from the irradiated position and to avoid events from the intrinsic $^{176}$Lu radiation of the scintillator. An energy window of 20% is applied. For the neural network validation an additional dataset is acquired at 1 mm grid steps in the detector center (10 x 10) with an offset of 0.5 mm with respect to the calibration positions. This validation set is acquired to avoid overfitting (more detail in Section 5.2.4). For clarity we summarise that for both algorithms the training (calibration) data is energy filtered and a position filter is applied. For the evaluation (test) dataset an energy filter but no ROI selection (no position filter) is applied. Therefore, only those scattered events are filtered that have not deposited their full energy in the detector (i.e., Compton interaction then gamma exits the crystal).

### 5.2.3 Mean nearest neighbour positioning algorithm

The implementation of the MNN algorithm closely resembles that in Chapter 4. Here we explain the methods again with respect to the differences in experimental measurements. The calibration data for the MNN algorithm is extracted from the Anger histogram as a ROI of 37 high intensity pixels (pixel size = 0.26 mm). The remaining number of events per position for the 0.6 mm beam is on average 4930 ± 730. Each event first undergoes a baseline correction and is normalized by

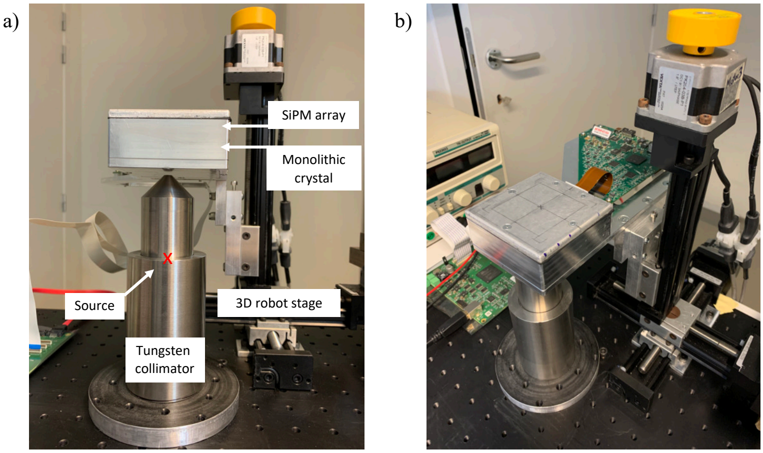

**Figure 5.1:** a) The calibration set-up consists of a collimator forming the calibration beam and the detector that is mounted on a 3D robot stage b)

dividing the signal in each channel by the sum of all 16 channels to make it energy independent. For each single event we calculate the variance between the values of the 16 channel signals. These variances are then used to sort the calibration events into six groups. For example, the first group includes signals with small variances referring to events that interacted at the top of the crystal where the light spread is broad and many SiPM pixels have a similar value. On the contrary, the sixth group includes events where the gamma interaction occurred close to the SiPM array and most of the light is captured by a small number of SiPM pixels and therefore the signal has a larger variance. The final step is to calculate the mean signal in each of the channels per group. For each calibration position we then end up with 6 reference signals which are the mean of all the events per "depth"-group. In Figure 5.4 these mean signals are presented for a calibration position in the detector centre. The number of events per group, here called layers, best resembles the expected depth distribution derived from Beer-Lambert attenuation law with these splits: 29.5%, 22.95%, 17.87%, 13.91%, 10.83% and 4.94% for layer 1 to 6 respectively. For simplicity we assume the beam to be perpendicular, however, a certain opening angle is introduced by the collimator geometry.

The six layers do not only provide depth information but also improve 2D spatial resolution [97]. The reason for the improvement is that the signal at one 2D position varies greatly between the different interaction

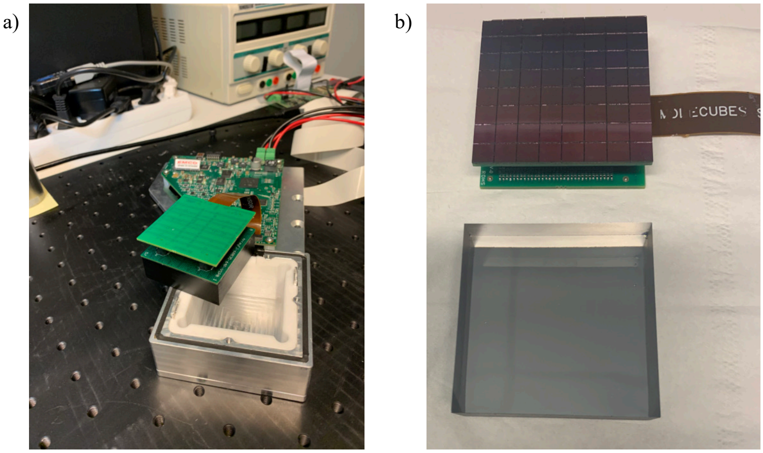

**Figure 5.2:** The light-tight aluminium housing encapsulates the black-painted scintillation crystal coupled to the SiPM array.

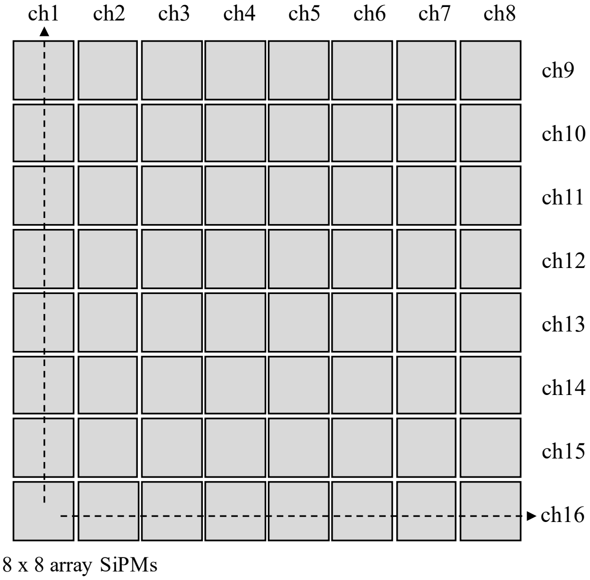

**Figure 5.3:** The signals of the 64 SiPM pixels are summed per row and column to a total of 16 readout channels.

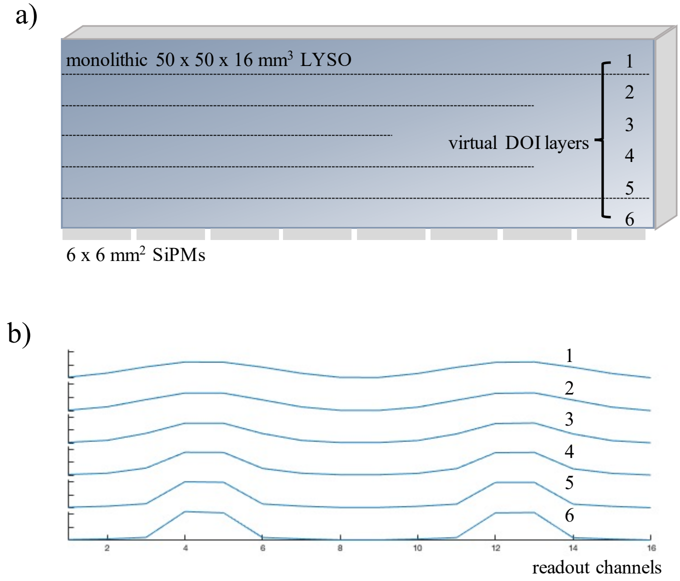

**Figure 5.4:** a) Detector geometry with SiPM readout and virtual DOI layers. b) 16-channel signal of an event in the detector center dependent on layer. The channel variance is smaller in layer 1 and increases towards layer 6.

depths. Using a single mean signal over all interaction depths would be a too general representation of the signal variety. Therefore, using mean events from different (here six) depth-groups leads to a better position determination using the MNN algorithm. The ideal number of layers is determined in Section 5.2.5. For each layer the mean signal is calculated, interpolated to a grid size 0.26 mm and stored in look-up-tables. The evaluation data is positioned with a nearest neighbour algorithm implemented in Matlab (‘knnsearch’-function). In an exhaustive neighbour search, each test event is compared to all reference signals from all six depth layers. The calibration signal with the calculated least distance to the test signal is the selected nearest neighbour.

### 5.2.4 Neural network positioning algorithm

The calibration data for the neural network is defined by a ROI of 109 high intensity pixels (pixel size = 0.26 mm) in the Anger histogram.The ROI is larger for the neural network calibration dataset than in the MNN dataset. A larger ROI includes more scattered events and especially the ones that scattered with a larger angle in a direction more parallel to the entrance face. While the neural network training profits from the ‘far’- scattered events and learns to position them, the MNN algorithm filters scattered events in the process of taking the mean signal of many events. Therefore, it is counterproductive to include more scattered events in the MNN training dataset. A fully connected artificial neural network is designed with 16 inputs (from 8 + 8 SiPM signals), three hidden layers containing each 256 neurons and three outputs (x, y and z position coordinates) as illustrated in Figure 5.5. Leaky ReLU activation is added after every hidden layer. The network is trained using the AdamW optimization algorithm with an initial learning rate of $10^{-3}$, a mini-batch size of 256 events and L1 loss between predicted and ground truth calibration position as optimization metric. L2 weight decay is set to $10^{-2}$. The calibration beam positions were used as ground truth x and y coordinates. The z coordinate label was set to the DOI layer (label 1 to 6) the event belongs to as obtained from the events’ variance (similar to Section 5.2.3). The number of events per calibration position is split with 28.85% for layer 1 with the smaller standard deviations, 22.03% for layer 2, 17.4% layer 3, 13.8% layer 4, 10.85% layer 5 and 8.07% for layer 6 with the larger standard deviations. Each event is independently standardized to zero mean and unit variance. The training set contains 1000 events per calibration position and one training epoch is defined as an iteration over 100 events per position randomly extracted from the training set. After every epoch, the network is validated on data acquired in a 1 mm intermediate grid in the detector center (9 x 9 $mm^2$, 10 x 10 positions, 1000 events/position). This allows to regularly check and prevent potential overfitting on the training grid positions. Based on the validation loss, learning rate is halved every 10 epochs without improvement and training is stopped if the loss did not improve for 50 epochs. The deep learning methodology is implemented in python using PyTorch and the network is trained on an 11 GB NVIDIA RTX 2080Ti GPU. Optimization of the network architecture, training set size and training procedure was done based on simulation data of the same set-up. For full detail we refer the reader to the paper of Decuyper et al. [100].

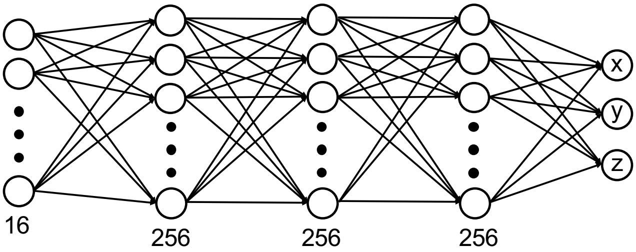

**Figure 5.5:** Neural network architecture. Input of 16 (8+8 summed row and column) signals and three output coordinates x, y and z.

### 5.2.5 Performance Evaluation

The performance is evaluated based on two parameters: FWHM and 1D/2D-bias. The FWHM [mm] is the full width at half maximum of the Gaussian fit to the horizontal and vertical line profile of the PSF in the 2D histogram of all events from all depths per calibration position. For the estimation of the FWHM we need the peak value of the distribution and the width of the distribution at half the peak value. To determine these two parameters most accurately, we fitted a Gaussian to the central peak region (including all values over a threshold T = 0.25 * peak value). The FWHM could also be evaluated simply by extracting the peak of the distribution and the width of the distribution at half the maximum without fitting a function to the distribution. The low sampling on the x-axis, however, does not allow to determine the FWHM at exactly the half maximum. Therefore, an interpolation between the data points or a fit is needed to determine these values. The positioning bias [mm] is the distance between the peak of the PSF and the known calibration position in x and y direction. The 2D bias [mm] is the 2D distance between the peak of the PSF and the true calibration position. Mean and median values are evaluated for the full detector (5 x 5 $\text{cm}^2$) and the detector centre (3 x 3 $\text{cm}^2$), respectively. Note that PSFs at the detector edges mostly do not resemble a Gaussian distribution resulting in inaccurate FWHM values. As an alternative measure for spatial resolution over the whole detector including the edges the bar phantom measurement can be used.

### Spatial resolution estimation

The evaluation dataset includes 30000 energy-filtered events (20% energy window) per position without ROI selection. The results are not corrected for the remaining source size of 0.6 mm. A bias correction for the 2D - position between the two calibrations is done with 0.3 mm and 0.18 mm in x-direction and 0 mm and -0.18 mm in y-direction for the MNN algorithm and neural network positioning respectively. The bias originates from the disassembly and assembly steps in between the two calibrations.

### DOI estimation

For positioning with the MNN algorithm each of the reference events automatically belongs to a certain depth-layer defined by the signal variance and therefore DOI of the event. The principle is described in detail in Section 5.2.3. For the neural network the DOI is determined by a network trained on the DOI labels defined by the signal variance. This is explained in Section 5.2.4. To evaluate the DOI estimation of both algorithms the predicted relative number of events in each of those layers is compared. We compare to (i) the theoretical number of events that we expect by the attenuation of the crystal according to Beer-Lambert law and (ii) the results we previously obtained from optical simulations [71] modelling the same detector geometry, calibration procedure and MNN positioning. Note that in the simulations the DOI was evaluated for only the centre 10 x 10 $\text{mm}^2$. Here, we use the calibration dataset from the 1.0 mm beam with 109 pixels.

### Energy resolution

The energy resolution is evaluated per calibration position. The sum of each event signal from the calibration dataset (1.0 mm beam, 37 pixels) is histogrammed and a Gaussian is fit to the distribution. Similar to what is described in Section 5.2.5 the Gaussian is fitted to the photopeak so that the fit accurately represents the peak of the actual distribution and the width at half maximum. To determine these two parameters most accurately, we fitted a Gaussian to the central peak region (including all values over a threshold $T = 0.25 * \text{peak value}$). Figure 5.10 shows the original distribution and the Gaussian fit. A remainder of the background signal ($^{176}$Lu) is present in the energy histograms and explains the counts higher than what is expected from the Germanium source. The fit does not consider the tails from the Lutetium contamination.

### Uniformity

An uncollimated $^{68}$Ge point source (29 MBq) is placed at a distance of 52.5 cm of the detector. The acquired events are filtered with an energy window of 20% and then positioned with the MNN algorithm and neural network. The uniformity is further analysed by selecting the positioned events per DOI layer.

### Bar phantom

Additional to the analysis of the point spread function, a four-quadrant bar phantom designed for this study gives a more visual impression on the detector performance. With this phantom the spatial resolution of the detector can be assessed by its capability to resolve adjacent bars. Furthermore, spatial linearity can be visually inspected. The phantom is a 60 x 60 x 15 mm$^3$ tungsten block in which slits of 0.6, 0.8, 1.0 and 1.2 mm are machined by wire erosion (see Figure 5.6). The phantom is placed directly on the detector while the $^{68}$Ge source (29 MBq) is placed at 52.5 cm distance. For each of the four phantom quadrants a separate measurement is done by positioning the source in the respective quadrant center as seen in Figure 5.6. This way the entrance angles are more perpendicular and less gamma rays penetrate the thin bars worsening the contrast of the test pattern. Recorded events are filtered with an energy window of 20% and positioned with the MNN algorithm and the neural network. The flood source histograms from Section 5.2.5 are used to normalize for uniformity.

The line profiles are not taken at one discrete position but are summed for each respective quadrant in the direction parallel to the bar pattern. The minima $O_{min}$ and maxima $O_{max}$ are determined in the summed line profile (Figure 5.14), between 0 and 60) to calculate the output modulation $M_{out} = (O_{max} - O_{min})/(O_{max} + O_{min})$. The input modulation $M_{in} = (I_{max} - I_{min})/(I_{max} + I_{min})$ is obtained from Gate simulations. The STL file of the bar phantom is loaded into the simulation software. The detector is modelled in Gate with the same geometry, SiPM pixel size and surface finish as in the presented prototype. More details on simulation parameters can be found in [71]. The positions of the gamma rays absorbed in the crystal are recorded for the four measurement scenarios (source positions $x_1$ to $x_4$ in Figure 5.6 b)). Similar to the experimental analysis the line profiles are then summed for each respective quadrant in the direction parallel to the bar pattern. Then the input modulation $M_{in}$ for all four bar widths is calculated. The simulated $M_{in}$ value is almost constant over the detector but does not include events from Lutetium background. Due to that and since a simulation represents an idealized environment a rather high input modulation value between 0.93 and 0.95 is calculated. For the determination of the MTF it means that the results shown here are rather on the pessimistic side and might be better in reality. Finally, the modulation transfer function (MTF) is calculated for each bar width w

$$MTF(w) = M_{out}(w)/M_{in}(w). \tag{5.1}$$

### 2D resolution improvement by adding DOI layers

For the MNN positioning algorithm the calibration data per position is divided into groups according to the signal's variance. For each group the mean signal is calculated and stored as a reference signal. Since the variance is related to the DOI of the signal we call these groups DOI layers or simply layers. Here the effect of the number of chosen DOI layers on the 2D resolution is evaluated. The acquired events from the bar phantom measurements in 5.2.5 are positioned with reference datasets calculated with different number of layers. For 1, 2, 4, 6, 8, and 10 layers the 2D resolution is compared visually. A quantitative comparison is provided by MTF values (Figure 5.15) that are determined the same way as described in the previous section.

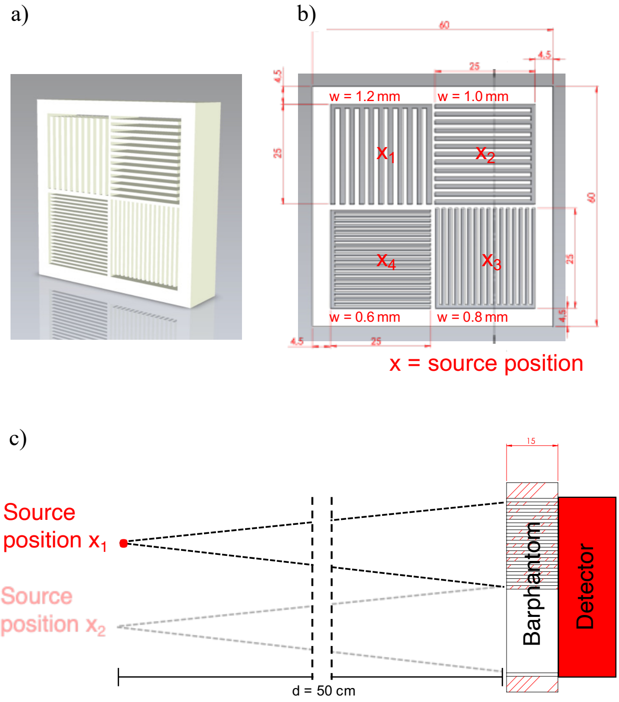

**Figure 5.6:** a) 3D view of the four-quadrant bar phantom. b) Dimensions of bar phantom and source positions $x_1$-$x_4$. c) Side view of the experimental set-up.

## 5.3 Results

### 5.3.1 Spatial resolution estimation

The spatial resolution obtained for the detector calibrated with the 0.6 mm beam is shown in Figure 5.7 for the MNN algorithm and the neural network respectively. For the MNN algorithm a FWHM of 1.17 mm is obtained (Table 7.1). The mean x and y bias is 0.37 mm and the resulting 2D bias is 0.59 mm. For the neural network, a mean and median FWHM of 1.14 mm and 1.10 mm is obtained, respectively. The mean x/y bias is 0.13/0.11 mm and the resulting 2D bias is 0.20 mm. A general degradation is seen towards the edges of the detector. In the detector center 30 x 30 mm$^2$ the mean FWHM value is 1.13 mm for MNN and 1.02 mm for the neural network.

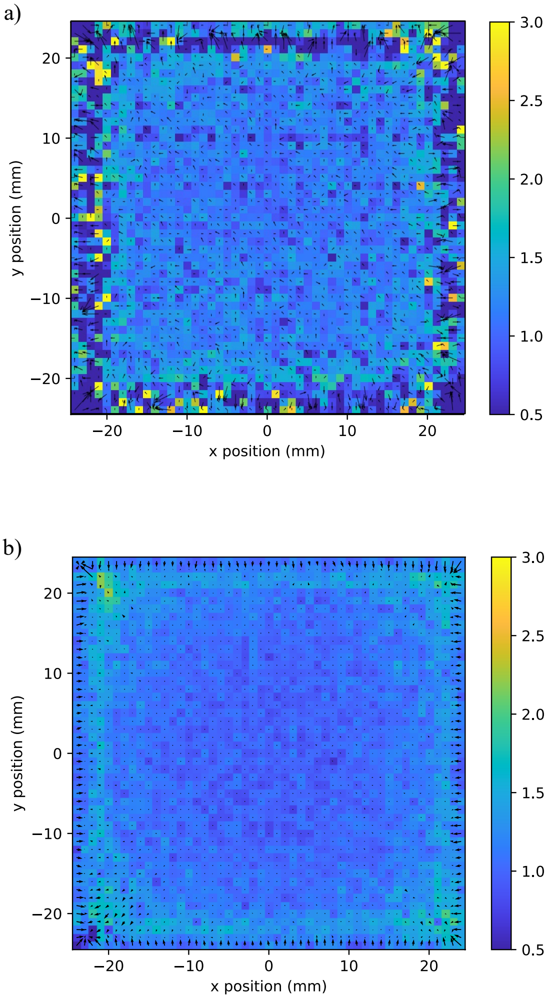

**Figure 5.7:** Spatial resolution as FWHM [mm] for detector with 0.6 mm diameter calibration beam. The bias vectors are indicated as arrows. a) MNN event positioning. b) Neural network positioning.

**Table 5.1:** Performance parameters for calibration of detector with 0.6 mm diameter calibration beam

| | MNN | | Neural network | |
|---|---|---|---|---|
| | 50 x 50 mm$^2$ | 30 x 30 mm$^2$ center | 50 x 50 mm$^2$ | 30 x 30 mm$^2$ center |
| FWHM mean | 1.17 | 1.13 | 1.14 | 1.02 |
| FWHM median | 1.17 | 1.14 | 1.10 | 1.01 |
| Bias x mean | 0.37 | 0.14 | 0.13 | 0.06 |
| Bias y mean | 0.37 | 0.16 | 0.11 | 0.05 |
| 2D Bias | 0.59 | 0.26 | 0.20 | 0.09 |

### 5.3.2 DOI estimation

In Figure 5.8 the relative distribution of the identified DOI layer is presented in red for the two algorithms. As a reference the theoretical distribution that we expect by the attenuation of the crystal is shown as a dotted black line. The result obtained from simulations [71] with the MNN algorithm is shown as a black solid line. For the MNN algorithm an offset of 1-2% can be observed in layer one to four compared to the theoretical curve. The sixth layer contains about 6% more events than expected. The depth distribution obtained from simulations with the same algorithm also shows a significantly higher amount of events positioned in layer 6 than expected from the theoretical distribution. This has been investigated and is explained in the discussion. The neural network fits the theoretical curve with a maximum offset of 0.8%.

### 5.3.3 Energy resolution

The evaluation of the energy resolution per calibration position is shown in Figure 5.9. The energy resolution for the whole detector is 11.03% ± 1.1% and 10.7% ± 0.5% for the detector center (30 x 30 mm$^2$). Degradations of up to 18% can be observed in the top left and right corner regions at 6-7 mm from the crystal edge. The bottom corner region degrades to 14-15%. The energy spectrum includes small amounts of $^{176}$Lu background radiation from the LYSO scintillator which explain the counts above 511 keV in Figure 5.10 [123].

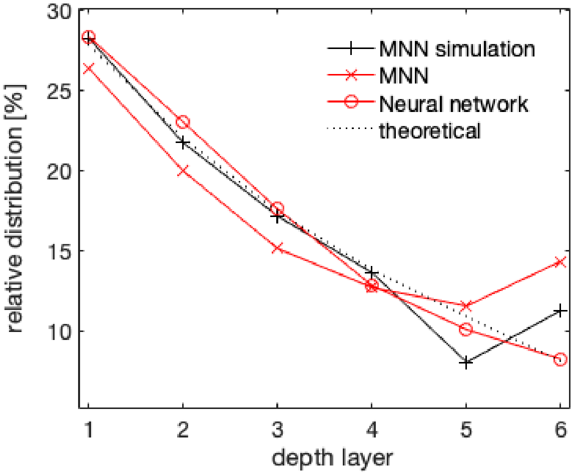

**Figure 5.8:** DOI evaluation. The distribution of events positioned in each layer

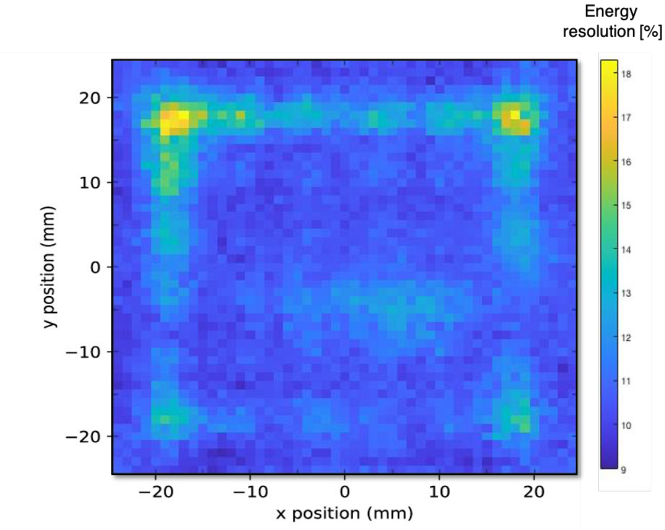

**Figure 5.9:** The mean energy resolution of the detector per calibration position is 11.03%.

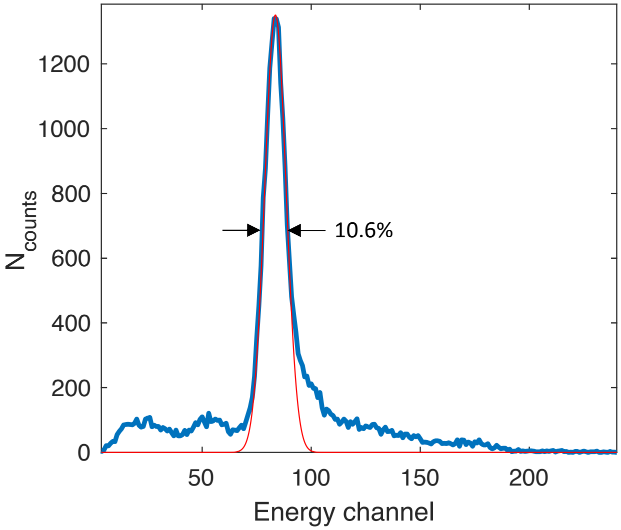

**Figure 5.10:** The energy spectrum at a calibration position in the detector centre with Gaussian fit and energy resolution of 10.6% FWHM.

### 5.3.4 Uniformity

In Figure 5.11 the detector uniformity is shown for the MNN positioning algorithm and the neural network. Both histograms show artefacts related to the underlying 8 x 8 SiPM pixel array. Furthermore, the MNN histogram shows bright hotspots while the neural network histogram shows more wrinkle-like artefacts. A better understanding of the non-uniformities can be obtained by looking at the 2D histograms per DOI layer in Figure 5.12. From left to right, the uniformity can be observed from the crystal top (gamma entrance face) to the readout (SiPM array) side of the detector. Especially in layer 6 the uniformity suffers from the underlying SiPM structure.

### 5.3.5 Bar phantom

In Figure 5.13 the bar patterns can be visually inspected from a) the MNN algorithm and b) the neural network. The bar patterns can be well distinguished for all bar sizes with both algorithms. A more quantitative evaluation is shown in Figure 5.14. On the left the summed line profiles are presented. From these profiles the output modulation

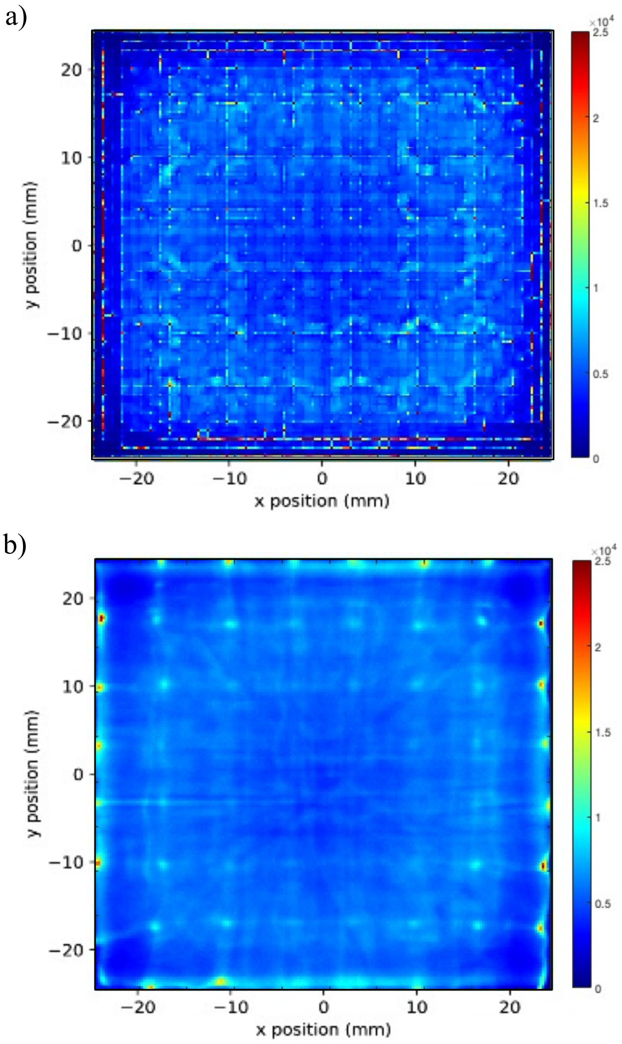

**Figure 5.11:** Detector uniformity. 2D histogram of positioned events from a flood source using a) the MNN positioning algorithm and b) the neural network positioning

$M_{out}$ is calculated. The MTF (Figure 5.14b)) is calculated from $M_{out}$ and the input modulation $M_{in}$ which was obtained from simulations (0.94) . It is given in line pairs per mm. The object contrast for the largest 1.2 mm bars (spatial frequency of 0.8 mm) is 22% and 24% for MNN and neural networks respectively. For the smallest bars of 0.6 mm (spatial frequency of 1.67 $\text{mm}^{-1}$) the object contrast is 2.9% and 5.3%.

### 5.3.6 2D resolution improvement by adding DOI layers

The 2D spatial resolution that is achieved with the MNN algorithm depends amongst other factors on the implementation of DOI layers. In Figure 5.15 the improvement can be seen between not using any DOI layers and a 10 layer DOI implementation. MTF values are stated in the corner of each quadrant. The most substantial improvement for this detector can be seen between layers 1 and 6. Here the MTF values for the largest bar size increase from 7.8% to 21.5% for the smallest bar size the MTF increases from 1.5% to 2.9%. Between 6 to 10 layers the improvement is limited. Here the MTF values for the largest bar size increase from 21.5% to 22.3% for the smallest bar size the MTF increases from 2.9% to 3.6%. For the neural network the 2D resolution does not depend on the number of DOI layers.

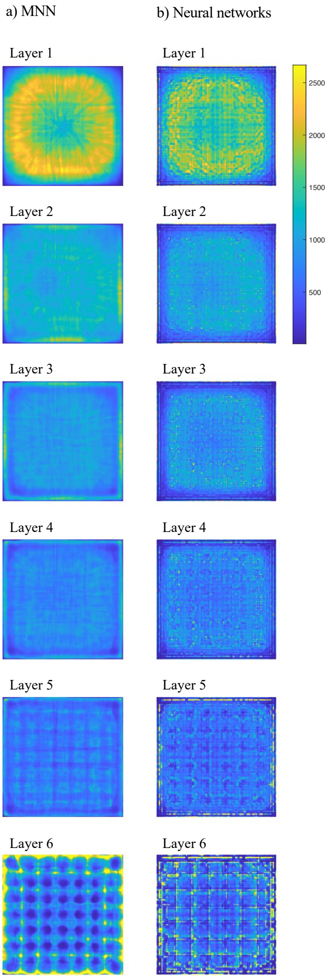

**Figure 5.12:** The detector uniformity presented per DOI layer. Layer 1 is the gamma entrance face and layer 6 is close to the SiPM array. a) 2D histograms for the MNN positioning and b) the neural network positioning.

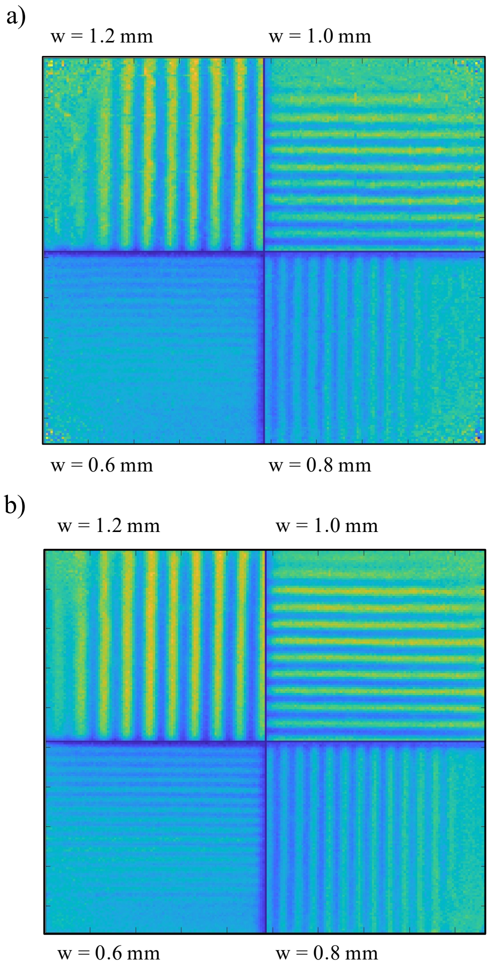

**Figure 5.13:** Bar phantom measurement with a) the MNN positioning and b) the neural network positioning.

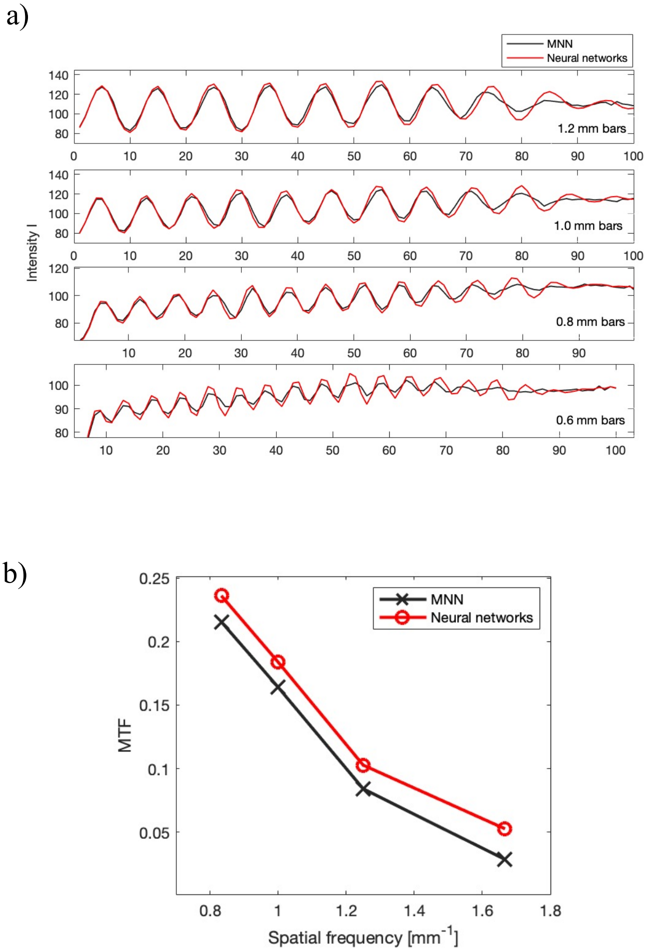

**Figure 5.14:** Evaluation of the bar phantom. a) The summed line profiles of the bar phantom. b) The MTF of the detector.

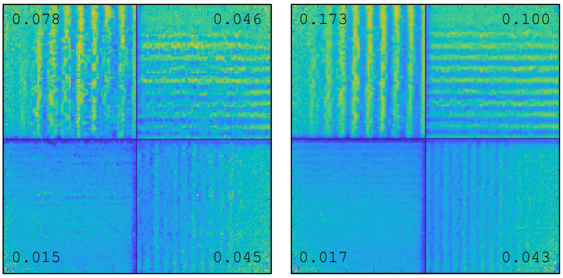
a) no layers

b) 2 layers

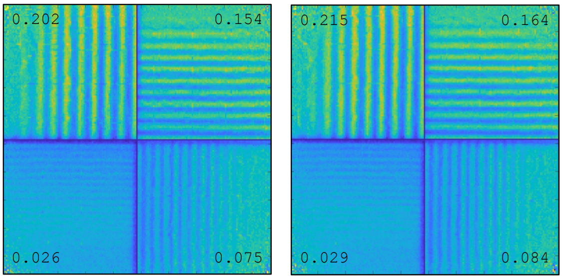
c) 4 layers

d) 6 layers

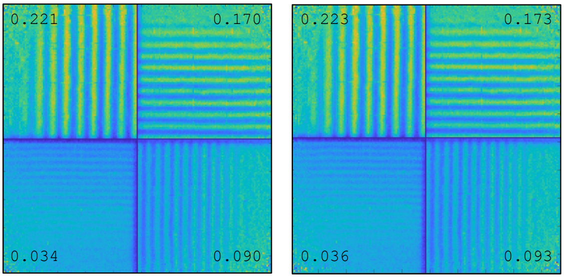
e) 8 layers

f) 10 layers

**Figure 5.15:** Bar phantom measurement with MNN positioning using up to 10 layers a) - f). MTF values are stated in the corner of each quadrant.

## 5.4 Discussion

The mean spatial resolution obtained with neural networks is 1.14 mm FWHM for the whole detector and 1.02 mm in the center excluding the edge region. Therefore, the novel neural network shows superior positioning performance to the MNN positioning algorithm by 2.6% and 9.7% respectively. The degradation towards the edges is typical for these detectors and is due to the scintillation light truncation. The measured PSFs at the edges are broader on the one hand but also not well characterized by Gaussian distributions that are used to calculate the FWHM. As can be seen in the uniformity measurement (Figure 5.11), events at the edges are often positioned at few very specific pixels leading to very good FWHM values. However, they are also connected to larger bias values. Hence, the fitting and resulting FWHM values at the very edges need to be taken with caution and median values or values excluding the edges are more reliable. In Figure 5.7 we see that the neural network shows a more uniform positioning performance especially at the edges compared to the MNN algorithm. The mean 2D bias is 0.59 mm for MNN and 0.2 mm for the neural network. In the center the bias is 0.26 mm and 0.09 mm respectively. Further improvements could be obtained by reading out more SiPM channels, that means 64 channels (8 x 8) when reading out each individual SiPM signal instead of one signal from each row and column (8+8). Another option that can further improve the results is using smaller SiPM pixels e.g. 3 x 3 mm$^2$ pixels in a 16 x 16 array reading out 32 or 256 channels.

In the previous simulation chapter we found that with an MNN approach for 6 x 6 mm$^2$ pixels (as used in this set-up) a single channel readout does not significantly improve spatial resolution. The study also showed that a reduction of the SiPM pixel size to 3 x 3 mm$^2$ can improve the resolution by  20% with summed channel readout and that a single channel readout with 256 channels further improves the resolution by another 7%. The next logical step would therefore be a reduction of the pixel size if better spatial resolution would be desired.

The experimental results do not include a correction to account for the resolution degradation introduced by the calibration beam diameter. The beam at its smallest diameter is here 0.6 mm. The collimator geometry leads to a spread of that beam with increasing distance to the collimator. The final beam width at the light extraction side of the crystal is slightly above 1 mm. Note that the spatial resolution that we measure here depends strongly on the evaluation dataset. If we evaluated this detector with the data of a perfect beam the resolution would still improve significantly. In section 6.2 of the next chapter the influence of the beam diameter on the spatial resolution is covered in a simulation study and experiments with different beam diameters.

The main factors that could cause the performance differences between the two positioning algorithms are discussed in this section. The fraction of Compton scattered events is 60% and has a large influence on the overall positioning performance [100]. The neural network is trained on many individual events while for the MNN database we use the mean of many signals which acts like a filter for PSFs of scattered events. The positioning of scattered events might therefore be improved with the neural networks. The output of the MNN algorithm is a discrete position depending on the degree of interpolation that is applied. The neural network on the contrary is able to provide continuous coordinates as an output. However, it is also prone to overfitting on the discrete calibration positions. Therefore, an additional dataset with signals of intermediate positions is needed to cross-check for overfitting in the training process. In terms of timing the neural network takes more time to be trained but once the training is finished positioning can be accomplished much faster. The MNN algorithm is comparing each event to the complete reference dataset which is computationally more intensive. This increases with higher degrees of interpolation and with the number of implemented DOI layers.

Besides very good intrinsic spatial resolution, DOI estimation is an attractive feature of monolithic detectors. The variance of the LSF gives a direct measure of the DOI and can be easily extracted from the measured signal. However, with wide (rather than thick) monolithic crystals it is very difficult to quantify DOI performance. Obtaining depth dependent data from an experimental set-up e.g. with an irradiation from the side has two main drawbacks. Firstly, the fact that most events will be captured at the very edge of the crystal and secondly, the Compton scatter direction is dependent on the incident angle of the gamma photon thus a side irradiation changes the measured light distributions for scattered events which are more than half of the events. Therefore, we compare the number of events in each depth-layer with (i) theoretically calculated numbers and (ii) simulated data, where the real DOI of the event is known. For MNN the overall DOI distribution is similar to what we expect but there is a large number of events in the sixth layer (close to the readout array). This is related to the mispositioning of Compton scattered events when the actual photoelectric effect occurs deeper inside the crystal than the first interaction. This was previously shown in simulations. An implementation in neural networks with the variance as a measure of the depth shows that neural networks on the contrary are able to position scattered events more reliably. Ideally DOI studies should be linked to simulated data since this is the most accurate way to obtain ground truth data.

The measured energy resolution for the whole detector is 11.03%. The major degradations in the corner regions could be linked to the crystal, crystal finish or reflector. In separate experiments we turned the crystal while the rest of the set-up stayed as it is. The degradation could still be linked to the specific corner of the scintillator. Experiments using other crystals showed also a degradation in the corners but with different emphasis. Thus, for more uniform and better energy resolution towards the corners the crystal and/or reflector quality should be examined.

The uniformity of the detector is clearly influenced by the underlying 8 x 8 SiPM pixel grid (Figure 5.11). When most optical photons are detected by a single SiPM pixel the algorithms are not able to position the event more accurately than in the center of that pixel. In Figure 5.12 the origin of the artefacts becomes more clear by looking at the uniformity as a function of the estimated interaction depth of the photons. Especially towards the SiPM array in layer 5 and 6 uniformity starts to degrade. An improvement could be achieved by using smaller SiPMs or a light guide. Important to be aware of is that for the neural network a uniformity measurement is very useful to check for overfitting. During the training the overall positioning performance improves uniformly over the whole detector until the performance at the discrete calibration positions keeps improving while the other positions start degrading. At that point the network is overfitting and detector performance will become non-uniform. In the uniformity histogram more events would be drawn towards the discrete 49 x 49 calibration grid forming a grid of hot spots. This effect is not observed here proving limited or no overfitting is present.

The bar phantom measurement gives a visual impression on the detector resolution over the complete field of view. The neural network can distinguish bars down to 0.6 mm with >5% contrast determined by the MTFs while the MNN algorithm is just below the 5% mark. The FWHM value is calculated as the smallest resolvable bar times 1.4 - 2

[5]. Thus the bar phantom measurement shows a detector resolution of 0.84 - 1.2 mm FWHM for neural networks and is in the range of what was evaluated with the PSFs. Note that for example in the bottom left quadrant the bars can be distinguished all the way to the left edge while they cannot be distinguished towards the bottom edge. This is due to the source position and angle of the gamma rays penetrating the bars. If a more perpendicular irradiation (and a flood source instead of a point source) could be provided the resolution would improve towards the bottom edge as well.

Both algorithms show similar spatial resolution values (0.1 mm difference). However, the artificial neural network provided more uniform performance over the full detector and smaller positioning bias. Furthermore, the DOI performance was improved with neural networks mainly due to improved positioning of scattered events. The bar phantom measurement provides additional support of the determined detector performance and spatial resolution at the detector centre, edges and corners. The detector resolution using neural networks is 1.13 mm FWHM over the whole detector and 1.02 mm FWHM without the edges. This is expectedly exceeding the resolution of PET detectors in the field that have a greater thickness than 16 mm [79] [82, 124]. In a recent publication of Gonzalez-Montoro [82] a remarkable detector spatial resolution of 0.9 mm FWHM is reported with a only slightly thinner crystal of 15 mm thickness. A notable difference is that the spatial resolution presented in our work is not corrected for the beam source diameter. In Gonzalez-Montoro [82] a great effort is done to isolate the source size from the measured FWHM values leading to a better estimate of the intrinsic spatial resolution. Other detectors that have better spatial resolution are significantly thinner such as [79] with 1.1 mm spatial resolution at 10 mm thickness or [81] with 0.76 mm spatial resolution at 8 mm thickness.

## 5.5 Conclusion

In this chapter the detector prototype construction, calibration and performance evaluation is covered. We presented a monolithic detector design aiming to serve high-resolution clinical PET systems while maintaining high sensitivity. The targeted detector resolution of 1.3 mm intrinsic FWHM needed to reach a 2 mm resolution on system level (with bore diameter of 60-80 cm) was exceeded with a MNN algorithm and 1.13 mm FWHM, as well as with a neural network achieving 1.02 mm FWHM. The 6-layer DOI positioning will also result in a uniform system spatial resolution over the full FOV. In the next chapter simulations and experiments are used to identify and analyse the most important spatial resolution degrading factors.

# 6

# Main degrading factors on spatial resolution

## 6.1 Introduction

In this chapter we identify and analyse the factors that have a degrading effect on the detector spatial resolution and discuss how they can be addressed. In the previous chapters we investigated the performance of a simulated detector under idealized conditions and the prototype detector in the lab. With the combination of simulations and experiments we are able to understand the impact of factors that are otherwise difficult to investigate and learn how to further improve future detector performance. Here we focus on five factors:
*Collimator beam size.* In the experimental set-up a narrow calibration beam is irradiating the detector at known 2D positions to collect the signal of reference events. These reference events are then used to train the positioning algorithms. However, the beam diameter has the same magnitude as the resolution we want to obtain. The first section therefore deals with the impact the finite calibration beam diameter has on the obtainable resolution.
*Compton scattered events.* Many of the gamma particles that are detected in a PET detector do not directly deposit their full energy in the detector but first undergo one or multiple Compton scatter interactions. The energy deposition at different locations results in an altered light distribution that is detected by the photodetectors and has an effect on the spatial resolution. In the second section the magnitude of this effect is analysed using simulations.
*Photon detection efficiency (PDE).* To collect the optical scintillation

light, photodetectors are coupled to the crystal. These devices cannot collect all impinging photons because they have a limited PDE. The lower the PDE the more noise is present in the measured signals. In the third section we simulate different PDEs and investigate the effect on spatial resolution.
The last two factors, $^{176}$Lu background and collimator leak radiation, are combined in one section since they both contribute to the background signal.
*$^{176}$Lu background.* During the calibration of the detector in singles mode one has to deal with background radiation that disturbs the quality of the measurements. The most widely used scintillator material in PET detectors is LSO or LYSO, both lutetium based materials. Lutetium itself contains small amounts of radioactive $^{176}$Lu that interfere with the 511 keV energy peak of interest contaminating the measured signal. In this section we analyse the $^{176}$Lu spectrum.
*Importance of collimator design.* Furthermore the calibration source that is encapsulated in a collimator made from tungsten ideally does not allow any gamma rays to exit the housing except for the tiny beam. An imperfect collimator design does allow gamma rays to exit the collimator at undesired locations. In this section we analyse the collimator leak radiation.
Finally, we present how to efficiently extract the gamma signals from the $^{176}$Lu background and collimator leak radiation.
The work presented in this chapter resulted in three conference contributions [125–127].

## 6.2 Influence of collimator beam size

### 6.2.1 Introduction

To precisely determine the position of a gamma interaction inside a monolithic detector, a fine calibration beam is used to obtain reference detector signals from known x,y-positions. These reference events and their known position can then be used to create reference data LUTs for nearest neighbour positioning or to train neural network algorithms. In a typical calibration set-up the calibration source is encapsulated inside a collimator (Figure 6.1). Due to the machining of the collimator the resulting calibration beam is not ideal, but has a certain diameter

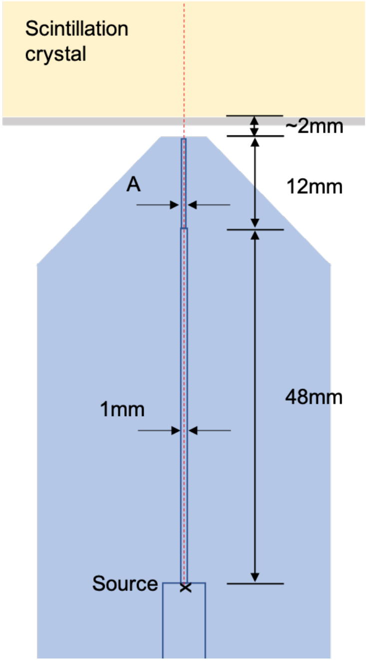

**Figure 6.1:** A drawing of the collimator. The encapsulated radioactive source is placed inside the tungsten collimator. The beam is first collimated to 1 mm and finally to a diameter A (0.6 or 1 mm). Between the collimator and the housing is another ~ 1 mm air gap to avoid a clash/interference during the automated movement between different calibration positions.

and beam spread. This introduces a bias in the ground truth position label. Here we examine the calibration beam size diameter as a potential source of resolution degradation to understand and ultimately improve the detector performance. First, we use optical simulations to produce a perfect calibration beam and compare the resolution to a realistic beam source. Second, we calibrate our prototype monolithic detector with a collimator of 0.6 mm and 1.0 mm diameter, respectively. Finally, we use deconvolution to estimate the spatial resolution without the impact of the remaining source diameter present in the prototype calibration.

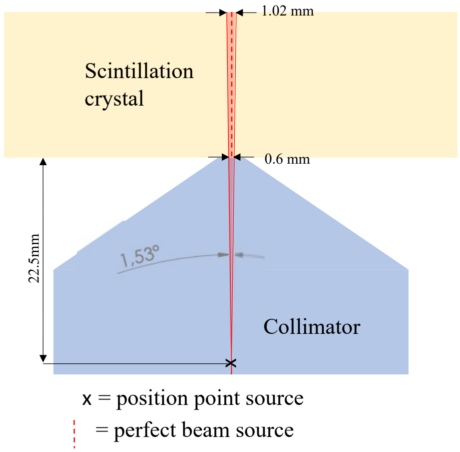

**Figure 6.2:** The collimated beam is simulated as a point source at 22.5 mm distance from the detector with an opening angle of 1.53°.

## 6.2.2 Materials and methods

### Simulation

The simulation is performed as explained in Chapter 4. For this study we choose the same configuration as in the prototype, i.e. 8 x 8 array of 6 x 6 $mm^2$ SiPMs with a 16 (8+8) channel rows and column summed readout. The detector is calibrated in 1 mm steps, first with a perfect perpendicular and mono-energetic 511 keV pencil beam source as in Chapter 4, then with a source that models a 0.6 mm diameter collimator. In the simulation this is done by a point source with an opening angle of 1.53° at a distance of 22.5 mm from the crystal surface (Figure 6.2). For both calibration datasets the nearest neighbour positioning $\mu$ maps are calculated. The mean and median FWHM values of the positioned events are evaluated for the full detector and the detector 30 x 30 $mm^2$ center.

Four simulation scenarios are tested:

- Detector calibration with perfect beam (0.0 mm), evaluation with same beam size.
- Detector calibration with perfect beam (0.0 mm), evaluation with 0.6 mm beam.

- Detector calibration with 0.6 mm beam, evaluation with same beam size.
- Detector calibration with 0.6 mm beam, evaluation with perfect beam.

### Experimental

The prototype detector described in Chapter 5 is calibrated with a collimated $^{68}$Ge source (69 MBq) placed in a tungsten collimator with diameter A of 0.6 mm and 1 mm, respectively (Figure 6.4). Calibration data is acquired in 1 mm steps for 70 s per position. In Figure 6.3 events from the two different beam sizes are positioned with simple Anger logic. For both calibration datasets (0.6 mm and 1 mm calibration beam) the nearest neighbour positioning mu maps are calculated. The mean and median FWHM values of the positioned events are evaluated for the full detector and the detector 30 x 30 mm$^2$ center.

Four experimental scenarios are tested:

- Detector calibration with 0.6 mm beam, evaluation with same beam size.
- Detector calibration with 0.6 mm beam, evaluation with 1 mm beam.
- Detector calibration with 1.0 mm beam, evaluation with same beam size.
- Detector calibration with 1.0 mm beam, evaluation with 0.6 mm beam.

### Estimation of real spatial resolution

To isolate the finite collimator beam size from the determined FWHM values we apply a convolution of the beam profile. The beam profile is assumed to be a rectangular function $r$ of the width $w$ of the collimator beam. More likely the beam width is slightly broader since (as described before) (i) there is a small gap between the crystal and collimator and (ii) the beam has a spread. However, for simplicity we chose a rather

pessimistic value. The rectangular function to represent the beam r(w) has a width of $w = 0.1 - 1.4$ mm and height of $h = 1$.
For Gaussian functions g(x) with FWHM values of 0 to 1.4 mm we can calculate

$$g(x) = \frac{1}{\sigma\sqrt{2\pi}} e^{-(x-\mu)^2 / 2\sigma^2} \tag{6.1}$$

with mean $\mu = 0$ and the standard deviation $\sigma$

$$\sigma = \frac{FWHM}{2 * sqrt(2 * log(2))} \tag{6.2}$$

For each Gaussian g(x) and beam profile r(w) a convolution

$$g_{conv}(x) = r * g = \int g(\tau) r(k - \tau) d\tau \tag{6.3}$$

is performed with Matlab *conv* function. Finally, the FWHM value of the resulting distribution $g_{conv}(x)$ is calculated.

### 6.2.3 Results

#### Simulation

When the detector is evaluated with data from a perfect calibration beam, the detector calibration with the same source leads to a mean spatial resolution of 0.81 mm FWHM (Table 6.1). When excluding the edges and only looking at the central 30 x 30 mm$^2$ the mean spatial resolution is 0.61 mm FWHM. The values excluding the edges are stated in brackets from now on. The detector calibration with a perfect calibration source but tested with data from the source with a diameter of 0.6 mm leads to a spatial resolution of 1.10 (0.88) mm FWHM. The calibration with a collimated beam of 0.6 mm diameter leads to a spatial resolution of 1.06 (0.88) mm FWHM when tested with data from the same source. When the detector is again calibrated with a 0.6 mm source but the test data originates from a perfect beam the spatial resolution improves to 0.78 (0.60) mm FWHM. The median FWHM values are stated in Table 6.2. For calibrations with both beam sizes a similar resolution could be obtained when the evaluation was done with data from the same source diameter. In Figure 6.4 the histograms of the positioned events

**Table 6.1:** Mean FWHM values for the full detector 50 x 50 mm$^2$ (and in brackets for the detector center 30 x 30 mm$^2$) dependent on the collimator beam size in the calibration data set and evaluation data set.

| mean FWHM [mm] | | Evaluation | |
|---|---|---|---|
| | | 0.0 mm | 0.6 mm |
| Calibration | 0.0 mm | 0.81 (0.61) | 1.10 (0.88) |
| | 0.6 mm | 0.78 (0.60) | 1.06 (0.88) |

**Table 6.2:** Median FWHM values for the full detector 50 x 50 mm$^2$ (and in brackets for the detector center 30 x 30 mm$^2$) dependent on the collimator beam size in the calibration data set and evaluation data set.

| median FWHM [mm] | | Evaluation | |
|---|---|---|---|
| | | 0.0 mm | 0.6 mm |
| Calibration | 0.0 mm | 0.62 (0.56) | 0.92 (0.85) |
| | 0.6 mm | 0.62 (0.55) | 0.93 (0.85) |

from the different scenarios can be visually inspected. The resolution in the first column (evaluation with 0.0 mm 'perfect' beam) is superior to the resolution in the second column (evaluation with 0.6 mm 'realistic' beam) independent of the calibration beam size.

### Experimental

The prototype detector calibration with the smaller 0.6 mm calibration source leads to a mean spatial resolution of 1.17 (1.13) mm FWHM (Table 6.3) when the detector is evaluated with data from the same source. The detector calibration with the 0.6 mm calibration source but tested with data from the source with a diameter of 1.0 mm leads to a spatial resolution of 1.31 (1.30) mm FWHM. The calibration with a collimated beam of 1.0 mm diameter beam leads to a spatial resolution of 1.33 (1.31) mm FWHM when tested with data from the same source. When the detector is again calibrated with a 1.0 mm source but the test data originates from a 0.6 mm beam the spatial resolution improves to 1.17 (1.16) mm FWHM. The median FWHM values are stated in Table 6.4. Similar to the results from the simulated datasets we see that the beam size in the evaluation dataset has a large influence on the determined spatial resolution while the beam size in the calibration

**Table 6.3:** Mean FWHM values for the full detector 50 x 50 mm$^2$ (and in brackets for the detector center 30 x 30 mm$^2$) dependent on the collimator beam size in the calibration data set and evaluation data set.

| mean FWHM [mm] | | Evaluation | |
|---|---|---|---|
| | | 0.6 mm | 1.0 mm |
| Calibration | 0.6 mm | 1.17 (1.13) | 1.31 (1.30) |
| | 1.0 mm | 1.17 (1.16) | 1.33 (1.31) |

**Table 6.4:** Median FWHM values for the full detector 50 x 50 mm$^2$ (and in brackets for the detector center 30 x 30 mm$^2$) dependent on the collimator beam size in the calibration data set and evaluation data set.

| median FWHM [mm] | | Evaluation | |
|---|---|---|---|
| | | 0.6 mm | 1.0 mm |
| Calibration | 0.6 mm | 1.17 (1.14) | 1.30 (1.32) |
| | 1.0 mm | 1.21 (1.16) | 1.34 (1.31) |

dataset results in comparable resolutions.

### Estimation of real spatial resolution

In Figure 6.5 the convolution of Gaussian functions with rectangular functions are shown in terms of their FWHM values. On the x-axis the FWHM values of Gaussian distributions are plotted. On the y-axis the FWHM values of the Gaussian distributions are plotted after the convolution with the rectangular function. The rectangular function represents the beam width and is represented in different colors. In our experiments we used beam widths of 0.6 mm and 1 mm which are the purple and green line respectively. If one now measured a certain FWHM with a collimated beam of 0.6 mm width the graph can indicate the spatial resolution without the influence of the beam width. Specifically for our detector we measured a FWHM value of 1.13 mm with a beam diameter of 0.6 mm and a FWHM value of 1.30 mm with a beam diameter of 1.0 mm. If we draw a horizontal line from the respective measured spatial resolution to the according line with the used beam width, we can read the spatial resolution isolated from the effect of the beam width on the x-axis. For both beam width the measurements indicate that the spatial resolution if it was measured with a perfect beam would be about 1.05 mm (see dashed black lines in Figure 6.5).

### 6.2.4 Discussion and conclusion

First, the influence of the calibration beam was evaluated for simulated data. We used (i) a perfect beam with a negligible beam diameter and (ii) a beam that simulates a realistic collimated beam of 0.6 mm diameter including an opening angle leading to a spread of the beam. The detector was calibrated with both beam sizes and then evaluated on both data sets. For clarity, the calibration data consist of events that were acquired per calibration position and then the mean reference signals were stored in LUTs. We found that the calibration with both beam sizes leads to a similar mean detector spatial resolution of 0.6 mm FWHM excluding edges (and 0.8 mm FWHM over the whole detector) when evaluated with the 'perfect' beam dataset. However, the resolution significantly degrades when the detectors are evaluated with the 0.6 mm beam. In simulations the ideal calibration beam can be provided, but in an experimental set-up it is more difficult especially when using mechanically collimated beams.

In a second step the same tests were done experimentally using the prototype detector. Here we used (i) a collimator with a 0.6 mm beam and (ii) a collimator with a 1 mm beam. The detector was calibrated with both beam sizes and then evaluated on both data sets. The calibration with both beam sizes lead to 1.17 mm FWHM over the whole detector when evaluated on the 0.6 mm beam diameter data. When the evaluation data from the larger beam diameter is used the resolution degrades to about 1.3 mm FWHM.

In summary, we showed that for the calibration of the detector, the beam diameter of up to 1 mm does not have a large influence on the obtainable resolution. A calibration with even larger beam diameters would pose several advantages, (i) more events can be acquired in less time or a source with lower activity can be used for calibration, (ii) improved SNR with respect to the background radiation (cfr. Section 6.5), and (iii) easier (cheaper) collimator manufacturing. The degree to which the collimator beam size could be increased before a degradation of the resolution is encountered, could be investigated in simulations.

Two important conclusions can be made: 1. a smaller calibration beam does not necessarily lead to better spatial resolution and 2. to demonstrate the actual detector spatial resolution it is important to provide data from a beam as small as possible. Therefore the (measured) resolution would still improve if ground truth data (with a negligible beam diameter) would be available for testing our prototype detector in the lab. However that does not change the actual performance that the detector will have on system level.

Using a deconvolution of the beam width we estimate the detector spatial resolution we could get with a perfect beam. For a 0.6 mm beam the resolution would improve by 7% to 1.05 mm. If the test was acquired by a 1 mm beam the introduced degradation by the beam size is already 18%. This method is a good indicator of the impact of the beam width on the obtained resolution, however, more advanced methods to extract the beam diameter influence from the measured source profile have been proposed in literature. In Maas et al. [128] a model was developed to correct for the finite diameter of the annihilation photon beam by a PSF model consisting of two convolved component, one for the spatial distribution of the annihilation photon energy deposition and the second for the influences of statistical signal fluctuations and electronic noise. In Gonzalez-Montoro [82] an isolation of the beam source was achieved by a theoretical model to fit the measured light distributions. The model is based on a convolution of a Gaussian shaped distribution for the detector contribution and a modified Lorentzian distribution to account for the collimated source profile.

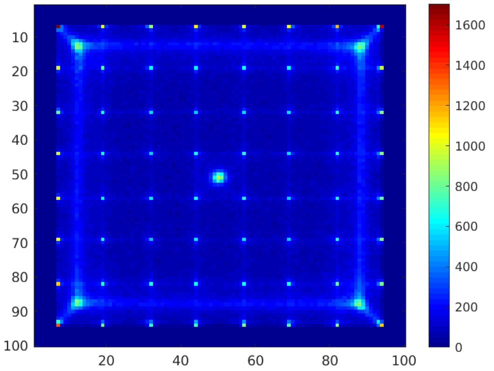

(a) 0.6 mm

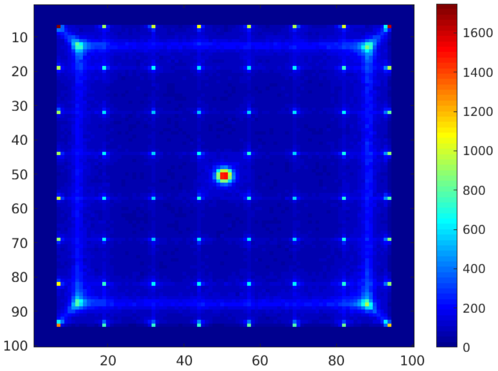

(b) 1.0 mm

**Figure 6.3:** Anger positioned events from 2 different collimators at a central calibration position in the detector center.

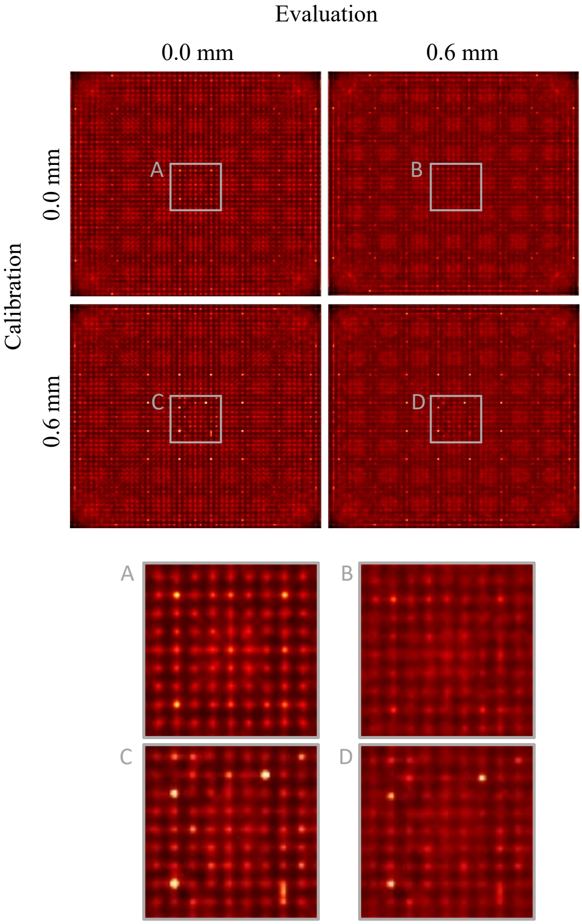

**Figure 6.4:** Histogram of positioned events dependent on the calibration data collimation beam and evaluation data collimation beam. A-B show a zoomed area of the respective detector center.

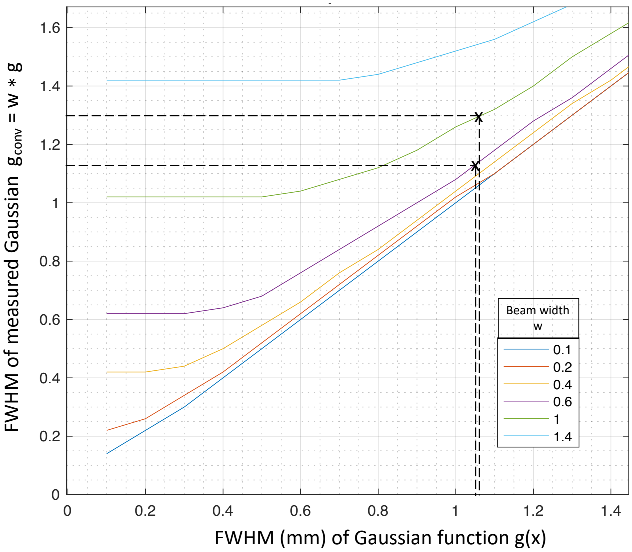

**Figure 6.5:** The FWHM of the measured distribution g(x) is plotted on the y-axis. The colors indicate the width of the rectangular function r(w). The resulting FWHM values of the Gaussian w(k) after a deconvolution of g(x) and r(w).

## 6.3 Influence of Compton scattered events

### 6.3.1 Introduction

The gamma photon interaction inside a scintillator can be a single photoelectric interaction or involve multiple Compton interactions. In Figure 6.6 multiple scenarios are presented. In (1) the gamma directly undergoes a photoelectric interaction and deposits all its energy at the interaction position. In (2) the gamma photon first undergoes a Compton scatter, depositing part of its energy at this location. It then travels further and undergoes a photoelectric interaction depositing its remaining energy. In (3) the gamma photon undergoes two Compton interactions and in (4) three Compton interactions before the photoelectric interaction occurs. In (5) the Compton scatter occurs close to the crystal edge, subsequently the gamma exits the crystal and does not deposit all its energy inside the detector. This event can be filtered by an energy window if the energy loss is big enough. The fraction of Compton scattered events in monolithic crystals depends on the detector material and energy. For LYSO the so called photofraction is $\approx 33\%$. The thickness of the crystal also has an effect on the number of Compton scattered events in a dataset. This is because the chance that the scattered photon is captured and therefore cannot be discarded by the applied energy window is increasing with crystal thickness. The scattering alters the measured light distribution and therefore has an influence on the determined interaction position. In this section we first analyse the number of Compton scattered events at different detector positions and their mean travel paths and second we evaluate the impact of Compton scatter on the obtainable spatial resolution.

### 6.3.2 Materials and methods

The simulation is performed as explained in Chapter 4. For this study we use the data from an 8 x 8 array of 6 x 6 mm$^2$ SiPMs. The signal from 64 SiPM pixels is combined to 16 (8+8) channels by summing rows and columns. The detector is calibrated in 1 mm steps, with a perfect perpendicular and mono-energetic 511 keV pencil beam source as in Chapter 4. The calibration and evaluation data is energy-filtered i.e. scattered events that have not deposited their full energy inside the crystal are discarded. The information on the gamma 3D interaction

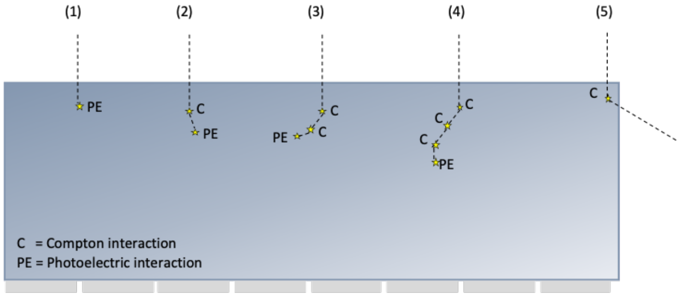

**Figure 6.6:** Interaction scenarios: (1) photoelectric interaction, (2) Compton scatter + photoelectric interaction, (3) two and (4) three Compton interactions + photoelectric interaction, (5) Compton interaction before gamma exits crystal.

position and interaction process are saved from the simulations. The nearest neighbour positioning mu maps are calculated as described in Section 4.2.2.

### Compton statistics

From the energy-filtered dataset the number of photoelectric and Compton interactions per event is determined for three calibration positions: (i) in the very center of the detector, (ii) 1 mm from the corner of the crystal and (iii) 1 mm from the edge of the crystal in between two corners.
Further the scatter distances between the first interaction and the second interaction are determined in x,y, and z direction for the center position. This is either the scatter distance between a Compton and a photoelectric interaction or between two Compton interactions.

### Simulation study on Compton scatter

2000 events are positioned for each calibration position across the whole detector for three scenarios. The evaluation data includes:

- scattered and non-scattered events.
- only events that have not scattered.
- only events that scattered once or multiple times.

**Table 6.5:** Scatter distances [mm] between the first and second gamma interaction and the first and third gamma interaction.

| | scatter distance between 1st and 2nd interaction | | scatter distance between 1st and 3rd interaction | |
|---|---|---|---|---|
| | mean | median | mean | median |
| x - direction | 2.21 | 1.19 | 3.36 | 2.18 |
| y - direction | 2.06 | 1.12 | 3.24 | 2.11 |
| z - direction | 2.67 | 1.68 | 3.43 | 2.39 |

The mean and median FWHM values of the positioned events are evaluated for the full detector and the 30 x 30 $mm^2$ center.

### 6.3.3 Results

#### Compton statistics

When irradiating the crystal with a perpendicular beam at the center of the detector the number of 511 keV gammas that are undergoing an immediate photoelectric interaction is 39.7% (Figure 6.7). 37.9% of the gammas undergo one Compton interaction before releasing their rest energy with a photoelectric interaction. The rest of the gammas, 22.4%, undergo at least two and up to six Compton interactions. The distribution shifts when evaluating at the very edge of the crystal. In that situation the number of 511 keV gammas that are immediately undergoing a photoelectric interaction is 50.8% while 33% of the gammas undergo one Compton interaction. At the corner this effect is enhanced to 58% without Compton interactions. At the edges and corners a gamma particle is more likely to exit the crystal after scattering, resulting in a lower energy deposition. This allows us to exclude these events from the dataset and explains the higher fraction of non-scattered events in Figure 6.7.

The mean scatter distance (Figure 6.8) between the first Compton interaction and next interaction (either Compton or photoelectric) is 2.21 and 2.06 mm in x and y direction, respectively (Table 6.5). The mean scatter distance in z direction is 2.67 mm. The mean distance between the first Compton interaction and the third interaction increases to 3.36 mm in x, 3.24 mm in y and 3.43 mm in z direction.

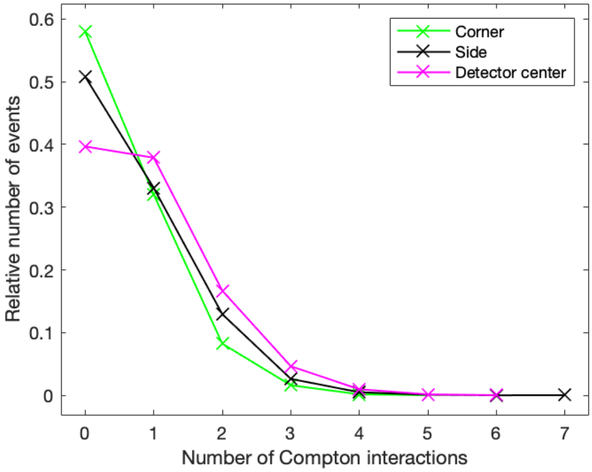

**Figure 6.7:** Relative number of Compton interactions per gamma event for three different calibration positions. This graph only includes events that fall into the energy window that means they have deposited their full energy in the crystal. ’0’ Compton interactions means that the gamma event did not scatter.

### Simulation study on Compton scatter

The determined mean spatial resolution for the full detector including scattered and non-scattered events is 0.81 mm FWHM for the full detector and 0.61 mm excluding the edges (Table 6.6). To determine the effect of Compton scattering, only the non-scattered events are positioned leading to a mean spatial resolution of 0.71 mm and 0.56 mm for the center. On the contrary, the evaluation of only scattered events results in FWHM values of 1.20 mm and 0.92 mm for the center. In Figure 6.9 the effect of Compton scatter on the positioning performance can be visually evaluated.

## 6.3.4 Discussion and conclusion

In this section the positioning performance is evaluated with respect to the presence of Compton scattered interactions in the crystal. Events that directly undergo a photoelectric interaction can be positioned more accurately. The gamma energy is converted into scintillation light at one single position which simplifies the corresponding light spread function and the positioning with the MNN algorithm. When only photoelectric

**Table 6.6:** Mean and median FWHM values for the full detector 50 x 50 mm$^2$ and the detector center 30 x 30 mm$^2$ for a) scattered and non-scattered events b) only non-scattered events and c) only scattered events.

| | FWHM [mm] | full detector 50 x 50 mm$^2$ | center 30 x 30 mm$^2$ |
|---|---|---|---|
| a) | mean | 0.81 | 0.61 |
| | median | 0.62 | 0.56 |
| b) | mean | 0.71 | 0.56 |
| | median | 0.56 | 0.50 |
| c) | mean | 1.20 | 0.92 |
| | median | 1.04 | 0.89 |

events are present the resolution is 12% better over the full detector and 9% excluding the edges (compared to scatter+non-scatter). The scattered events can be scattered once or multiple times in the detector. The energy deposition occurs subsequently at multiple locations. The effect on the light spread function that is measured can be small when the final photoelectric interaction is in very close proximity and occurs in the line of the irradiation beam with only a small lateral shift with respect to the incidence angle. However, the light distribution of many scattered events is altered, leading to a shift of the peak of the light distribution. This negatively affects the positioning performance of the MNN algorithm. When only positioning scattered events the FWHM degrades by 32.5% and 33.7% excluding the edges (compared to scatter+non-scatter). When positioning all events (i.e. scatter+non-scatter) the differences in FWHM compared to only non-scatter is 9-12%, however, scattered events contribute especially to the tails of the PSFs rather than affecting the FWHM values [100]. Therefore it is of great relevance to be able to position scattered events more accurately. In collaboration with Decuyper et al. [129] a scatter determination network was trained on simulated data to detect the distance events have scattered. Those events that exceed a certain scatter threshold can then be removed from the dataset and improve the positioning accuracy of the remaining events. In Section 7.3 of the next chapter this scatter determination network trained on simulation data is applied to our prototype detector.

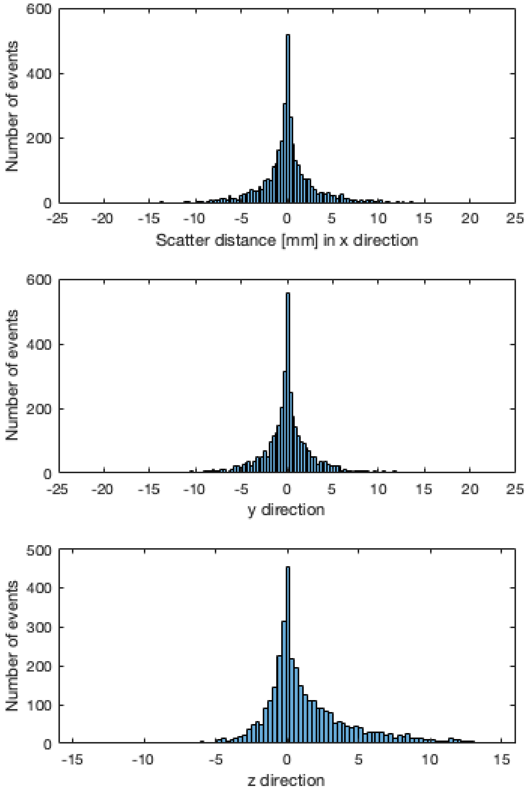

**Figure 6.8:** Histogram of the gamma scatter distance [mm] in x, y and z direction. This histogram does not include non-scattered events. The z - direction considers forward scatter from 0 to 16 mm as well as backward scatter from 0 to -16 mm.

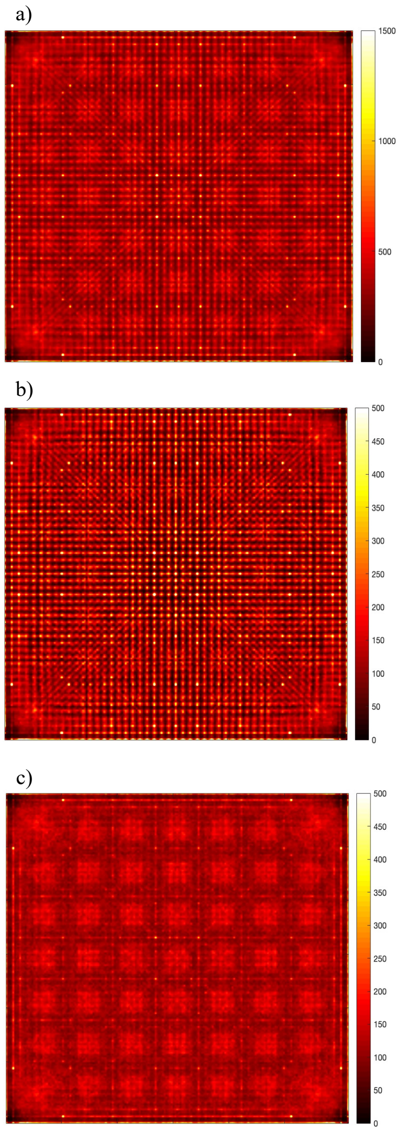

**Figure 6.9:** Histograms of positioned events a) scattered and non-scattered events b) only non-scattered events and c) only scattered events. a) is the combination of b) and c).

## 6.4 Photon detection efficiency (PDE)

### 6.4.1 Introduction

The scintillation light generated by the high energy gamma ray is typically extracted on one side of the crystal block by a photodetector array. The most common type of photodetectors are SiPMs. The sensitivity, or the probability that an impinging optical photon is detected by a SiPM, is called the PDE. As discussed in 3.5.2, the PDE is dependent on the quantum efficiency of silicon, the applied voltage and the fill factor. Currently SiPMs have PDEs up to 60% [10]. In Chapter 4 the PDEs of 35%, 50% and 75% were simulated. In this section we study in more detail the influence of the noise introduced by lower PDEs.

### 6.4.2 Materials and methods

The GATE simulations performed in Chapter 4 initially use a detection efficiency of 75%. According to the binomial selection theorem, a binomial selection of a Poisson distribution yields a Poisson distribution, which can be fully characterized by its mean [130]. In a post-processing step, the photons per pixel can thus be re-sampled to obtain a PDE of 50% and 35%, respectively. The 2D resolution is determined for PDEs of 35% and 50% and compared to 75% PDE. The dependency between photon wavelength and detection efficiency is not modelled. The spatial resolution is obtained by positioning 2,000 events per calibration position in the central 10 x 10 $\text{mm}^2$ of the detector. The PSFs are measured in terms of FWHM (Gaussian fit) in horizontal and vertical direction and presented as an average of all profiles. The positioning bias is defined as the distance between the real X, Y - position and the calculated position. The FWHM, the mean positioning bias and the median bias for all events are calculated for pixel sizes 3 mm and 6 mm, with individual and combined channel readout, and with PDEs of 35%, 50% and 75%.

### 6.4.3 Results

In Table 6.7 the determined spatial resolution is presented dependent on three PDE values and different SiPM readout schemes. For a 16 channel - combined row and column - readout the FWHM worsens from 0.48 mm

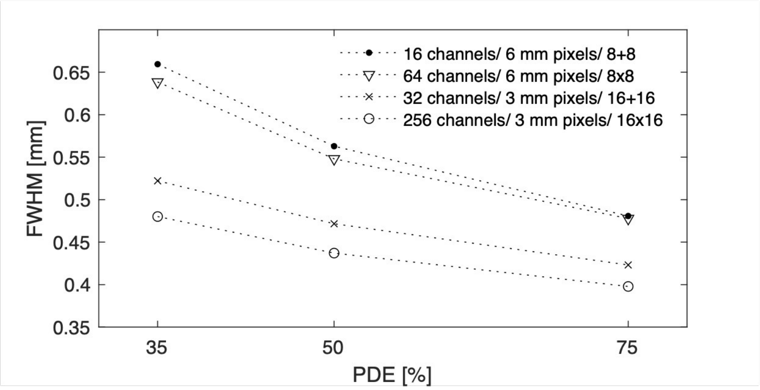

**Figure 6.10:** The detector spatial resolution in terms of FWHM and its dependency on the SiPM PDE.

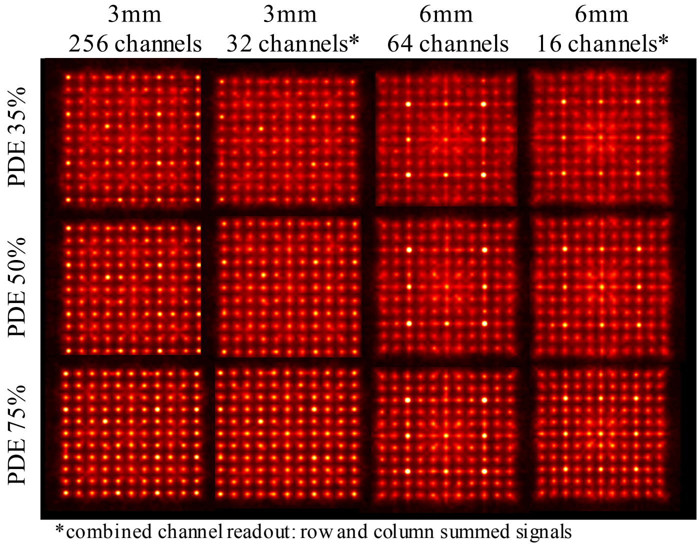

**Figure 6.11:** Positioning performance of the monolithic detector design. The estimated event positions are presented in 2D histograms dependent on different SiPM pixel sizes, PDEs and number of readout channels. The center region 10 x 10 $mm^2$ of the detector is evaluated.

**Table 6.7:** FWHM (mm) dependent on the PDE and readout channels.

| Readout channels | PDE 35% | PDE 50% | PDE 75% |
|---|---|---|---|
| 16 | 0.66 | 0.56 | 0.48 |
| 64 | 0.64 | 0.55 | 0.48 |
| 32 | 0.52 | 0.47 | 0.42 |
| 256 | 0.48 | 0.44 | 0.4 |

FWHM at 75% to 0.56 mm at 50% and 0.66 mm at 35%. The single channel readout with 64 channels leads to similar FWHM values: 0.48, 0.55 and 0.64 mm. For 3 mm pixels and a corresponding - combined row and column - 32 channel readout the FWHM values are 0.42, 0.47 and 0.52 FWHM. For the single channel 256 readout the values are slightly better: 0.4, 0.44 and 0.48 mm FWHM. In Figure 6.10 one can see the relatively small degradation introduced by summing row and columns while it is also visible that PDE has a larger effect on the larger pixel size (6 mm) than the smaller pixels (3 mm). Figure 6.11 shows histograms of estimated event positions for all scenarios. Increasing PDE visibly improves spatial resolution and reduces positioning bias. For 6 mm pixel size the high intensity spots (artefacts), arranged in a square-like pattern, are prominent, as well as the accumulation of events in the central region of the evaluated area. The effect of channel reduction is hardly visible.

### 6.4.4 Discussion and conclusion

In this section we analysed the influence of different PDEs on the obtainable spatial resolution. We found that the spatial resolution is strongly dependent on the PDE. Depending on the readout scheme the PDE reduction of 75% to 35% led to a resolution degradation of 16% - 30%. An improvement of SiPM PDEs would improve the spatial resolution due to higher signal-to-noise ratios. A similar effect would be obtained when a scintillator with a higher light yield could be used.

## 6.5 Influence of background radiation

### 6.5.1 Introduction

During the calibration of the detector in singles mode one has to deal with two kinds of background radiation that disturb the quality of the measurements. Here we analyse this background radiation which is the intrinsic $^{176}$Lu radiation of the scintillator and the events triggered by the gammas that exit the collimator housing due to insufficient attenuation thickness.

### 6.5.2 $^{176}$Lu radiation

Lutetium based scintillators, like LSO and LYSO, are the most widely used ones in PET today. Their properties make them very suitable for the detection of 511 keV gamma rays. The Lutetium contains 2.6% of $^{176}$Lu which decays naturally and generates a background signal in the detectors. The resulting spectrum coincides with the photopeak energies that are relevant in PET scans (Figure 6.12 a)). While during a PET scan the coincidence principle most of the time reliably distinguishes between a gamma coincidence and single background events, the background becomes a problem when performing measurements with the detectors in singles mode. This is the case when calibrating the detectors with a collimator. The challenge lies then in the filtering of background events to extract the calibration signal.

In Figure 6.12 a) the background signal is measured with our prototype detector and the events are positioned with simple Anger logic and presented in a 2D histogram. The distribution is uniform with an accumulation of events at each SiPM pixel center. The accumulation of events at single image pixels is due to the limited light spread of events that occur deep in the crystal, close to the SiPM array. The edge region (around 3 mm on each side) is depleted and the events are positioned more towards the center which can be described as a shadow between the first and second hotspot. The corresponding energy spectrum is presented in Figure 6.12 b). It consists of 3 characteristic peaks and a long tail towards the higher energies. The decay of $^{176}$Lu is a combination of a continuous beta decay leading to the long tail of up to 597 keV and a discrete energy deposition by multiple gamma decays which are 88, 202 and 307 keV (Figure 6.13). During the beta-decay

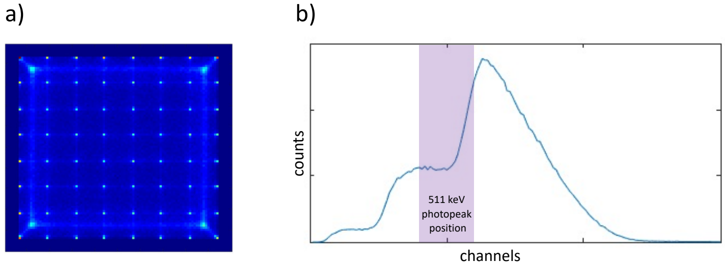

**Figure 6.12:** a) Histogram of positioned events of $^{176}$Lu background measurement. b) Corresponding $^{176}$Lu energy spectrum with indicated region of where the 511 keV photopeak would be expected.

an electron and an anti-neutrino are emitted. The beta spectrum is continuous because the energy is shared between the electron and the anti-neutrino. The electron deposits its energy inside the crystal while the anti-neutrino rarely interacts with matter. The combination of the continuous beta spectrum and the discrete gamma energies leads to the characteristic Lutetium spectrum. In Figure 6.14 a) the different energy combinations and in b) the resulting spectra are shown for a smaller and a larger crystal.

### 6.5.3 Importance of collimator design

To calibrate the monolithic detector a collimated beam is stepped over the detector. The measured signals per position are stored. The collimator itself does not produce a perfect calibration beam. We already discussed the beam diameter and spread in a previous section, however, there is also leak radiation present that generates signals at undesired detector locations. In Figure 6.15 a) the detector is irradiated in the crystal center. The source is shielded with at least 60 mm tungsten and only a very small fraction of gamma rays can pass the collimator to reach the detector. In Figure 6.15 b) an edge calibration position is sketched. As indicated with the arrows, here a part of the detector is exposed to gamma rays that could pass an only 40 mm tungsten shield which is expectedly a larger fraction of gamma rays. In Figure 6.15 c) an edge calibration position for a smaller crystal is shown. Smaller crystals suffer less from the effect of collimator leak radiation because they cover a smaller solid angle.

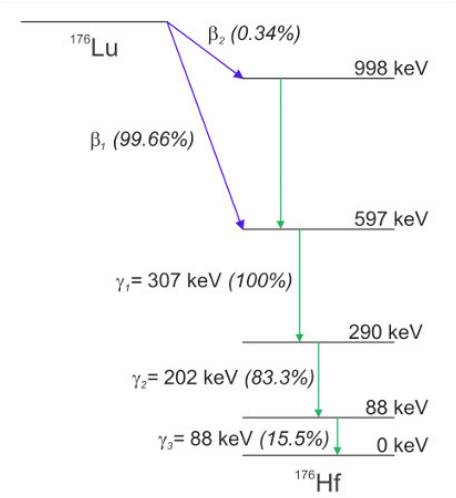

**Figure 6.13:** Decay scheme of $^{176}$Lu [123].

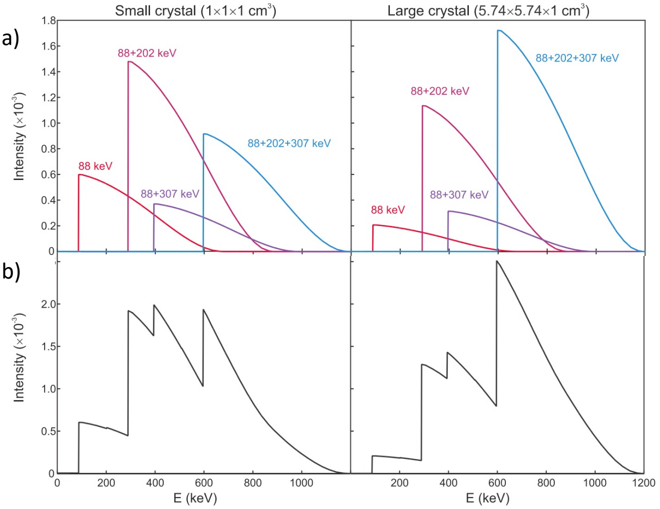

**Figure 6.14:** a) The energy spectra contributions for each of the gamma beta decay combinations for a smaller crystal geometry 1 x 1 x 1 $cm^3$ and a larger crystal geometry 5.74 x 5.74 x 1 $cm^3$. b) The individual contributions summed to a single spectrum. Figure adapted from [123].

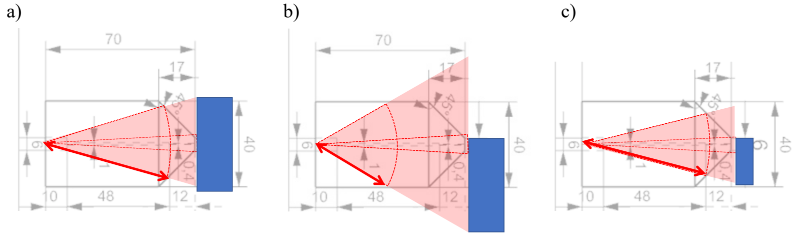

**Figure 6.15:** a) Travel path of gamma rays in collimator at central calibration position. The absorbing material provides a minimal shielding of around 60 mm tungsten (indicated by red arrows). b) At an edge calibration position using a 50 x 50 $\text{mm}^2$ scintillation crystal the minimal shielding decreases to around 40 mm. c) In a smaller crystal 25 x 25 $\text{mm}^2$ the minimal shielding is 60 mm even at edge calibration positions.

In Figure 6.16 the effect can be seen demonstrated with a BGO crystal. BGO is a scintillator with similar properties than LYSO but does not contain the radioactive $^{176}$Lu, hence no background radiation is expected. In a) the BGO crystal is irradiated at an edge position. One can clearly see the large signal detected at the opposite side of the detector. The more the calibration position is located in the detector center, as seen in b) and c), the less strong is the detected signal from collimator leak radiation. Experiments with additional shielding led to a reduction (elimination) of this effect.

### 6.5.4 Extraction from background

The combined effect from $^{176}$Lu background and collimator leak radiation can be seen in Figure 6.18 a). Due to the small collimator hole the signal-to-background ratio is quite low and it becomes necessary to filter the data to extract the relevant event signal. Especially for the edge calibration positions the highest signal in the histogram is not necessarily the region of interest. In Figure 6.18 b) many events that correspond to hotspots are filtered, to be able to automatically determine the calibration source position. In order to distinguish these events one can calculate, for each event, the standard deviation over all 16 readout channels (see flowchart in Figure 6.17). The fraction with the largest standard deviations are then removed from the dataset. In our case 20% led to an Anger histogram that allows a reliable distinction between background and source position. From the most intense pixel

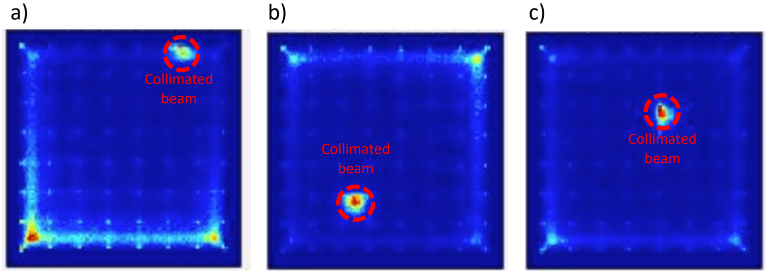

**Figure 6.16:** BGO crystal of 50 x 50 mm$^2$ without $^{176}$Lu background irradiated at 3 different positions. 2D histograms of events positioned with Anger logic. a) The beam is positioned at the top right corner. The strong signal in the lower left corner is caused by collimator leak radiation. In b) and c) the beam is positioned more in the center of the detector. A less strong signal is detected at the corners.

$$\begin{bmatrix} S1\ [ch_1 \dots ch_{16}] \\ S2\ [ch_1 \dots ch_{16}] \\ S3\ [ch_1 \dots ch_{16}] \\ \dots \\ \dots \\ S_N\ [ch_1 \dots ch_{16}] \end{bmatrix} \xrightarrow[\substack{standard\\deviation}]{} \begin{bmatrix} std1 \\ std2 \\ std3 \\ \dots \\ \dots \\ stdN \end{bmatrix} \xrightarrow[\substack{sort\\events}]{} \begin{bmatrix} S4\ [ch_1 \dots ch_{16}] \\ S2\ [ch_1 \dots ch_{16}] \\ S1\ [ch_1 \dots ch_{16}] \\ \dots \\ \dots \\ S_N\ [ch_1 \dots ch_{16}] \end{bmatrix} \xrightarrow[\substack{remove\\20\%}]{} \begin{bmatrix} S4\ [ch_1 \dots ch_{16}] \\ S2\ [ch_1 \dots ch_{16}] \\ S1\ [ch_1 \dots ch_{16}] \\ \dots \\ \dots \\ S_{\boldsymbol{N-20\%}}[ch_1 \dots ch_{16}] \end{bmatrix}$$

**Figure 6.17:** The flowchart depicts how to obtain a filtered Anger histogram that allows the determination of the beam source position. S1 to $S_N$ are the event signals each consisting of 16 channels $ch_1$ to $ch_{16}$. For each event the standard deviation std1 to stdN over the 16 channels is calculated. The events are sorted accordingly and a fraction (here 20%) of events is removed from the dataset.

in this figure a circular ROI is drawn, here of 37 pixels. The determined 'true' pixels (d)) are then extracted from the original image c). A too small selected ROI has a better SNR (includes less background signal) but also cuts off some events that are scattered. A too large selected ROI includes a lot of background events that are not representing the true signal from the calibration beam. For the training of the positioning algorithms it is valid to draw a ROI and exclude a number of scattered events, however, for the evaluation of the detector it would not be valid to exclude scattered events. For the evaluation the data is simply energy filtered and no ROI filter is applied.

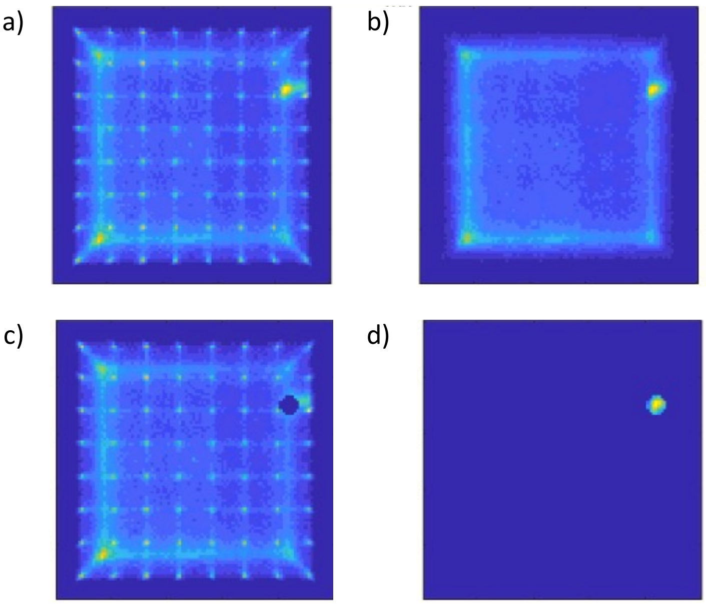

**Figure 6.18:** a) Unfiltered Anger positioned 2D histogram including $^{176}$Lu background events, collimator leak events and events from the calibration beam. b) The filtered histogram after removing events with high standard deviations. c) The original histogram excluding the ROI and d) only the selected ROI.

### 6.5.5 Discussion and conclusion

The calibration procedure with a collimated beam in singles mode involves some challenges, one of them being the contamination of the dataset with not-relevant signals from the scintillator intrinsic radiation and partially insufficient shielding of the calibration source. $^{176}$Lu background and collimator leak radiation make up a large fraction of the detected signal and need to be isolated from the set of reference signals in order to obtain the most reliable position labels for the training of the positioning algorithms. Here we analysed the contribution of both factors to the pre-positioning histograms and the energy spectra. By automated algorithms that first find the true beam position in the Anger positioned histograms and then extract the events that are positioned in a defined ROI one can obtain useful reference data. In conclusion, only with the automated selection of accurate ROIs and understanding of the energy spectra it is possible to generate reference data sets that lead to the best spatial resolution.

## 6.6 Summary and final conclusion

In this section we identified and analysed factors that have an impact on the spatial resolution. The discussed factors are the collimator beam size, the impact of Compton scattered events, the PDE of SiPMs and the background radiation of the detector when operated in singles mode.

Both simulation and experimental results showed that a beam size in the order of 0.6 and 1 mm does not significantly degrade the obtainable detector spatial resolution. A beam size of 0.6 mm or 1 mm is not a barrier to calibrate a detector with a high resolution of around 1 mm. From the test data to evaluate the detector outside the system the beam size needs to be taken into account. Here we showed that the beam size of 0.6 mm will degrade the measured resolution by 7% and a beam size of 1 mm will degrade the measured resolution by 21%. Implemented in a clinical system both detectors would show similar performance though. That means that beam size is not degrading the spatial resolution when the detector is implemented in a system. To estimate the real spatial resolution of the detector, which is only possible with ground truth position data from a perfect beam, we deconvolved the PSF with a rectangular function of the width of the collimated beam of 0.6 mm. The spatial resolution of 1.13 measured with the MNN algorithm improved to 1.05 mm after the deconvolution. In conclusion, the beam size does not need to be improved, the influence of the beam size on the actual detector performance is small. Quite the contrary, a larger beam size can be advantageous to some extent as the SNR improves.

Compton scattered events make a large fraction of the detected events and significantly degrade the detector spatial resolution. In simulations we tested the effect on spatial resolution and found that when only photoelectric events are present the resolution improves by 12%, and when only scattered events are present the resolution degrades by 32.5%. The resolution here was measured at FWHM, but foremost the scattered events are present in the tails of the PSF. In Section 7.3 of the next chapter a scatter determination network trained on simulation data is applied to our prototype detector.

The SiPMs low PDE introduces noise in the detector which degrades the spatial resolution significantly. The simulation study showed a resolution degradation of up to 30% when PDE dropped from 75% to 35%. In the experimental setting the SiPMs have an estimated PDE of 50%. There is additional noise introduced by the electronic readout which is difficult to determine. It is likely that the noise present in the prototype detector is slightly higher than what is simulated. A value between 35% and 50% is probable. A SiPM PDE improvement to 60% can further improve the detector performance but higher PDEs are currently not existing and available by any supplier. A higher scintillator light yield would have a similar positive impact on the spatial resolution.

The last section discusses the impact of the background radiation when operating a detector in singles mode. The impact of $^{176}$Lu and leak radiation from non-perfect collimator design were discussed and an efficient method to extract the valuable signals from the background by several filters was explained. On system level the detectors that are calibrated in singles mode can achieve very high resolution when one is aware of the background and the prior filtering steps are done properly.

In conclusion, by analysing and evaluating each factor separately one can evaluate the magnitude of the degradation and whether it is possible or necessary to improve the factor. This work was published in the form of several conference contributions.

In the next chapter we will train algorithms on simulated detector data and apply them directly to the prototype detector. On the one hand, to simplify or eliminate the need to do a physical detector calibration. On the other hand, to reduce the degrading effect of Compton scattered events by training an algorithm that can identify the events with the largest scatter distances.

# 7

# Simulated data applied to real detectors

## 7.1 Introduction

Throughout this thesis it has been shown that optical simulations are a great tool to support the PET detector development. Be it the prediction of detector performance metrics or the identification and analysis of degrading effects. Taking it a step further, we will now determine if we can use the simulated detector data and directly apply it to the training and positioning of the real detector.

In the first section we use the calibration maps generated by simulations to serve as reference data to position events of the prototype detector. The lengthy calibration is one of the major factors holding back the implementation of monolithic detectors in clinical PET scanners. A calibration based on simulated reference data could potentially allow an elimination of these lengthy measurements.

In the second section we want to tackle the degrading effect that Compton scattered events have on the spatial resolution. For the construction of a LOR only the first interaction position of the gamma ray in the detector is relevant. A scattered event with multiple interactions inside the crystal often leads to a distorted light distribution and an inaccurate position estimation (cfr. Section 6.3). Compton scatter is a factor that significantly degrades spatial resolution in monolithic PET detectors. Nevertheless, they are not treated differently as photoelectric events, probably because it is very difficult to distinguish between scattered and non-scattered events in experimental set-ups. To improve the positioning of Compton scattered events we assume that the interaction position of far-scattered events are most difficult for the algorithms to position. Far-scattered means, the distance between the first and last interaction position is large. Therefore scintillation light is emitted 'far' from the first interaction position which leads to a more distorted light distribution for 'far' scattered events. Subsequently a detection and elimination of the farthest scattered events should lead to an improvement of the overall resolution.

In the thesis of Decuyper [129] a neural network was trained based on simulated data to distinguish the scatter distance from the detected light distribution. While Decuyper applied the network to simulated data, we apply it to the real detector. In conclusion, we want to determine the scatter distance of real events and evaluate if an improvement of the resolution can be achieved.

## 7.2 Detector calibration with simulations

### 7.2.1 Introduction

Statistical event positioning methods require light distribution profiles along with the 2D interaction position. As has been mentioned several times throughout this work, this requires a lengthy calibration process that scans the crystal in a narrow grid. Several methods have been proposed to avoid acquiring the calibration datasets. One can for example use theoretical models that describe the light distribution, use detector uniformity flood maps, or use simulations [69, 73, 131–135]. In Li et al. [134] several analytical solid angle models were used to describe the relation between the gamma interaction position and the photodetector signal. The internal reflections at side and top surfaces are modelled using virtual mirrored sources outside the crystal. From these virtual sources the solid angles can be drawn that arise from the reflected rays. From the model the 3D coordinates can then be estimated using nonlinear least square fitting. The models were applied to experimental data and achieved a spatial resolution of 1.4 mm FWHM in a 20 x 20 x 10 $mm^3$ LSO crystal. This method was further developed by Extebeste et al. [136] to test its performance for different reflective materials. The results show that for reflectors that are not fully specular, but more diffuse, it is better to limit the influence of internal reflections in the model especially towards the detector edges. Here a FWHM of 1.2 mm was measured for a 10 mm thick white painted LYSO crystal. The authors repeat the importance of modelling the type of reflections at the crystal edges properly and that it strongly depends on the interaction position inside the crystal. Later this work was extended to tapered crystal geometries leading to spatial resolution of 1-1.5 mm FWHM using 12.25 mm thick crystals [135].

To create realistic light distributions of monolithic crystals analytically or with simulations requires the exact knowledge of the reflection probabilities and reflection directions of the reflected optical photons. To describe this analytically is very difficult since the reflections are complex and the conditions change at every location in the crystal. Often there are multiple reflectors used and also the reflections at the photodetector readout surface should not be forgotten.

Optical simulations of monolithic detectors are able to track each optical photon and decide at each interface whether the photon is reflected or not, and in which direction. These decisions are based on LUTs that are calculated including measured surface data of the crystal, refractive indices and reflection probabilities (of crystal surface and reflector). Subsequently a light distribution can be generated that is very close to the real distribution. The reader is referred to Section 3.8.3 to find more details on surface reflection models. Optical simulations have gone through some fundamental changes in the last years, like (i) the availability of more accurate surface reflection models, and (ii) the high computing power that is needed to run these simulations, for example computer clusters.

Here we use the calibration maps generated by optical simulations from Chapter 4 to serve as reference data to position events of the prototype detector.

### 7.2.2 Materials and methods

#### Spatial resolution estimation

The simulated detector calibration and the corresponding calibration data LUTs as described in Chapter 4 are used to position events from the prototype detector. The simulated calibration data LUTs were generated with a perfectly collimated beam. They consist of a 16 channel, summed row and column readout which is also the readout scheme of the prototype detector. We simulated three different PDEs: 35%, 50%, and

75%. The calibration data LUTs with PDE 35% were selected for this study as the prototypes SiPM PDE (ON Semiconductor MicroFJ-60035-TSV) is around 50% and the electronics introduce additional noise. When simply comparing a subset of mean detector signals between the simulated and experimental data a good fit could be observed (Figure 7.1). Identical to Section 5.2.3, 30000 energy-filtered events per position without ROI selection were positioned with the MNN algorithm. The performance is evaluated based on two parameters: FWHM and 1D/2D-bias (cfr. Section 5.2.5).

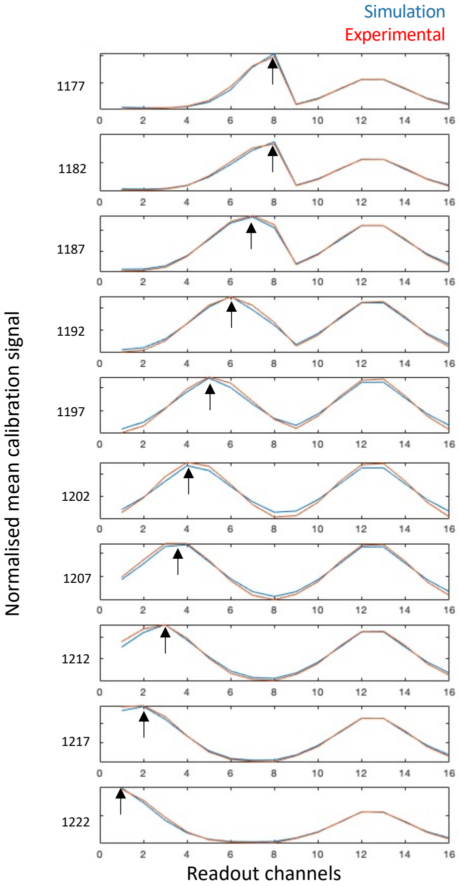

**Figure 7.1:** Mean calibration signals from simulation (blue) and experimental calibration data (red) from a subset of calibration position starting with position 1177 corresponding to row 23 and column 1 of a 49 x 49 calibration grid. The following signals are presented in 5 mm intervals along row 23. The readout channels 1 to 8 correspond to rows and 9 to 16 correspond to columns. The error indicates the peak shift due to the beam moving along one row. The peak position for the column is constant.

### DOI estimation

Each of the reference events belongs to a certain depth-layer defined by the signal variance and therefore DOI of the event. To evaluate the DOI estimation the predicted relative number of events in each of those layers is compared to (i) the theoretical number of events that we expect by the attenuation of the crystal according to Beer-Lambert Law and (ii) the results we previously obtained from positioning the same events with calibration maps of the actual detector.

### Bar phantom

Additional to the analysis of the point spread function, the four-quadrant bar phantom gives a more visual impression on the detector performance. With this phantom the spatial resolution of the detector can be assessed by its capability to resolve adjacent bars. The methods are identical to those in Section 5.2.5 except that all events are positioned with simulated calibration data LUTs. The most important methodological steps are repeated below.
Recorded events are filtered with an energy window of 20% and positioned with the MNN algorithm. The flood source histograms are generated as in Section 5.2.5 except the positioning is done with the simulated calibration data LUTs. The bar phantom histograms are then normalized with the flood source histograms. The line profiles are summed per quadrant and the peak-to-valley ratios are determined to calculate the MTF values.

## 7.2.3 Results

### Spatial resolution estimation

The estimated mean and median spatial resolution of the prototype detector when using completely simulated calibration maps is stated in Table 7.1 *sim-exp*. For the full detector the estimated resolution is 1.38 mm and 1.28 mm for the detector center. The median FWHM values for the full detector are 1.34 mm and 1.28 mm for the detector center. The mean and median bias values are 0.48 mm and 0.46 mm for the full detector and 0.2 mm and 0.23 mm for the detector center. The resulting mean 2D bias is 0.76 mm and 0.35 mm for the center. For reference the

**Table 7.1:** Performance parameters when using simulated calibration maps to position experimental data.

| | MNN exp-exp | | MNN sim-exp | |
|---|---|---|---|---|
| | 50 x 50 mm$^2$ | 30 x 30 mm$^2$ center | 50 x 50 mm$^2$ | 30 x 30 mm$^2$ center |
| FWHM mean | 1.17 | 1.13 | 1.38 | 1.28 |
| FWHM median | 1.17 | 1.14 | 1.34 | 1.27 |
| Bias x mean | 0.37 | 0.14 | 0.48 | 0.2 |
| Bias y mean | 0.37 | 0.16 | 0.46 | 0.23 |
| 2D Bias | 0.59 | 0.26 | 0.76 | 0.35 |

results from a calibration with experimental data (cfr. Chapter 5 are also stated in Table 7.1 *exp-exp*. The resolution per calibration position is plotted in Figure 7.2. The bias is indicated as arrows.

### DOI estimation

The DOI estimation is presented in Figure 7.3. The theoretical distribution and distribution obtained by positioning the experimental data with experimentally acquired calibration LUTs have already been shown in Section 5.3.2 and are shown here as a reference. The distribution obtained by positioning the experimental data with simulated calibration LUTs leads to 28.6% of events in layer 1, 20.6% in layer 2, 14.2% in layer 3, 10.8% in layer 4, 11%, in layer 5, and 14.8% in layer 6.

### Bar phantom

The bar phantom plots are shown in Figure 7.4. In a) the measured data is positioned with experimentally acquired data (result from Chapter 5) and in b) positioned with simulated calibration maps. In terms of bar-distiguishability both bar phantom histograms allow the separation of bar widths down to the smallest bar pattern of 0.6 mm. The bars are less uniform and more noisy in a) compared to b). The quantitative analysis of the bars is shown in Figure 7.5. The red lines represent the summed line profiles of the bar phantom positioned with the simulated calibrations maps and the black lines the one positioned with the experimental calibration maps. For both, the peaks can be distinguished easily for all bar widths. Only towards the detector edges the distinguishability lowers. The positioning with simulated calibration maps is indeed less uniform as already visually inspected in Figure 7.4. Finally, in Figure 7.6 the MTF is calculated from the peak-to-valley ratios. For all bar widths the simulated calibration maps lead to a significant degradation of 2.8%, 4.0%, 2.3%, 0.26% for the largest to smallest bar pattern, respectively. The relative degradation is 15.2%, 32.7%, 37.4%, and 9.8%.

### 7.2.4 Discussion and conclusion

The aim of this study is the performance evaluation of the experimental data using simulated calibration maps. Even though we did not adapt the simulated data for any SiPM gains or detector non-uniformities the channel values for the mean events from simulation and experiments show a close correlation. The obtained spatial resolution show a resolution degradation of 11.7% in the detector center and 15.2% over the whole detector compared to the results from Chapter 5 that are based on experimental detector calibration. The overall bias increases by 27%. Comparing to Figure 5.7 especially the bias at the edges is noticeable. This might be a sign for inaccurate modelling of the black painted and rough crystal walls. At these detector locations the number of reflections is much larger than in the rest of the detector, therefore accurate modelling is more important. Rough surfaces in general show a larger variation in micro-facet distribution than polished surfaces. Thus, the modelling is more likely to be inaccurate when using a random rough surface model for the representation of a rough surface from a different crystal and vendor. The Davis LUT reflection model used in this study provides surface models based on measured polished and rough surfaces. An implementation of a rough surface model based on measured data from the specific crystal provider could lead to more accurate modelling. Furthermore, the black paint simulation model has been developed specifically for our study and has not been validated experimentally. It assumes that all photons interacting with the reflector material are absorbed. In reality, the black paint is probably not 100% absorbing and additionally between the crystal surface and the black paint there are probably air inclusions leading to a lower refractive index and higher reflection probability. The number of absorbed photons at the detector edges might be overestimated. To improve these results one should (i) re-evaluate the modelling of the detector edges or (ii) develop a detector with surfaces that are easier to model, such as polished surfaces with more common reflectors like Teflon or ESR. However, the remaining spatial resolution is still in a range that allows a 2 mm system resolution in a system with a diameter as large as 80 cm (cfr. Figure 2.9).

The bar phantom histogram supports the results obtained from the PSF analysis. The bars can be distinguished down to the 0.8 mm profile with more than 5% contrast. FWHM value is calculated as the smallest resolvable bar times 1.4-2 [5]. Thus the bar phantom measurement shows a detector resolution of 1.12-1.6 mm FWHM. The increased positioning bias is visible in this measurement. An adaptation of the channel gain or similar procedures could be applied in the future to account for non-uniformities.

To our knowledge no published work exists that has calibrated monolithic detectors solely on simulated data and achieved this high resolution.

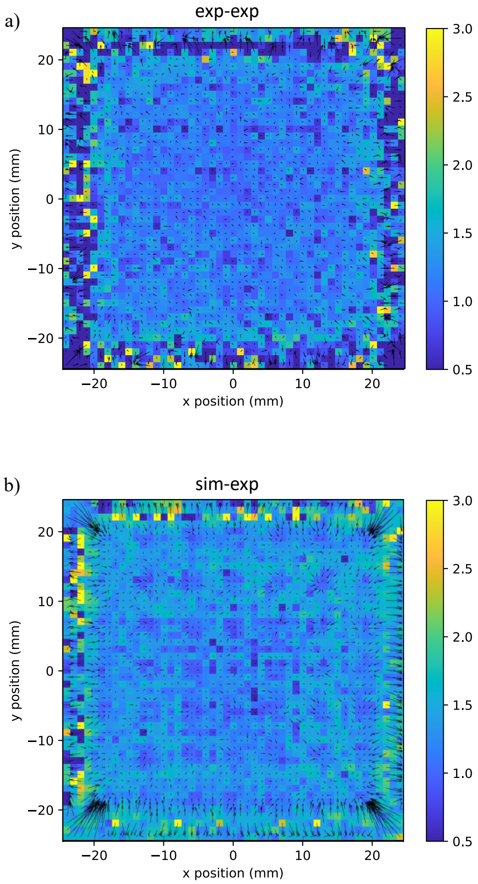

**Figure 7.2:** Spatial resolution as FWHM [mm] for the detector prototype that is calibrated a) on experimental data and b) entirely on simulated data.

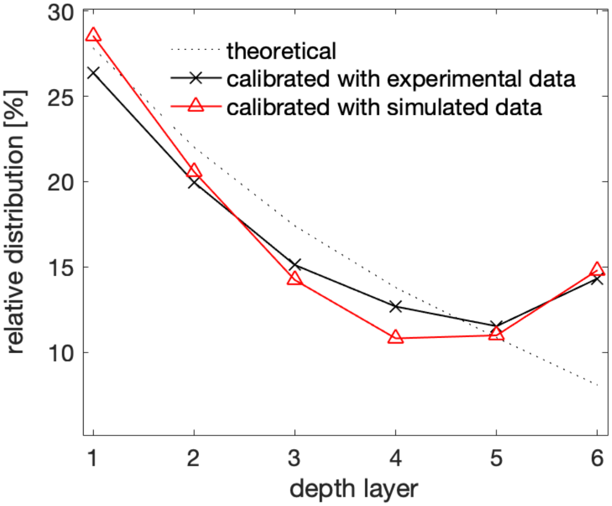

**Figure 7.3:** DOI performance of the detector prototype that is calibrated on simulated data. As a reference the DOI performance for a detector calibrated on experimental data is plotted and the theoretical (expected) values per depth layer.

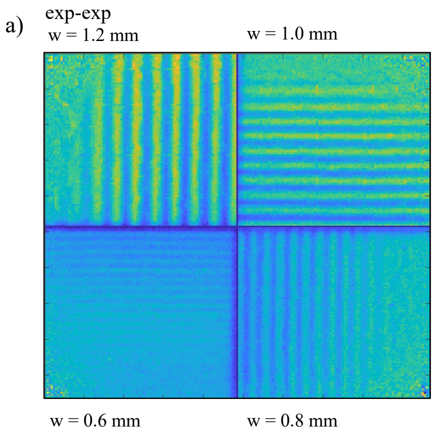

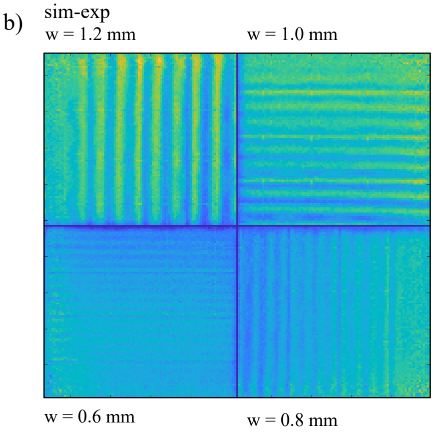

**Figure 7.4:** Bar phantom measurements a) calibration data is acquired experimentally and b) calibration data is simulated.

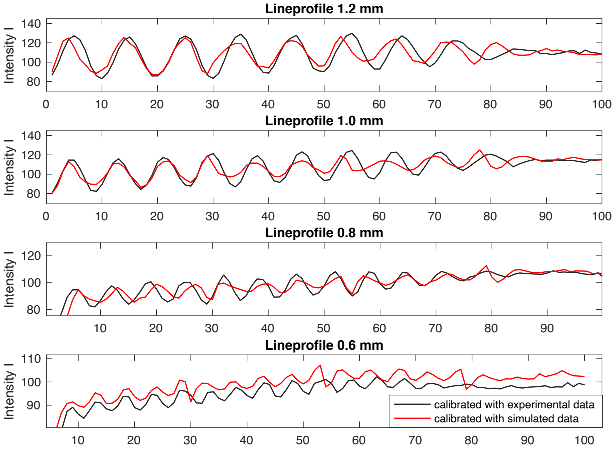

**Figure 7.5:** Quantitative evaluation of the bar phantom. Line profiles per quadrant are summed and plotted for bar phantom calibrated with experimental (black) and simulated data (red).

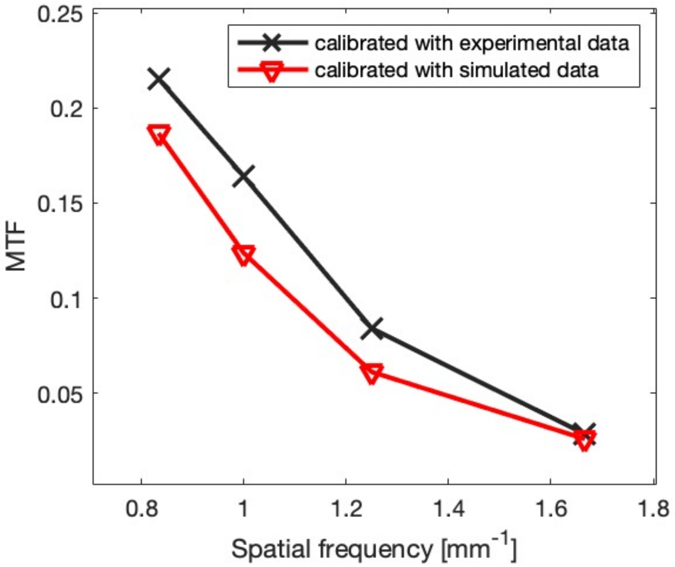

**Figure 7.6:** MTF values in terms of spatial frequency of the bar phantom for experimental (black) and simulated data (red).

## 7.3 Scatter distance estimation network

### 7.3.1 Introduction

In Section 6.3 the influence of Compton scattered events was evaluated based on simulated data. The results showed that scattered events lead to a major degradation of the spatial resolution. In experiments it is very difficult or impossible to investigate the effect of scatter. The simulations allow us to collect the ground truth interaction positions of each gamma photon individually.

These data allowed us to investigate the training of neural network to identify Compton scatter and process them with different positioning networks. While it was difficult to improve positioning performance by specifically training algorithms on scattered data, it was shown that the overall detector performance could be improved by discarding events that have a large 3D scatter distance and therefore a large positioning error (Figure 7.7). Following up on that idea, an algorithm was trained that can determine the scatter distances between the first and last interaction position in the crystal [127, 129] . With the scatter distance one can then set a threshold (depending on the application) to define how many events are removed from the dataset. Applied to simulated detector data we were able to estimate the scatter distance of gamma rays especially for far scattered events. The removal of 5% of the far-scattered events improved the 3D positioning distance by 9%, a removal of 10% lead to an improvement of 18%. In experiments it is not possible to train networks the same way because there is no information on 3D scatter positions available. Here we apply the network trained on simulated data to experimental data.

### 7.3.2 Materials and methods

The training data is the same as used in Chapter 4. The trained network architecture can be seen in Figure 7.8 and is the same as described in Section 5.2.4 i.e. three hidden layers of 256 neurons with leaky ReLU activation. The inputs are the 16 channel signals from all 49 x 49 detector calibration positions. The output and ground truth labels are the 3D scatter distances. 40% of the events in the data-set are not-scattered and due to the perpendicular incidence angle of the calibration beam most of the scattered events are forward scattered events with

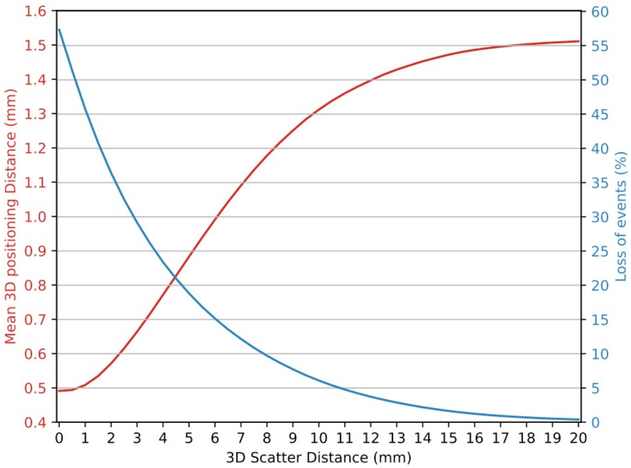

**Figure 7.7:** The positioning performance is investigated as a function of the 3D scatter distance of the gamma and the removal of those events with the largest scatter distances [129].

a light distribution that resembles that of a non-scattered event. To avoid that the network is overestimating the number of non-scattered events it is only exposed to the scattered data. The network is trained on 1000 events per calibration position using the AdamW optimisation algorithm, mini-batch size of 256 events, MSE loss and L2 weight decay set to 0.01. One epoch is defined as an iteration over 240,100 events, randomly sampled with replacement from the entire training set. The initial learning rate was set to 0.001 and halved every 10 epochs that the validation loss did not improve. Early stopping was applied after 60 epochs without improvement. The network was implemented in PyTorch and trained on a MacBook Pro with a 2.8 GHz Quad-Core Intel i7 CPU. The described methods above are partially adapted from [129] where this network is first described.

### Bar phantom

Theoretically, to test the scatter distance estimation network one would produce data with 'ground truth scatter distance' - labels and then determine how well the network can reproduce these values. Since it is not possible to obtain ground truth information on the scatter distance

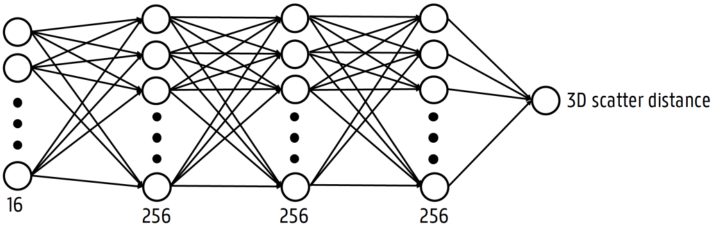

**Figure 7.8:** Scatter distance estimation network.

from experimental set-ups, the evaluation is done with the bar phantom measurement. The hypothesis is that if the far-scattered events are removed successfully, the contrast should improve in the bar phantom measurement.

The bar phantom data is evaluated by the scatter distance estimation network. A fraction of the far-scattered events are removed from the datasets i.e. 10%, 20%, and 40%. The same procedure is applied to the uniformity histograms. The bar phantom plot is normalized by the uniformity measurement. The bar phantom evaluation is done as in Section 5.2.5.

### 7.3.3 Results

In Figure 7.9 the bar phantom images are presented. The respective fraction of removed 'far-scattered' events is stated below each image. Visually it is difficult to find differences, however, when focussing on the upper left quadrant with the largest bars and comparing Figure 7.9 a) to d), then one can clearly see an improved contrast. For the quantitative evaluation of the contrast we use the peak-to-valley values of the summed line profiles and calculate the resulting MTFs (Figure 7.10). The smallest spatial frequency 0.83 $\mathrm{mm}^{-1}$ corresponds to the bar width of 1.2 mm. The MTF contrast values are 21.5% initially, without removing any scattered events. The removal of 10%, 20% and 40% of the farthest scattered events determined by the neural network lead to an improvement of the contrast to 22.7%, 23.6% and 26.1%. This is a relative improvement of 6%, 9% and 18%.

For the largest spatial frequency 1.67 $\mathrm{mm}^{-1}$ (0.6 mm bar width) the MTF contrast values are 2.8% initially, without removing any scattered events. The removal of 10%, 20% and 40% of the farthest scattered

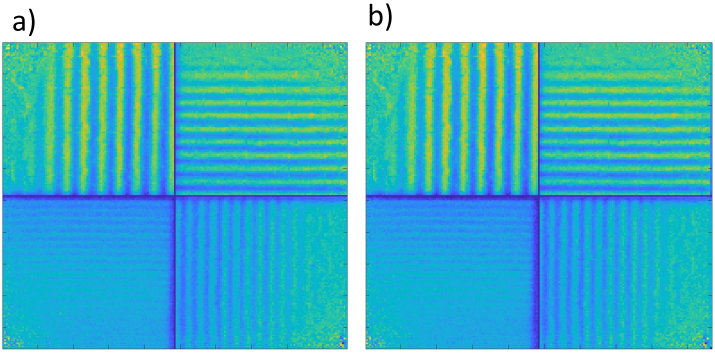

0% scattered events removed

-10% scattered events removed

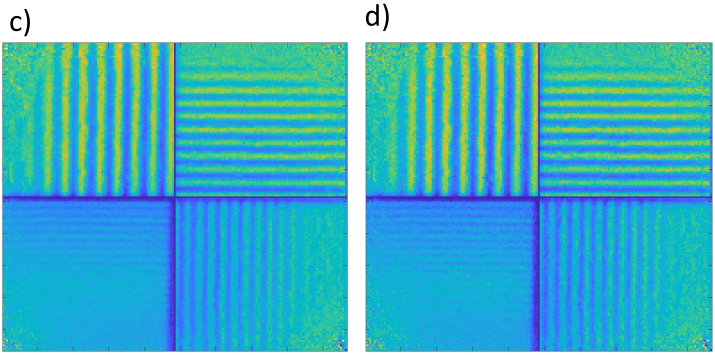

-20% scattered events removed

-40% scattered events removed

**Figure 7.9:** Scatter distance estimation network applied to the bar phantom measurement. Several scatter distance thresholds are applied. In a) no events are removed, in b) 10% of the determined farthest scattered events are removed, in c) 20% are removed, in d) 40% are removed.

events determined by the neural network lead to an improvement of the contrast to 3.2%, 3.4% and 3.9%. This is a relative improvement of 12.5%, 17.6% and 28.2%.

### 7.3.4 Discussion and conclusion

In this section we applied a scatter distance estimation network trained on simulated data to experimental datasets. Since it is impossible to acquire ground truth scatter distance data the algorithm is evaluated on the bar phantom measurements. An improved contrast indicates that the scatter distance determination is meaningful in the sense that

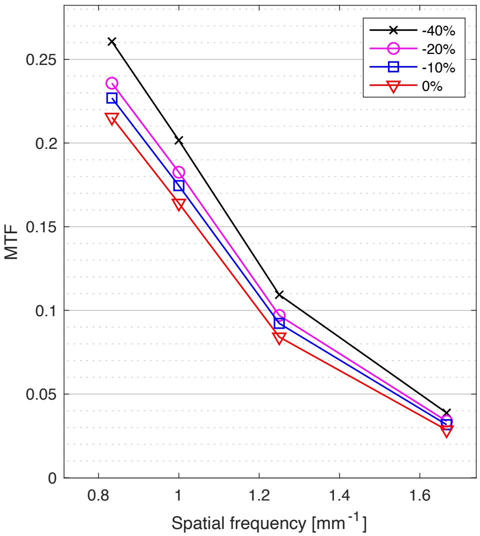

**Figure 7.10:** MTF values in terms of spatial frequency of the bar phantom.

events can be sorted correctly according to their scatter distance, even though the absolute distance metric is probably not reliable. The results show that when 10% of the farthest scattered events are removed from the dataset the contrast can be improved by 6% for the 1.2 mm bar width and 18% for the 0.6 mm bars. When up to 40% of the farthest scattered events are removed the contrast can be improved by 12.5% for the 1.2 mm bar width and 28% for the 0.6 mm bars. This is a drastic improvement that indicates that far scatter distances degrade the resolution drastically and that it is possible to filter these events. However, one has to trade the resolution improvement for sensitivity which for coincidence measurements are introducing a squared loss since always two detected gammas are necessary to form a LOR.

## 7.4 Summary and final conclusion

In this chapter we used the simulated detector data to directly apply it to the training of the actual detector. In the first section we test which spatial resolution we can retain when using the simulated calibration data to position events from the prototype detector. The obtained spatial resolution is 1.38 mm FWHM over the whole detector and 1.28 mm in the detector center. This is a degradation of 15.2% and 11.7% respectively. The bias increased by 27% being strongly linked to the degradation at the detector edges. The increased bias might be related to an inaccuracy of the reflection modelling of the black painted crystal sides. Future research to improve these results should be focused on a re-investigation of the reflection and absorption properties of black paint or consider a scintillation crystal surface treatment that is easier to model. The obtained resolution is degraded but still in the range to obtain a 2 mm system spatial resolution in a system with a diameter as large as 80 cm.

In the second section of this chapter we use the advantages of simulations that can provide ground truth information of all interactions of each single gamma ray along its trajectory. With this information we can train a network to estimate the scatter distance of the gamma ray and subsequently allow the user to exclude far-scattered events from the dataset. We used the bar phantom measurement to evaluate whether the contrast improves when removing certain amounts of far-scattered events. The results showed us that removing only 10% of the farthest scattered events leads to an improvement of 6% to 18% depending on the bar pattern width. Further reduction of far-scattered events to 40% improves the contrast by 12.5% and up to 28%. Even though this improvement can only be achieved trading for sensitivity, there are applications where the count rate is sufficiently high to trade it for spatial resolution.

In conclusion, the developed optical model for our monolithic detector and the performed optical simulations provide a realistic representation of the true detector. The simulated calibration maps can provide a high spatial resolution and the scatter distance estimation network can further improve the resolution.

# 8

# Conclusions and future perspectives

## 8.1 Summary

The purpose of this dissertation was to study the ultimate spatial resolution that can be obtained from a thick monolithic detector for the use in clinical PET applications. First, we investigated the expected detector performance in an optical simulation study. Then, we focussed on the construction of a prototype detector and design of a calibration set-up. During this process we encountered several challenges and could identify important degrading factors that influence the spatial resolution. The combination of comprehensive simulations and lab experiments allowed us to analyse these critical factors and understand the ultimate effect on the detector performance on system level. Finally, we applied the simulated data directly to the real detector. In first instance, to replace the lengthy detector calibration procedure and secondly, to improve positioning of scattered events.

In Chapter 2 and 3 we build the basis to grasp the principles of PET and gamma ray detectors. To understand our motivation to use monolithic detectors for clinical PET one needs to understand the physics behind a PET scan and the factors that fundamentally limit PET system resolution. We calculated that in a system of 65 cm diameter and using $^{18}$F as a tracer, the detector spatial resolution must be about 1.3 mm to not be a significant degrading factor for the system resolution. The system resolution is then close to the physics imposed limit which is around 2 mm. The 2 mm are attributed mainly to the system diameter and non-collinearity of the gamma propagation, while the positron range has a smaller influence. Additionally, a detector with DOI capability helps to maintain spatial resolution over the whole FOV, radially as well as axially. Considering these conditions, the monolithic detectors can provide much higher intrinsic spatial resolution than pixelated detectors while not loosing other important performance metrics such as sensitivity and energy resolution. In terms of timing resolution pixelated detectors are still superior, however, the unrestricted movement of scintillation photons with a direct travel path to the photodetector makes monolithic crystals fundamentally superior to be used for timing measurements.

In monoliths DOI can be extracted from the measured light distribution. On the contrary to provide high spatial resolution with pixelated detectors, the scintillation crystals need to be finely segmented. This leads to a large loss of sensitivity since the reflective material between the segments introduces dead space. The sensitivity loss is squared in PET scanners since always two gamma rays are needed to detect one LOR. Further, the manufacturing becomes very expensive, more expensive compared to monolithic detectors when requesting arrays of segmented crystals below 2 mm width. The high number of reflections per scintillation photon in a thin long pixelated crystal, leads to a loss of these photons and worse light collection efficiency. Less collected light photons lead to lower SNRs and worse energy resolution. Also, the more reflections the longer it takes to collect all light. DOI capability is usually only available at the cost of additional hardware or more complex detector design, such as double-ended readout or phoswhich. In summary, the monolithic detector is more suitable to provide high overall performance when high spatial resolution is desired.

In Chapter 4 simulations are used to investigate the detector performance of our monolithic detector design under idealised and controlled circumstances. We study several hardware-related parameters that are difficult to study or cannot be studied in depth in experimental set-ups. An optical simulation study of a 50 x 50 x 16 $mm^3$ LYSO crystal with SiPM readout is performed. The event positioning algorithm is a MNN algorithm. The indicated 2D spatial resolution of the detector is 0.4-0.66 mm FWHM in the detector center. A clear advantage is a smaller pixel size (here tested 3 mm and 6 mm) and also a higher PDE. Reducing the number of readout channels by a factor of 4, however, had no significant impact on the resolution. The performance slightly degrades towards the edges. The DOI could be estimated with an accuracy of 72% and a mean absolute positioning error of 1.6 mm.

In Chapter 5 we build and evaluate the prototype detector which has 6 x 6 $mm^2$ pixels that are summed in rows and columns to a 16-channel readout. The obtained mean spatial resolution is 1.13 mm FWHM with small degradations towards the edges. The evaluation was extended to a second positioning algorithm based on neural networks. This trained network achieved a more uniform resolution and smaller bias. The mean spatial resolution is 1.02 mm. The aim to reach 1.3 mm intrinsic spatial resolution was exceeded by both algorithms. As mentioned above, this intrinsic spatial resolution will not impose degradation to the system spatial resolution in clinical PET scanners. DOI capability was enabled and implemented for both algorithms by a layer approach which will result in a nearly uniform system spatial resolution over the full FOV. The detector energy resolution is around 11% (comparable to pixelated detectors) allowing a reliable distinction between scattered and non-scattered events.

The simulations in Chapter 4 and the prototype development in Chapter 5 allowed us to identify many factors that have an effect on the spatial resolution. In Chapter 6 we use the combination of both, to further investigate those factors. First, the impact of the beam size is investigated. In our calibration set-up we can only collimate the beam to a diameter of 0.6 mm. In simulations and experiments we investigated two questions: 1. How do the slightly shifted gamma interaction positions affect the calibration and training of the detector? 2. How does it affect the detector evaluation? Both, simulations and experiments, confirmed that a 0.6 mm and a 1 mm beam size allows the calibration and training of a detector with comparable high resolution. The MNN and neural network results are not negatively impacted by the slightly spread gamma interaction positions. However, for the detector evaluation the non-perfect calibration beam has a negative effect that needs to be taken into account. For this purpose the beam diameter can be isolated with a deconvolution. For our prototype detector this resulted in a improvement from 1.17 mm to 1.05 mm when the beam width of 0.6 mm was deconvolved from the measured PSFs.

The second degrading factor is the impact of Compton scattered events. More than half of the detected events have scattered once or multiple times resulting in an altered light distribution. In a simulation study we found that the resolution in terms of FWHM would improve by 9-12% when excluding scattered events (i.e. sensitivity loss of 50-60%). When only positioning scattered events we do see a resolution degradation of more than 32%. Scattered events impact not only the FWHM metric but also the tails are broadened by scattered events. Compton scattered events have a significant influence on the detector spatial resolution. We investigate in the Chapter 8 whether it is possible to improve positioning of Compton scattered events.

As a third degrading factor we investigated the SiPM PDE. It is defined as the probability that a single photon is detected when impinging on the SiPM surface. Current SiPM PDEs range between 35% and 60%. In simulations a PDE reduction of 75% to 35% led to a resolution degradation of 16-30% depending on the size of SiPMs and the number of readout channels. We conclude that higher PDEs improve the SNR and are a major contributor to better spatial resolution detectors. Unfortunately PDEs higher than 60% are currently not existing and available by any supplier. The SiPM PDE is however expected to improve further in the future. Also the introduction of scintillators with higher light yield and hence, more photons per energy unit deposited in the detector, would have a similar positive effect.

The fourth degrading factor is the background radiation. A detector calibration in singles mode suffers from a strong background signal, i.e. a detection of events that are not 511 keV gamma photons originating from our calibration beam. First of all, there is the intrinsic $^{176}$Lu radiation of the Lutetium-based scintillation crystal. It introduces a background signal with a complex energy spectrum covering the gamma photopeak. The amount of background radiation increases with detector volume. Secondly, the collimator does not provide sufficient attenuation thickness so that, at large solid angles, more gammas from the calibration source can exit the collimator housing. Potentially the radiation from both sources contaminate the calibration data. Here we presented effective methods to filter relevant calibration events from background. With these methods we can train high resolution detectors even when a large background signal is present during calibration.

We presented four important degrading factors in this chapter. The individual consideration of each degrading factor allows us to identify the origin and quantify the magnitude of the degradation.

In Chapter 8 we use the simulated detector data to directly apply it to the training of the actual detector.

The main drawback of monolithic detectors is the need for a calibration that requires a dedicated lab set-up and often a separate calibration for each detector. If the calibration procedure could be replaced by

simulated calibration data the actual calibration could be avoided. Additionally, simulations provide ideal conditions, such as a perfect calibration beam, no intrinsic detector activity, and provide ground truth information on DOI and scatter interactions.
First, we test which spatial resolution we can retain when using the simulated calibration data to position events from the prototype detector. The obtained spatial resolution is 1.28 mm with a degradation towards the edges. Compared to the experimental calibration this is a degradation of 11.7%. The overall bias increased by 27% mostly attributed to the detector edges. The increased bias might be related to an inaccuracy of the reflection modelling of the black painted crystal sides. Future research to improve these results should be focused on a re-investigation of the reflection and absorption properties of black paint or consider a scintillation crystal surface treatment that is easier to model (cfr. next section 'Future research'). The obtained resolution is slightly degraded but still within the range to obtain a 2 mm system spatial resolution in a system with a diameter as large as 80 cm. This preliminary study provides promising results for the role of optical simulation studies and to potentially replace the cumbersome calibration procedure.
In the second section of this chapter we use the advantage that simulations can provide ground truth information on all interactions of each single gamma ray along its trajectory. With this information we can train a network to estimate the gamma scatter distances and subsequently allow the user to exclude far-scattered events from the dataset. We used the bar phantom measurement to evaluate whether the contrast improves when removing certain amounts of far-scattered events. The results demonstrated that removing only 10% of the farthest scattered events leads to an improvement of the MTF by 6-18% depending on the bar pattern width. Further reduction of far-scattered events to 40% improves the contrast by 12.5 and up to 28%. Even though this improvement can only be achieved by trading in sensitivity, there are several applications where the count statistics are sufficiently high.

## 8.2 Future research

Based on the results of this dissertation, a number of future research topics are discussed in this section.

In terms of further improving spatial resolution we showed that very high intrinsic 2D spatial resolution can be obtained with the presented methods. Even at the very edges of the detector only relatively small degradations were present. A further 2D resolution improvement would not necessarily be advantageous on system level since there are other dominating factors, such as the non-collinearity and positron range. However, improved resolution could be traded for other degrading factors like (i) using a thicker scintillator, (ii) less calibration data or coarser calibration grid (ii) larger SiPM pixel size or (iii) less readout channels. An important research topic in the future is the implementation of meaningful evaluation standards for the spatial resolution estimation across different research institutes. The variability of the methods makes it very difficult to compare the performance of different detectors, restraining the progress in the field. The differences are introduced by: (i) the calibration beam size and the method that is used to correct for it, (ii) the energy or position filtering of the data, (iii) the evaluated region of the detector (centre, edge, corner, line on one axis), (iv) the PSF evaluation (directly measuring FWHM or first fitting a function to the PSF), (v) type of fitted function (Gaussian, fitted to peak or complete PSF?) (vi) DOI evaluation (by side irradiation or 'expected events per layer') etc. The list can be further extended. Instead of evaluating PSFs, the measurement of a standardised bar phantom as it is first used in this dissertation could be useful. A measurement standard on how to use the phantom could be implemented. The phantom allows the estimation of the spatial resolution across the whole detector with a single measurement and also shows the detector linearity.

Even more challenging than 2D resolution evaluation is the DOI performance estimation. Experimental DOI settings using a side irradiation are highly impractical. While it is a reasonable measurement in thin pixelated detectors, the side irradiation in monolithic crystals has two major disadvantages (i) most events are interacting close to the crystal edge and (ii) Compton scatter are dependent on the incidence angle and therefore the side irradiation introduces light distributions that are not representative, nor realistic. An important future step might therefore be the training of DOI with neural networks and simulated data for real detectors.

While this thesis led to several design indications aiming at high spatial resolution, one should carefully consider whether or not the detector should also be optimized for TOF measurement. TOF is an important

feature for large bore systems. It reduces the statistical uncertainty of the annihilation position estimation along the LOR and therefore improves the SNR. From our experience the design indications for high spatial resolution and high CTR can be conflicting. The factors we are aware of are the crystal coating, the pixel size and the readout scheme.
*Crystal coating.* On the one hand, black crystal coating reduces the photon reflections on the crystal sides and therefore helps to retain the event's light distribution. On the other hand we know that the light collection over multiple photodetector pixels already results in low SNR. The black coating further reduces the SNR and thus limits the achievable timing performance. To obtain better CTR polished surfaces with reflective coating would be more effective.
*SiPM pixel size.* Larger SiPM pixels provide better SNRs because more photons per area are detected. This is an advantage for CTR but not for spatial resolution. However this was concluded from simulations that only took into account PDE and pixel size, no other electronic specifications.
*Readout.* A summed row and column readout is a design advantage in terms of spatial resolution. The readout cost are much lower but the resolution does not degrade significantly. For CTR, however, the summed signal is a disadvantage because it inherently introduces some degree of uncertainty in the time-stamping of the event.
A future research topic should be the determination of an equilibrium between spatial resolution and CTR.
Since a major drawback of monolithic detectors is the lengthy calibration, effort should be made to reduce the work and time spent on it. Especially the strongly collimated beam in singles mode combined with a thick Lutetium-based scintillator, that has high intrinsic radioactivity, leads to a challenging calibration procedure. Other groups focus on better and faster calibrations in coincidence mode, and by using a slit collimator. Resulting from this thesis, it is the logical next step, to further investigate the use of optical simulations to speed up detector calibration. As a major step towards better calibration with simulated data we see the accurate modelling of the reflective surfaces in the detector. The use of surfaces that are easy to characterise, can be an important step. As a rule of thumb, polished surfaces are more predictable as the surface facet distribution has a smaller variability. Polished surfaces may be problematic at the edges since the large fraction of reflected photons shifts the light distribution. As a result the interaction position

estimation becomes more difficult to solve. A reinvestigation of polished sides with our neural network positioning algorithms might be successful. Furthermore, at this point the 'black paint'-model has not been validated for simulations which should be done in the future. Another option is simply switching to validated surface reflector models like, Teflon or ESR. A tool to ease the optical simulation workflow in Gate for monolithic detector calibration could be useful for the community. A list of input parameters would include: crystal material, crystal geometry, crystal surface treatment and reflector, SiPM pixel size, SiPM PDE, calibration grid size, events per calibration position.

## 8.3 Final conclusion

This dissertation demonstrated that monolithic detectors, with sufficient thickness for clinical PET applications, can provide very high intrinsic spatial resolution, approaching the fundamental spatial resolution limits of PET. Using optical simulation models we were able to grasp the factors that are limiting the intrinsic detector resolution and improve the hardware and software design of the prototype detector. Furthermore the development of an advanced simulation model demonstrated the potential of directly applying simulated data to improve monolithic detectors. The combination of high intrinsic spatial resolution with efficient calibration methods and good timing performance, can lead the way for monolithic detectors to be the detector of choice in future PET systems.

# Bibliography

[1] Terry Jones and David Townsend. "History and future technical innovation in positron emission tomography". In: *J. Med. Imaging* 4.1 (2017), p. 011013. DOI: `10.1117/1.jmi.4.1.011013`.

[2] Frederik L. Giesel et al. "68 Ga-FAPI PET/CT: Biodistribution and preliminary dosimetry estimate of 2 DOTA-containing FAP-targeting agents in patients with various cancers". In: *J. Nucl. Med.* 60.3 (2019), pp. 386–392. DOI: `10.2967/jnumed.118.215913`.

[3] Clemens Kratochwil et al. "68Ga-FAPI PET/CT: Tracer uptake in 28 different kinds of cancer". In: *J. Nucl. Med.* 60.6 (2019), pp. 801–805. DOI: `10.2967/jnumed.119.227967`.

[4] Frederik Giesel et al. "Intensity of tracer-uptake in FAPI-PET/CT in different kinds of cancer". In: *J. Nucl. Med.* 60.supplement 1 (2019), p. 289. URL: `https://jnm.snmjournals.org/content/60/supplement{\_}1/289`.

[5] Simon R. Cherry, James A. Sorenson, and Michael E. Phelps. *Physics in Nuclear Medicine*. 4th. Elsevier Saunders, 2012.

[6] Z. H. Cho et al. "Positron ranges obtained from biomedically important positron-emitting radionuclides". In: *J. Nucl. Med.* 16.12 (1975), pp. 1174–1176.

[7] C. S. Levin and E. J. Hoffman. "Calculation of positron range and its effect on the fundamental limit of positron emission tomography system spatial resolution". In: *Phys. Med. Biol.* 44 (1999), pp. 781–799. DOI: `10.1088/0031-9155/45/2/501`.

[8] Eric Berg and Simon R. Cherry. "Innovations in Instrumentation for Positron Emission Tomography". In: *Semin. Nucl. Med.* 48.4 (2018), pp. 311–331. DOI: `10.1053/j.semnuclmed.2018.02.006`.

[9] Ioannis Androulakis. “The effect of heart rate on CAC Scoring”. Master thesis. 2017. DOI: 10.13140/RG.2.2.10768.20480.

[10] Stefan Gundacker et al. “Experimental time resolution limits of modern SiPMs and TOF-PET detectors exploring different scintillators and Cherenkov emission”. In: *Phys. Med. Biol.* 65.2 (2020), 20pp. DOI: 10.1088/1361-6560/ab63b4.

[11] Jeffrey A. Kolthammer et al. “Performance evaluation of the Ingenuity TF PET/CT scanner with a focus on high count-rate conditions”. In: *Phys. Med. Biol.* 59 (2014), pp. 3843–3859. DOI: 10.1088/0031-9155/59/14/3843.

[12] B. W. Jakoby et al. “Physical and clinical performance of the mCT time-of-flight PET/CT scanner”. In: *Phys. Med. Biol.* 56 (2011), pp. 2375–2389. DOI: 10.1088/0031-9155/56/8/004.

[13] Michael Miller et al. “Characterization of the Vereos Digital Photon Counting PET System”. In: *J. Nucl. Med.* 56.Supplement 3 (2015), p. 434. URL: http://jnm.snmjournals.org/cgi/content/long/56/supplement{_}3/434.

[14] S Vandenberghe et al. “Recent developments in time-of-flight PET”. In: *EJNMMI Phys.* 3.3 (2016), pp. 1–30. DOI: 10.1186/s40658-016-0138-3.

[15] Joyce van Sluis et al. “Performance Characteristics of the Digital Biograph Vision PET/CT System”. In: *J. Nucl. Med.* 60.7 (2019), pp. 1031–1036. DOI: 10.2967/jnumed.118.215418.

[16] Paul Lecoq et al. “Roadmap toward the 10 ps time-of-flight PET challenge”. In: *Phys. Med. Biol.* 65.21RM01 (2020), 64pp. DOI: 10.1088/1361-6560/ab9500. URL: https://iopscience.iop.org/article/10.1088/1361-6560/ab9500.

[17] Jin Ho Jung et al. “Optimization of LSO/LuYAP phoswich detector for small animal PET”. In: *Nucl. Instruments Methods Phys. Res. Sect. A Accel. Spectrometers, Detect. Assoc. Equip.* 571.3 (2007), pp. 669–675. DOI: 10.1016/j.nima.2006.10.293. URL: https://linkinghub.elsevier.com/retrieve/pii/S0168900206022662.

[18] L. Eriksson et al. “Phoswich solutions for the PET DOI problem”. In: *Nucl. Instruments Methods Phys. Res. Sect. A Accel. Spectrometers, Detect. Assoc. Equip.* 648.SUPPL. 1 (2011), pp. 288–292. DOI: `10.1016/j.nima.2010.11.049`. URL: `http://dx.doi.org/10.1016/j.nima.2010.11.049https://linkinghub.elsevier.com/retrieve/pii/S016890021002512X`.

[19] Hendrik Thoen et al. “Influence of detector pixel size, TOF resolution and DOI on image quality in MR-compatible whole-body PET”. In: *Phys. Med. Biol.* 58.18 (2013), pp. 6459–6479. DOI: `10.1088/0031-9155/58/18/6459`.

[20] Mikiko Ito, Seong Jong Hong, and Jae Sung Lee. “Positron emission tomography (PET) detectors with depth-of- interaction (DOI) capability”. In: *Biomed. Eng. Lett.* 1.2 (2011), pp. 70–81. DOI: `10.1007/s13534-011-0019-6`.

[21] Myron L. Good Frank R. Wrenn and Philip Handler. “The Use of Positron-Emitting Radioisotopes for the Localization of Brain Tumors”. In: *Am. Assoc. Adv. Sci.* 113.2940 (1951), pp. 525–527.

[22] William H. Sweet. “The Uses of Nuclear Disintegration in the Diagnosis and Treatment of Brain Tumor”. In: *N. Engl. J. Med.* 245 (1951), pp. 875–878. DOI: `10.1056/NEJM195112062452301`.

[23] Gordon L. Brownell and William H. Sweet. “Localization of brain tumors with positron emitters”. In: *Nucleonics* 11.11 (1953), pp. 40–45.

[24] S. Rankowitz et al. *Positron scanner for location brain tumors.* Tech. rep. Upton, NY (United States): Brookhaven National Laboratory (BNL), 1961, pp. 49–56. DOI: `10.2172/4736421`.

[25] C. A. Burnham and Gordon L. Brownell. “A multi-crystal positron camera”. In: *IEEE Trans. Nucl. Sci.* 19.3 (1973), pp. 201–205. DOI: `10.1109/TNS.1972.4326726`.

[26] G. N. Hounsfield. “Computerized transverse axial scanning (tomography): Part 1. Description of system”. In: *Br. J. Radiol.* 46.552 (1973), pp. 1016–1022. DOI: `10.1259/0007-1285-46-552-1016`.

[27] J. Ambrose. “Computerized transverse axial scanning (tomography): II. Clinical application”. In: *Br. J. Radiol.* 46.552 (1973), pp. 1023–1047. DOI: `10.1259/0007-1285-46-552-1023`.

[28] Christopher J Thompson, Yayoi Yamamoto, and E. Meyer. "A Position Imaging System for the Measurement of Regional Cerebral Blood Flow". In: *Appl. Opt. Instrum. Med.* 96 (1976), p. 263. DOI: `10.1117/12.965421`.

[29] Michael E Phelps et al. "Application of annihilation coincidence detection to transaxial reconstruction tomography". In: *J. Nucl. Med.* 16.3 (1974), pp. 210–224.

[30] C. W. Williams, M. C. Crabtree, and S. G. Burgiss. "Design and performance characteristics of a positron emission computed axial tomograph –ECAT(R)-II". In: *IEEE Trans. Nucl. Sci.* NS-26.1 (1979), pp. 619–627.

[31] T. J. Spinks. "Physical characteristics of the ECAT EXACT3D positron tomograph". In: *Phys. Med. Biol.* 45 (2000), pp. 2601–2618.

[32] M E Casey and R Nutt. "A multicrystal two dimensional BGO detector system for positron emission tomography". In: *IEEE Trans. Nucl. Sci.* 33.1 (1986), pp. 460–463.

[33] D W Townsend et al. "Three dimensional reconstruction of PET data from a multi-ring camera". In: *IEEE Trans. Nucl. Sci.* 36.1 (1989), pp. 1056–1065.

[34] C. L. Melcher and J. S. Schweitzer. "A promising new scintillator: cerium-doped lutetium oxyorthosilicate". In: *Nucl. Inst. Methods Phys. Res. A* 314.1 (1992), pp. 212–214. DOI: `10.1016/0168-9002(92)90517-8`.

[35] Joel S. Karp et al. "Benefit of time-of-flight in PET: Experimental and clinical results". In: *J. Nucl. Med.* 49.3 (2008), pp. 462–470. DOI: `10.2967/jnumed.107.044834`.

[36] Cristina Lois et al. "An assessment of the impact of incorporating time-of-flight information into clinical PET/CT imaging". In: *J. Nucl. Med.* 51.2 (2010), pp. 237–245. DOI: `10.2967/jnumed.109.068098`.

[37] S. R. Cherry et al. "MicroPET: A high resolution PET scanner for imaging small animals". In: *IEEE Trans. Nucl. Sci.* 44.3 (1997), pp. 1161–1166. DOI: `10.1109/23.596981`.

[38] R. Lecomte et al. "Initial results from the sherbrooke avalanche photodiode positron tomograph". In: *IEEE Trans. Nucl. Sci.* 43.3 (1996), pp. 1952–1957. DOI: `10.1109/23.507252`.

[39] Suleman Surti et al. “Imaging performance of A-PET: A small animal PET camera”. In: *IEEE Trans. Med. Imaging* 24.7 (2005), pp. 844–852. DOI: `10.1109/TMI.2005.844078`.

[40] Marc C. Huisman et al. “Performance evaluation of the Philips MOSAIC small animal PET scanner”. In: *Eur. J. Nucl. Med. Mol. Imaging* 34 (2007), pp. 532–540. DOI: `10.1007/s00259-006-0271-7`.

[41] Istvan Szanda et al. “National electrical manufacturers association NU-4 performance evaluation of the PET component of the nanoPET/CT preclinical PET/CT scanner”. In: *J. Nucl. Med.* 52.11 (2011), pp. 1741–1747. DOI: `10.2967/jnumed.111.088260`.

[42] Kálmán Nagy et al. “Performance evaluation of the small-animal nanoscan PET/MRI system”. In: *J. Nucl. Med.* 54 (2013), pp. 1825–1832. DOI: `10.2967/jnumed.112.119065`.

[43] K. Sato et al. “Performance evaluation of the small-animal PET scanner ClairvivoPET using NEMA NU 4-2008 Standards”. In: *Phys. Med. Biol.* 61 (2015), pp. 696–711. DOI: `10.1088/0031-9155/61/2/696`.

[44] Srilalan Krishnamoorthy et al. “Performance evaluation of the MOLECUBES $\beta$ -CUBE—a high spatial resolution and high sensitivity small animal PET scanner utilizing monolithic LYSO scintillation detectors”. In: *Phys. Med. Biol.* 63.15 (2018), pp. 1–12. DOI: `10.1088/1361-6560/aacec3`.

[45] Simon R Cherry et al. “Total-body imaging: Transforming the role of positron emission tomography”. In: *Sci. Transl. Med.* 9 (2017), pp. 1–3. URL: `http://stm.sciencemag.org/content/scitransmed/9/381/eaaf6169.full.pdf`.

[46] Jonathan K. Poon et al. “Optimal whole-body PET scanner configurations for different volumes of LSO scintillator: A simulation study”. In: *Phys. Med. Biol.* 57.23 (2012), p. 8117. DOI: `10.1088/0031-9155/57/23/8117`.

[47] Simon R. Cherry et al. “Total-Body Pet: Maximizing Sensitivity To Create New Opportunities for Clinical Research and Patient Care”. In: *J. Nucl. Med.* 59.1 (2018), pp. 3–12. DOI: `10.2967/jnumed.116.184028`.

[48] Joel S. Karp et al. "PennPET explorer: Design and preliminary performance of a whole-body imager". In: *J. Nucl. Med.* 61.1 (2020), pp. 136–143. DOI: `10.2967/jnumed.119.229997`.

[49] Suleman Surti, Austin R. Pantel, and Joel S. Karp. "Total Body PET: Why, How, What for?" In: *IEEE Trans. Radiat. Plasma Med. Sci.* 4.3 (2020), pp. 283–292. DOI: `10.1109/trpms.2020.2985403`.

[50] Benjamin A. Spencer et al. "Performance Evaluation of the uEXPLORER Total-Body PET/CT Scanner Based on NEMA NU 2-2018 with Additional Tests to Characterize PET Scanners with a Long Axial Field of View". In: *J. Nucl. Med.* 62.6 (2021), pp. 861–870. DOI: `10.2967/jnumed.120.250597`.

[51] Stefaan Vandenberghe et al. "PET 20.0: A cost efficient, 2.00 mm resolution total body monolithic PET with very high sensitivity and an adaptive axial FOV up to 2.00 m". In: *Annu. Congr. Eur. Assoc. Nucl. Med.* Vienna, 2017, p. 305.

[52] Stefaan Vandenberghe, Pawel Moskal, and Joel S. Karp. "State of the art in total body PET". In: *EJNMMI Phys.* 7.1 (2020), p. 35. DOI: `10.1186/s40658-020-00290-2`. URL: `https://ejnmmiphys.springeropen.com/articles/10.1186/s40658-020-00290-2`.

[53] P Moskal et al. "Novel detector systems for the Positron Emission Tomography". In: *Bio-Algoritms Med-Syst* 7 (2011), p. 73. arXiv: `1305.5187`.

[54] P. Moskal et al. "Time resolution of the plastic scintillator strips with matrix photomultiplier readout for J-PET tomograph". In: *Phys. Med. Biol.* 61.5 (2016), pp. 2025–2047. DOI: `10.1088/0031-9155/61/5/2025`.

[55] Pawel Moskal et al. "Simulating NEMA characteristics of the modular total-body J-PET scanner - an economic total-body PET from plastic scintillators". In: *Phys. Med. Biol.* (2021). DOI: `10.1088/1361-6560/ac16bd`. URL: `https://iopscience.iop.org/article/10.1088/1361-6560/ac16bd`.

[56] S. Niedźwiecki et al. "J-PET: A New Technology for the Whole-body PET Imaging". In: *Acta Phys. Pol. B* 48.10 (2017), p. 1567. DOI: `10.5506/APhysPolB.48.1567`. arXiv: `1710.11369`.

[57] Ian Alberts et al. "Clinical performance of long axial field of view PET/CT: a head-to-head intra-individual comparison of the Biograph Vision Quadra with the Biograph Vision PET/CT". In: *Eur. J. Nucl. Med. Mol. Imaging* 48.8 (2021), pp. 2395–2404. DOI: `10.1007/s00259-021-05282-7`.

[58] Ramsey Badawi et al. "First Human Imaging Studies with the EXPLORER Total-Body PET Scanner". In: *J. Nucl. Med.* 60.3 (2019), pp. 299–303. DOI: `10.2967/jnumed.119.226498`.

[59] Jennifer R. Stickel, Jinyi Qi, and Simon R. Cherry. "Fabrication and characterization of a 0.5-mm lutetium oxyorthosilicate detector array for high-resolution PET applications". In: *J. Nucl. Med.* 48.1 (2007), pp. 115–121.

[60] Glenn F. Knoll. *Radiation Detection and Measurement.* 4th. 2010. DOI: `10.1109/PROC.1981.12016`.

[61] Epic Crystal. *LYSO(Ce) Crystal.* 2021. URL: `https://www.epic-crystal.com/oxide-scintillators/lyso-ce-scintillator.html`.

[62] B. J. Pichler et al. "Lutetium oxyorthosilicate block detector readout by avalanche photodiode arrays for high resolution animal PET". In: *Phys. Med. Biol.* 49.18 (2004), pp. 4305–4319. DOI: `10.1088/0031-9155/49/18/008`.

[63] Alexander M. Grant et al. "NEMA NU 2-2012 performance studies for the SiPM-based ToF-PET component of the GE SIGNA PET/MR system". In: *Med. Phys.* 43.5 (2016), pp. 2334–2343. DOI: `10.1118/1.4945416`.

[64] SensL. *An Introduction to the Silicon Photomultiplier.* Tech. rep. 2011, pp. 1–16.

[65] S. España et al. "Performance evaluation of SiPM photosensors in the presence of magnetic fields". In: *AIP Conf. Proc.* Vol. 1231. April. 2010, pp. 171–172. DOI: `10.1063/1.3428910`.

[66] Stefan Gundacker and Arjan Heering. "The silicon photomultiplier: Fundamentals and applications of a modern solid-state photon detector". In: *Phys. Med. Biol.* 65.17 (2020). DOI: `10.1088/1361-6560/ab7b2d`.

[67] ONSemiconductor. *J-Series SiPM Sensors Silicon Photomultipliers.* Tech. rep. 2018, pp. 1–12.

[68] Emilie Roncali, Mariele Stockhoff, and Simon R Cherry. “An integrated model of scintillator-reflector properties for advanced simulations of optical transport”. In: *Phys. Med. Biol.* 62.12 (2017), pp. 4811–4830. DOI: `10.1088/1361-6560/aa6ca5`.

[69] Andrea Gonzalez-Montoro et al. “Evolution of PET Detectors and Event Positioning Algorithms Using Monolithic Scintillation Crystals”. In: *IEEE Trans. Radiat. Plasma Med. Sci.* 5.3 (2021), pp. 282–305. DOI: `10.1109/TRPMS.2021.3059181`.

[70] Robert S. Miyaoka et al. “Resolution properties of a prototype continuous miniature crystal element (cMiCE) scanner”. In: *IEEE Trans. Nucl. Sci.* 58.5 (2011), pp. 2836–2840. DOI: `10.1109/TNS.2011.2165296`.

[71] Mariele Stockhoff, Roel Van Holen, and Stefaan Vandenberghe. “Optical simulation study on the spatial resolution of a thick monolithic PET detector”. In: *Phys. Med. Biol.* 64.19 (2019), p. 195003. DOI: `10.1088/1361-6560/ab3b83`.

[72] Efthymios Lamprou et al. “Exploring TOF capabilities of PET detector blocks based on large monolithic crystals and analog SiPMs”. In: *Phys. Medica* 70.December 2019 (2020), pp. 10–18. DOI: `10.1016/j.ejmp.2019.12.004`.

[73] Giacomo Borghi, Valerio Tabacchini, and Dennis R Schaart. “Towards monolithic scintillator based TOF-PET systems: practical methods for detector calibration and operation”. In: *Phys. Med. Biol.* 61 (2016), pp. 4904–4928. DOI: `10.1088/0031-9155/61/13/4904`.

[74] Andrea González-Montoro et al. “Detector block performance based on a monolithic LYSO crystal using a novel signal multiplexing method”. In: *Nucl. Instruments Methods Phys. Res. Sect. A Accel. Spectrometers, Detect. Assoc. Equip.* 912 (2018), pp. 372–377. DOI: `10.1016/j.nima.2017.10.098`.

[75] Garry Chinn, Peter D. Olcott, and Craig S. Levin. “Sparse signal recovery methods for multiplexing PET detector readout”. In: *IEEE Trans. Med. Imaging* 32.5 (2013), pp. 932–942. DOI: `10.1109/TMI.2013.2246182`.

[76] L. A. Pierce et al. “Multiplexing strategies for monolithic crystal PET detector modules”. In: *Phys. Med. Biol.* 59.18 (2014), pp. 5347–5360. DOI: `10.1088/0031-9155/59/18/5347`.

[77] Qian Yang et al. “Performance comparison of two signal multiplexing readouts for SiPM-based pet detector”. In: *Phys. Med. Biol.* 64.23NT02 (2019), pp. 1–11. DOI: `10.1088/1361-6560/ab5738`.

[78] S. Gundacker et al. “State of the art timing in TOF-PET detectors with LuAG, GAGG and L(Y)SO scintillators of various sizes coupled to FBK-SiPMs”. In: *JINST* 11.P08008 (2016), pp. 1–16. DOI: `10.1088/1748-0221/11/08/P08008`.

[79] Giacomo Borghi et al. “Experimental validation of an efficient fan-beam calibration procedure for k-nearest neighbor position estimation in monolithic scintillator detectors”. In: *IEEE Trans. Nucl. Sci.* 62.1 (2015), pp. 57–67. DOI: `10.1109/TNS.2014.2375557`.

[80] Florian Müller et al. “Gradient Tree Boosting-based Positioning Method for Monolithic Scintillator Crystals in Positron Emission Tomography”. In: *IEEE Trans. Radiat. Plasma Med. Sci.* 2.5 (2018), pp. 411–421. DOI: `10.1109/TRPMS.2018.2837738`.

[81] Pieter Mollet et al. “The $\beta$-CUBE, a high-end compact preclinical benchtop PET for total body imaging”. In: *J. Nucl. Med.* 58.Supplement 1 (2017), p. 393. URL: `http://jnm.snmjournals.org/content/58/supplement{\_}1/393.abstract`.

[82] Andrea González-Montoro et al. “Novel method to measure the intrinsic spatial resolution in PET detectors based on monolithic crystals”. In: *Nucl. Instruments Methods Phys. Res. Sect. A Accel. Spectrometers, Detect. Assoc. Equip.* 920.November 2018 (2019), pp. 58–67. DOI: `10.1016/j.nima.2018.12.056`.

[83] Marta Freire et al. “Calibration of Gamma Ray Impacts in Monolithic - Based Detectors Using Voronoi Diagrams”. In: *IEEE Trans. Radiat. Plasma Med. Sci.* 4.3 (2019), pp. 350–360. DOI: `10.1109/trpms.2019.2947716`.

[84] Samuel España et al. “Fast calibration of SPECT monolithic scintillation detectors using un-collimated sources”. In: *Phys. Med. Biol.* 58.14 (2013), pp. 4807–4825. DOI: `10.1088/0031-9155/58/14/4807`.

[85] Robert S Miyaoka et al. “Calibration procedure for a continuous miniature crystal element (cMiCE) detector”. In: *IEEE Trans. Nucl. Sci.* 57.3 (2010), pp. 1023–1028. DOI: `10.1109/NSSMIC.2007.4437070`.

[86] Herman T. van Dam et al. “Improved nearest neighbor methods for gamma photon interaction position determination in monolithic scintillator PET detectors”. In: *IEEE Trans. Nucl. Sci.* 58.5 (2011), pp. 2139–2147. DOI: `10.1109/TNS.2011.2150762`.

[87] Hal O. Anger. “Scintillation camera”. In: *Rev. Sci. Instrum.* 29.27 (1958). DOI: `10.1016/0160-4120(91)90365-w`.

[88] Karel Deprez. “Preclinical SPECT imaging based on compact collimators and high resolution scintillation detectors”. PhD Thesis. Universiteit Gent, 2014.

[89] R. Pani et al. “Preliminary evaluation of a monolithic detector module for integrated PET/MRI scanner with high spatial resolution”. In: *J. Instrum.* 10.6 (2015). DOI: `10.1088/1748-0221/10/06/C06006`.

[90] Robert M Gray and Albert Macovski. “Maximum a posteriori estimation of position in scintillation cameras”. In: *IEEE Trans. Nucl. Sci.* NS-23.1 (1976), pp. 849–852.

[91] Harrison H Barrett et al. “Maximum-Likelihood Methods for Processing Signals From Gamma-Ray Detectors”. In: *IEEE Trans. Nucl. Sci.* 56.3 (2009), p. 725.

[92] Samuel España et al. “DigiPET: Sub-millimeter spatial resolution small-animal PET imaging using thin monolithic scintillators”. In: *Phys. Med. Biol.* 59.13 (2014), pp. 3405–3420. DOI: `10.1088/0031-9155/59/13/3405`.

[93] Yoshiyuki Hirano, Tsutomu Zeniya, and Hidehiro Iida. “Monte Carlo simulation of scintillation photons for the design of a high-resolution SPECT detector dedicated to human brain”. In: *Ann. Nucl. Med.* 26 (2012), pp. 214–221. DOI: `10.1007/s12149-011-0561-4`.

[94] Jacob Y. Hesterman et al. “Maximum-likelihood estimation with a contracting-grid search algorithm”. In: *IEEE Trans. Nucl. Sci.* 57.3 PART 1 (2010), pp. 1077–1084. DOI: `10.1109/TNS.2010.2045898`.

[95] M.C. Maas et al. “Experimental Characterization of Monolithic-Crystal Small Animal PET Detectors Read Out by APD Arrays”. In: *IEEE Trans. Nucl. Sci.* 53.3 (2006), pp. 1071–1077. DOI: `10.1109/NSSMIC.2004.1466303`.

[96] T M Cover and P E Hart. “Nearest Neighbor Pattern Classification”. In: *IEEE Trans. Inf. Theory* IT-13.1 (1967), pp. 21–27. DOI: `10.1007/978-0-387-30164-8`.

[97] T. Ling, T. K. Lewellen, and R. S. Miyaoka. “Depth of interaction decoding of a continuous crystal detector module”. In: *Phys. Med. Biol.* 52 (2007), pp. 2213–2228. DOI: `10.1109/NSSMIC.2006.356509`.

[98] P. Conde et al. “Determination of the Interaction Position of Gamma Photons in Monolithic Scintillators Using Neural Network Fitting”. In: *IEEE Trans. Nucl. Sci.* 63.1 (2016), pp. 30–36. DOI: `10.1109/TNS.2016.2515163`.

[99] Y. Wang et al. “3D position estimation using an artificial neural network for a continuous scintillator PET detector.” In: *Phys. Med. Biol.* 58.5 (2013), pp. 1375–1390. DOI: `10.1088/0031-9155/58/5/1375`.

[100] Milan Decuyper et al. “Artificial neural networks for positioning of gamma interactions in monolithic PET detectors”. In: *Phys. Med. Biol.* 66.7 (2021), pp. 1–15. DOI: `10.1088/1361-6560/abebfc`.

[101] Peter Bruyndonckx et al. “Neural network-based position estimators for PET detectors using monolithic LSO blocks”. In: *IEEE Trans. Nucl. Sci.* 51.5 II (2004), pp. 2520–2525. DOI: `10.1109/TNS.2004.835782`.

[102] A. Iborra et al. “Ensemble of neural networks for 3D position estimation in monolithic PET detectors”. In: *Phys. Med. Biol.* 64.195010 (2019), 20pp. DOI: `10.1088/1361-6560/ab3b86`.

[103] Florian Müller et al. “A novel DOI positioning algorithm for monolithic scintillator crystals in PET based on gradient tree boosting”. In: *IEEE Trans. Radiat. Plasma Med. Sci.* 3.4 (2019), pp. 465–474. DOI: `10.1109/trpms.2018.2884320`.

[104] David Sarrut et al. “Advanced Monte Carlo simulations of emission tomography imaging systems with GATE”. In: *Phys. Med. Biol.* 66.10 (2021), p. 23. DOI: `10.1088/1361-6560/abf276`.

[105] S. Agostinelli et al. “Geant4—a simulation toolkit”. In: *Nucl. Instruments Methods Phys. Res. Sect. A Accel. Spectrometers, Detect. Assoc. Equip.* 506.3 (2003), pp. 250–303. DOI: `10.1016/S0168-9002(03)01368-8`.

[106] S Jan et al. “GATE: a simulation toolkit for PET and SPECT”. In: *Phys. Med. Biol.* 49.19 (2004), pp. 4543–4561. DOI: `10.1088/0031-9155/49/19/007`.

[107] Sebastien Jan et al. “GATE V6: a major enhancement of the GATE simulation platform enabling modelling of CT and radiotherapy”. In: *Phys. Med. Biol.* 56.4 (2011), pp. 881–901. DOI: `10.1088/0031-9155/56/4/001`.

[108] Emilie Roncali and Simon R Cherry. “Simulation of light transport in scintillators based on 3D characterization of crystal surfaces”. In: *Phys. Med. Biol.* 58.7 (2013), pp. 2185–2198. DOI: `10.1088/0031-9155/58/7/2185`.

[109] Shree Nayar, Katsushi Ikeuchi, and Takeo; Kanade. “Surface Reflection: Physical and Geometrical Perspectives”. In: *IEEE Trans. Pattern Anal. Mach. Intell.* 13.7 (1991), pp. 611–634.

[110] A. Levin and C. Moisan. “A more physical approach to model the surface treatment of scintillation counters and its implementation into DETECT”. In: *IEEE Nucl Sci Symp Conf Rec.* 1996, pp. 702–706. DOI: `10.1109/NSSMIC.1996.591410`.

[111] J. Bea et al. “Simulation of light collection in scintillators with rough surfaces”. In: *Nucl. Instrum. Methods Phys. Res A* 350.1-2 (1994), pp. 184–191. DOI: `10.1016/0168-9002(94)91162-2`.

[112] Martin Janecek and William W. Moses. “Simulating scintillator light collection using measured optical reflectance”. In: *IEEE Trans. Nucl. Sci.* 57.3 (2010), pp. 964–970. URL: `https://www.escholarship.org/uc/item/0xw5n4n3`.

[113] Carlotta Trigila, Eshani Moghe, and Emilie Roncali. “Technical Note: Standalone application to generate custom reflectance Look-Up Table for advanced optical Monte Carlo simulation in GATE/Geant4”. In: *Med. Phys.* 48.6 (2021), pp. 2800–2808. DOI: `10.1002/mp.14863`.

[114] Mariele Stockhoff et al. “Advanced optical simulation of scintillation detectors in GATE V8.0: first implementation of a reflectance model based on measured data”. In: *Phys. Med. Biol.* 62.12 (2017), pp. L1–L8. DOI: `10.1088/1361-6560/aa7007`.

[115] Mariele Stockhoff, Roel Van Holen, and Stefaan Vandenberghe. “Optical simulation study for high resolution monolithic detector design for TB-PET”. In: *EJNMMI Phys.* Vol. 5. S1. 2018, p. 8. DOI: `10.1186/s40658-018-0218-7`.

[116] M Stockhoff, R Van Holen, and S Vandenberghe. “High-resolution monolithic detector design for clinical PET systems: Advanced optical simulation study”. In: *IEEE Nucl. Sci. Symp. Med. Imaging Conf. Poster.* Sydney, Australia, 2018.

[117] Mariele Stockhoff, Roel Van Holen, and Stefaan Vandenberghe. “High-resolution monolithic detector design for clinical positron emission tomography systems”. In: *17th Natl. Day Biomed. Eng.* 2018.

[118] Milan Decuyper, Mariele Stockhoff, and Roel Van Holen. “Deep Learning for Positioning of Gamma Interactions in Monolithic PET Detectors”. In: *IEEE Nucl. Sci. Symp. Med. Imaging Conf. Poster.* Manchester, UK, 2019.

[119] Mariele Stockhoff et al. “High-resolution monolithic LYSO detector with 6-layer depth-of-interaction for clinical PET”. In: *Phys. Med. Biol.* 66.15 (2021), p. 155014. DOI: `10.1088/1361-6560/ac1459`.

[120] Mariele Stockhoff, Roel Van Holen, and Stefaan Vandenberghe. “Monolithic PET detectors with sub-mm transverse and 6 layer DOI identification for next generation high resolution clinical PET scanners”. In: *Eur. J. Nucl. Med. Mol. Imaging, Poster.* Vol. 56. Barcelona, Spain: October 12 – 16, 2019, p. 2019.

[121] Mariele Stockhoff et al. “Spatial resolution of large monolithic detector: performance evaluation with two positioning algorithms”. In: *IEEE Nucl. Sci. Symp. Med. Imaging Conf. Poster.* Boston (online), 2020. DOI: `10.1088/1361-6560/ab3b83`.

[122] Karel Deprez et al. “Design of a high resolution scintillator based SPECT detector (SPECTatress)”. In: *Nucl. Instruments Methods Phys. Res. Sect. A Accel. Spectrometers, Detect. Assoc. Equip.*

648.SUPPL. 1 (2011), pp. 107–110. DOI: `10.1016/j.nima.2010.12.081`.

[123] H. Alva-Sánchez et al. “Understanding the intrinsic radioactivity energy spectrum from 176Lu in LYSO/LSO scintillation crystals”. In: *Sci. Rep.* 8.1 (2018), pp. 1–7. DOI: `10.1038/s41598-018-35684-x`.

[124] Peter Bruyndonckx et al. “Towards a continuous crystal APD-based PET detector design”. In: *Nucl. Instruments Methods Phys. Res. Sect. A Accel. Spectrometers, Detect. Assoc. Equip.* 571.1-2 SPEC. ISS. (2007), pp. 182–186. DOI: `10.1016/j.nima.2006.10.058`.

[125] M Stockhoff, R Van Holen, and S Vandenberghe. “Influence of photon detection efficiency and multiplexing on spatial resolution in monolithic PET detectors”. In: *IEEE Nucl. Sci. Symp. Med. Imaging Conf. Poster.* 2018, p. 3039.

[126] Mariele Stockhoff, Roel Van Holen, and Stefaan Vandenberghe. “Identifying potential sources of resolution degradation in monolithic scintillators: simulations vs experiments”. In: *IEEE Nucl. Sci. Symp. Med. Imaging Conf. Poster.* Boston (online), 2020.

[127] Milan Decuyper et al. “Mitigating the Adverse Effect of Compton Scatter on the Positioning of Gamma Interactions in Large Monolithic PET Detectors”. In: *2020 IEEE Nucl. Sci. Symp. Med. Imaging Conf.* Boston (online): IEEE, 2020, pp. 1–3. DOI: `10.1109/NSS/MIC42677.2020.9507885`.

[128] Marnix C. Maas et al. “Model of the point spread function of monolithic scintillator PET detectors for perpendicular incidence”. In: *Med. Phys.* 37.4 (2010), pp. 1904–1913. DOI: `10.1118/1.3355889`.

[129] Milan Decuyper. “Advancing medical imaging with artificial intelligence: PET acquisition enhancement and MRI based brain tumour diagnosis”. PhD thesis. Ghent University.

[130] Harrison H Barrett and William Swindell. “Radiological Imaging: The Theory of Image Formation, Detection, and Processing”. In: San Diego, California: Academic Press, 1981, pp. 061–116. URL: `https://www.sciencedirect.com/book/9780080572307/radiological-imaging`.

[131] T Ling et al. “Parametric positioning of a continuous crystal PET detector with depth of interaction decoding”. In: *Phys. Med. Biol.* 53.7 (2008), pp. 1843–1863. DOI: `10.1088/0031-9155/53/7/003.Parametric`.

[132] Wang Yonggang, Cheng Xinyi, and Li Deng. “Improved statistics based positioning scheme for continuous thick crystal PET detectors”. In: *IEEE Trans. Nucl. Sci.* Vol. 60. 3. IEEE, 2013, pp. 1527–1532. DOI: `10.1109/NSSMIC.2012.6551522`.

[133] Sascha Moehrs et al. “A detector head design for small-animal PET with silicon photomultipliers (SiPM)”. In: *Phys. Med. Biol.* 51.5 (2006), pp. 1113–1127. DOI: `10.1088/0031-9155/51/5/004`.

[134] Zhi Li et al. “Nonlinear least-squares modeling of 3D interaction position in a monolithic scintillator block”. In: *Phys. Med. Biol.* 55.21 (2010), pp. 6515–6532. DOI: `10.1088/0031-9155/55/21/012`.

[135] Ane Etxebeste et al. “Study of sensitivity and resolution for full ring PET prototypes based on continuous crystals and analytical modeling of the light distribution”. In: *Phys. Med. Biol.* 64.3 (2019). DOI: `10.1088/1361-6560/aaf7ba`.

[136] Ane Etxebeste et al. “3D position determination in monolithic crystals coupled to SiPMs for PET”. In: *Phys. Med. Biol.* 61.10 (2016), pp. 3914–3934. DOI: `10.1088/0031-9155/61/10/3914`.

Human undergoing radiological exam.